Space-Time Adaptive Processing
For Side-Looking Arrays
With Platform Maneuver

THESIS

John T. Buckreis, Captain, USAF

AFIT/GE/ENG/06-09

DEPARTMENT OF THE AIR FORCE
AIR UNIVERSITY

AIR FORCE INSTITUTE OF TECHNOLOGY

Wright-Patterson Air Force Base, Ohio

The views expressed in this thesis are those of the author and do not reflect the official policy or position of the United States Air Force, Department of Defense, or the United States Government.

SPACE-TIME ADAPTIVE PROCESSING
FOR SIDE-LOOKING ARRAYS
WITH PLATFORM MANEUVER

THESIS

Presented to the Faculty

Department of Electrical and Computer Engineering

Graduate School of Engineering and Management

Air Force Institute of Technology

Air University

Air Education and Training Command

In Partial Fulfillment of the Requirements for the

Degree of Master of Science in Electrical Engineering

John T. Buckreis, B.S.E.E.

Captain, USAF

March 2006

AFIT/GE/ENG/06-09

SPACE-TIME ADAPTIVE PROCESSING
FOR SIDE-LOOKING ARRAYS
WITH PLATFORM MANEUVER

John T. Buckreis, B.S.E.E.

Captain, USAF

Approved:

/signed/	06 Mar 2006
Maj T.B. Hale, PhD (Chairman)	date
/signed/	06 Mar 2006
Dr. R.K. Martin (Member)	date
/signed/	06 Mar 2006
Dr. A.J. Terzuoli (Member)	date

AFIT/GE/ENG/06-09

Abstract

This research develops a space-time adaptive processing (STAP) radar model for side-looking (SL) arrays with platform maneuver incorporation, and examines maneuver effects on Matched Filter (MF) performance and sample support homogeneity for linear and planar arrays at various ranges. A primary assumption of most STAP models is the absence of platform maneuver during the coherent processing interval (CPI). This research abandons the platform stationarity assumption, allowing platform pitch, roll, and yaw during the CPI. Maneuver rates (set to 800°/sec) are held constant throughout the CPI and each maneuver type is examined individually.

All maneuver effects have a negative impact on both MF performance and sample support homogeneity. The introduction of pitch marginally impacts MF Signal-to-Interface-plus-Noise-Ratio (SINR) due to the lack of achieved azimuth resolution in this research, but decreases available homogenous sample support 24% at 11 km and 20% at 66 km. Roll impact on MF performance is observed only in the planar array, with MF SINR dropping 4 dB but sample support homogeneity is unaffected. Yaw effects are the by far the most devastating, dropping output SINR 15 dB at 11 km and 66 km, and decreasing available homogeneous sample support 34% at 11 km and 18% at 66 km.

Acknowledgements

I extend my sincere appreciation and thanks to my thesis advisor, Major Todd Hale, whose hard work and dedication helped make this thesis a reality. I'm indebted to my fellow Radar and Electromagnetics classmates, whose company during long days in classes and late nights in labs ensured proper perspective and brought needed humor.

And finally, a heartfelt thank you to my wife whose admirable patience, compassion, and encouragement were a stabilizing force.

John T. Buckreis

Table of Contents

List of Figures

ix

List of Tables

List of Symbols

xiii

List of Abbreviations

Space-Time Adaptive Processing

For Side-Looking Arrays

With Platform Maneuver

I. Introduction

This research's primary objective is the advancement of space-time adaptive processing (STAP) radar data models for the side-looking (SL) array. A modeling process often requires assumptions that limit a model's scope, ideally without sacrificing its accuracy or integrity. A primary assumption of most STAP models is the absence of platform maneuver during the coherent processing interval (CPI). Airborne radar platforms are predominantly modeled as stationary, and while limited published work has modeled the impact of that assumption on the forward-looking (FL) array, no published work discovered has modeled the impact on the SL array. This research abandons the platform stationarity assumption, allowing platform pitch, roll, and yaw during the CPI. The primary focus of this research is the maneuver model development, based on the popular stationary model of [3, 10]. Secondary objectives include characterizing platform maneuver effects on the clutter environment, examining resulting Matched Filter (MF) output Signal-to-Interference-plus-Noise-Ratio (SINR), and examining maneuver impact on data homogeneity and sample support.

1.1 Motivation

The primary motivation for this research is contributing an additional layer of capability and robustness to the popular model of [3, 10]. Limited published work investigates the impact of platform maneuver. And while two authors have examined the FL scenario, the clutter models used were their own and not widely available nor used. This research offers a complete framework to model platform maneuver within the context of the popular [3, 10] model. Future researchers may use this framework to examine maneuver effects on partially-adaptive processing techniques. Others may

use it to explore optimum processing techniques less susceptible to platform maneuver. Others may convert this research to a forward-looking (FL) array, the orientation of most fighter aircraft today. This thesis lays the groundwork for future investigations of platform maneuver. Today's fly-by-wire aircraft constantly monitor their platform attitude, offering an additional potential application of the framework this research builds. This research may offer potential uses in the space-based radar area as well, as platform maneuver and space-based radar are inseparable.

1.2   Organization

The stationary model of [3,10] serves as the foundation for this research. It and STAP fundamentals are discussed in Chapter II. The maneuver model is developed in Chapter III, abandoning the stationary platform assumption of [3,10]. The maneuver model is implemented in Chapter IV, and maneuver effects on the clutter environment, target, and radar performance are examined. Research results, improvements, and future relevant research incorporating platform maneuver are offered in Chapter V.

1.3   Assumptions

Several assumptions within the stationary model of [3,10] remain in the maneuver model developed. The waveform is considered narrowband, and signals are co-phased with phase shifts and not time delays. The waveform is assumed Doppler tolerant, making the time-frequency-autocorrelation-function (TFACF) unity. Targets are modeled as point scatterers with constant radar cross section (RCS), independent of incidence angle. Maneuver is modeled as rotation about the array reference element, without regard to array location on the platform. Range walk effects have been previously characterized [5], are not this research's focus, and are ignored. Ground clutter is assumed overwhelmingly stronger than atmospheric and all other attenuation effects, and is the only factor modeled. Finally, the return signal is assumed a perfect plane wave, with no phase error across the antenna face.

II. SL Stationary Model, STAP Fundamentals, and Literature Review

Relevant background knowledge consists of four major areas discussed in this chapter: an airborne radar overview, the physical airborne radar model for a stationary platform, space-time adaptive processing (STAP) concepts, techniques, and metrics, and previously published work investigating platform maneuver effects on STAP performance for the forward-looking (FL) array.

Concepts and details of the popular STAP model, developed for side-looking (SL) linear arrays in [10] and extended to planar arrays in [3], are highlighted in Section 2.2. The stationary model presented serves as the foundation of the maneuver model in Chapter III. Major components of the model include the geometry, transmit signal, receive signal, formatting, antenna pattern, target model, noise model, and clutter model. A major assumption of this popular model, abandoned in Chapter III and the focus of this thesis, is the absence of platform maneuver during the coherent processing interval (CPI).

STAP concepts, techniques, and metrics are highlighted in Section 2.3. Included are STAP fundamentals, fully and partially adaptive processing techniques, covariance estimation, sample support homogeneity issues, and performance metrics.

Finally, previously published work modeling platform maneuver effects on FL STAP are discussed in Section 2.4. Limited published work for the SL array with platform maneuver is available. Two significant contributors for the FL array are Peter G. Richardson [7,8] and George M. Herbert [4].

Before delving into the stationary model development and STAP concepts, Section 2.1 offers a brief overview of the airborne radar problem.

2.1 Airborne Radar Overview

The most basic and fundamental goal of a radar system is target detection. Detection requires the radar to distinguish targets from the interference environment.

Pulsed Doppler radars take advantage of a target's Doppler frequency, a shift due to signal time compression (or dilation) dependent upon the target-radar relative velocity [6]. The Doppler frequency f_d of a target is given by [9]

$$f_d = \frac{2v_r}{\lambda_o},\tag{2.1}$$

where v_r is the relative velocity between the radar and target, and λ_o is the transmitted signal's wavelength. In the ground-based radar scenario, the relative velocity between the radar and ground clutter is zero since neither are moving. Therefore, moving targets that produce a Doppler shift are easily separable from zero Doppler clutter. The airborne radar does not possess this advantage. Ground clutter returns possess a Doppler frequency in the airborne radar scenario due to the aircraft's velocity, making the task of separating slow moving targets from clutter more difficult.

A basic pulsed Doppler radar system transmits a series of pulses, samples the environment at specific times corresponding to range, receives the return pulses, then adds (or equivalently, integrates) the pulses. The method of integration can have dramatic effects on detection performance. Non-adaptive (NA) techniques, among the earliest methods of processing techniques, simply add all available returns without any consideration of their contents. The problem arises when the returns contain both the desired target *and* undesired interference. The concept of adaptive-processing is to intelligently weight available returns to *minimize* interference effects and *maximize* target returns, Signal-to-Interference-plus-Noise Ratio (SINR), and detection capability.

In order to intelligently choose these adaptive weights, the interference environment must be known or estimated. The airborne radar model described next in Section 2.2 models this interference environment for a SL antenna array. Section 2.3 then describes fundamental STAP concepts, techniques, and metrics used to enhance target detection.

4
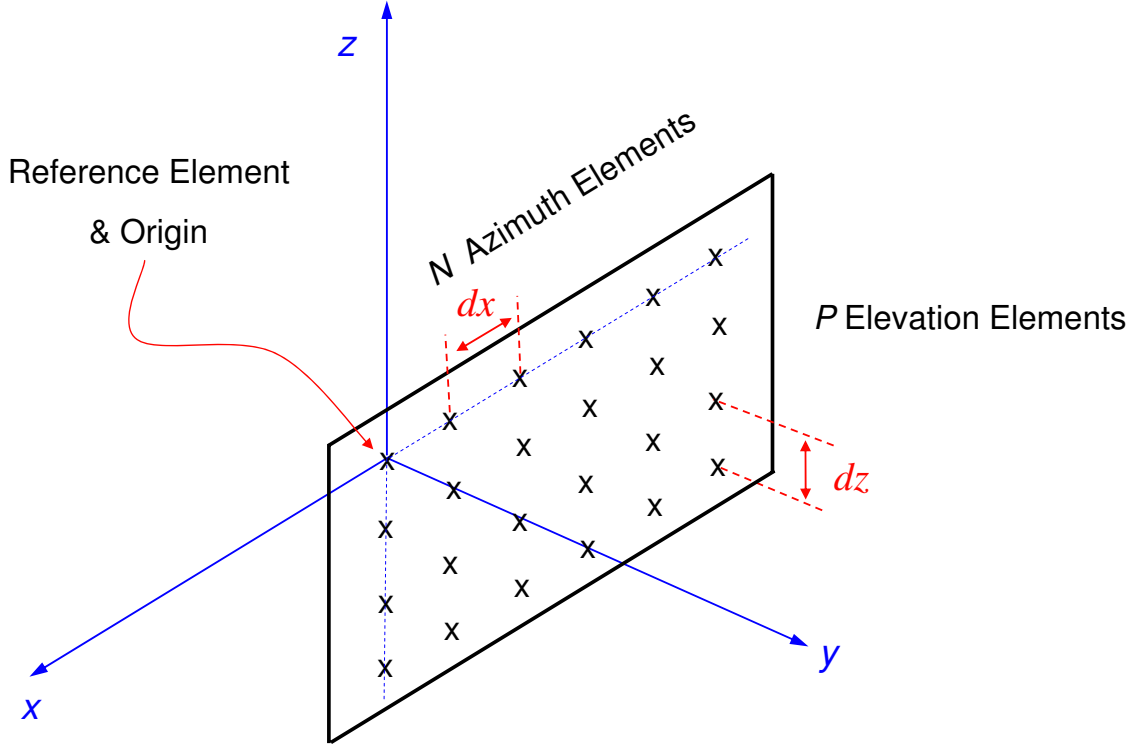
Figure 2.1: Antenna array geometry for stationary model. The antenna array is oriented in the x-z plane. Its reference element, defined as the upper-left most element, serves as the origin of the cartesian and radar coordinate systems. The elements are uniformly spaced with inter-element spacings of dx in the x direction and dz in the z direction. The N azimuth channels are numbered 0 to $N-1$, and the P elevation channels 0 to $P-1$.

2.2 Airborne Radar Model for Stationary Platform

The goal of the radar model is accurate characterization of the target and the interference environment. The first model component is the scenario geometry. Once the geometry is defined, the transmit and receive signals are described. The returns are then formatted in a linear algebra framework. Finally, the interference (noise and clutter) environment is modeled. The following sections examine each of these pieces from the model of [3, 10] in detail.

2.2.1 Geometry. Consider the antenna array depicted in Figure 2.1. The antenna is orientated in the x-z plane with N horizontal elements and P elevation

elements. The horizontal elements are numbered from zero to $N-1$ with uniform inter-element spacing dx, while the vertical elements are numbered zero to $P-1$ with uniform inter-element spacing dz. The antenna is mounted in a SL configuration on an aircraft above the ground, as depicted in Figure 2.2. Boresight is defined in the $\hat{\mathbf{y}}$ direction. The aircraft travels at speed v_a in the $\hat{\mathbf{x}}$ direction perpendicular to the y-z plane. A target is located at an elevation angle θ and azimuth angle ϕ. The radar elevation angle θ is negative when measured from boresight towards the ground and the radar azimuth angle ϕ is positive when measured from boresight to the positive x-axis (toward the nose of the plane). The upper and left most element is the first element to receive returns from a target at positive θ and positive ϕ, and is therefore designated the reference element. The reference element defines the origin (0,0,0) of the reference cartesian coordinate system. The reference element and element separations dx and dz define individual array element locations. The unit vector from the reference element to the np^{th} element is [3]

$$\hat{\mathbf{d}}_{np} = -nd_x\hat{\mathbf{x}} - pd_z\hat{\mathbf{z}}. \tag{2.2}$$

The vector $\hat{\mathbf{k}}$ describes the unit vector to a target at (θ,ϕ) and a transformation from the radar coordinate system to the cartesian coordinate system. Unit vector $\hat{\mathbf{k}}$ is the projection onto the cartesian unit vectors $\hat{\mathbf{x}}$, $\hat{\mathbf{y}}$, and $\hat{\mathbf{z}}$ [3],

$$\hat{\mathbf{k}} = \cos\theta\sin\phi\hat{\mathbf{x}} + \cos\theta\cos\phi\hat{\mathbf{y}} + \sin\theta\hat{\mathbf{z}}. \tag{2.3}$$

Equations (2.2) and (2.3) fully describe the airborne radar SL array physical picture. The radar transmit and receive signals are next characterized.
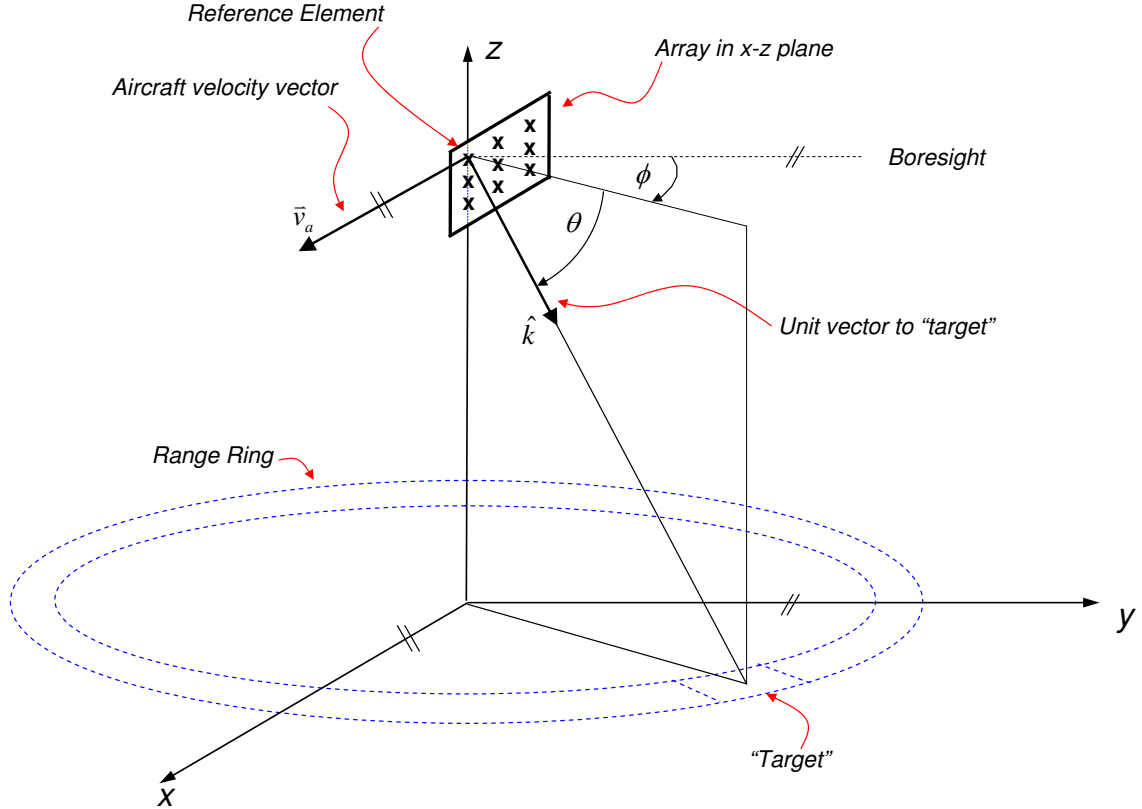
Figure 2.2:   Radar platform geometry. The array is mounted on an aircraft in a SL configuration with boresight defined in the $\hat{\mathbf{y}}$ direction. The aircraft travels at speed v_a in the $\hat{\mathbf{x}}$ direction. The vector $\hat{\mathbf{k}}$ is the unit vector from the reference element to the target at (θ, ϕ).

2.2.2   Transmit Signal.   Construction of the transmit signal model begins with a single pulse (the standard envelope function) $u_p(t)$ [3],

$$u_p(t) = \begin{cases} 1 & 0 \leq t \leq \tau \\ 0 & \text{otherwise}, \end{cases}$$

where τ is the uncompressed pulse width. Multiple copies of $u_p(t)$ shifted by integer multiples of the pulse repetition interval (PRI) T_r create the pulse train $u(t)$,

$$u(t) = \sum_{m=0}^{M-1} u_p(t - mT_r). \tag{2.4}$$

The summation bounds determine the CPI length of M pulses or equivalently MT_r seconds. Incorporation of a signal amplitude a_t, carrier frequency ω_o, and random starting phase φ yields the complete transmitted pulsed radar signal $s(t)$,

$$s(t) = a_t u(t) e^{j(\omega_o t + \varphi)}. \tag{2.5}$$

2.2.3 Received Signal. Upon transmission the signal propagates through free space as a plane wave, reflects off a target, and is received by each individual array element as a plane wave. Each individual array element contains its own receiver chain. The received signal at each np^{th} element contains three major differences than the original transmit signal: a Doppler shift f_d (assumed equal for all elements) due to relative target velocity v_r; a time delay τ_{np} due to the round trip time T_R and differential time delay τ'_{np}; and a received amplitude a_r. Incorporating these effects yields the received signal at element np [3],

$$s_{np}(t) \quad = \quad a_r u(t - \tau_{np}) e^{j 2\pi f_o (t - \tau_{np})} e^{j 2\pi f_d (t - \tau_{np})} e^{j\varphi}. \tag{2.6}$$

The receive amplitude a_r includes range and radar cross section (RCS) attenuation effects, fully discussed in [9]. The time delay τ_{np} is the sum of the round trip time from the array face to the target, T_R, and the differential time τ'_{np} from the reference element to each individual np^{th} element,

$$\tau_{np} = T_R + \tau'_{np}. \tag{2.7}$$

A narrowband assumption requires a signal time duration greater than the time required to propagate across the face of the array. The pulsewidth must therefore meet the requirement

$$\tau \gg \frac{\sqrt{(Nd_x)^2 + (Pd_z)^2}}{c}, \tag{2.8}$$

8

where $\sqrt{(Nd_x)^2 + (Pd_z)^2}$ represents the greatest distance across the array face and c the propagation speed. Under the narrowband assumption each channel receives the return signal simultaneously and τ'_{np} is ignored with respect to time, but *not phase*. Substituting (2.7) into (2.6), ignoring the differential delay τ'_{np} in the pulse train, and rearranging the result yields

$$s_{np}(t) = a_r u(t - T_R) e^{j2\pi(f_o + f_d)t} e^{-j2\pi(f_o + f_d)T_R} e^{-j2\pi(f_o + f_d)\tau'_{np}} e^{j\varphi} \qquad (2.9)$$

Complete characterization of the narrowband receive signal therefore requires quantifying the receive amplitude a_r and the signal phase. The differential delay τ'_{np} has units of time and represents the time difference of signal arrival between elements. The corresponding phase difference between elements must be found. The physical interpretation of τ'_{np} is the element to element physical separation in the $\hat{\mathbf{k}}$ direction divided by the propagation speed c. The projection of the unit vector to the target ($\hat{\mathbf{k}}$) onto the physical location vector of the elements ($\hat{\mathbf{d}}_{np}$) yields that element to element physical separation, resulting in the expression

$$\tau'_{np} = \frac{\hat{\mathbf{k}}(\theta, \phi) \cdot \hat{\mathbf{d}}_{np}}{c} \qquad (2.10)$$

$$= \frac{-nd_x \cos\theta \sin\phi - pd_z \sin\theta}{c}. \qquad (2.11)$$

Examining the third exponential term in Equation 2.9, the $e^{-j2\pi f_d \tau'_{np}}$ is approximated as $e^0 = 1$, since $f_d \tau'_{np} \approx 0$ for any expected Doppler values. Multiplying the time difference τ'_{np} by $\omega_o = 2\pi f_o$ yields the element to element phase difference,

$$\omega_o \tau'_{np} = -2\pi f_o \frac{nd_x \cos\theta \sin\phi + pd_z \sin\theta}{c}. \qquad (2.12)$$

9

A spatial frequency ϑ defines the return signal element to element phase behavior,

$$\vartheta = -\frac{\hat{\mathbf{k}}(\theta, \phi) \cdot \hat{\mathbf{d}}_{np}}{\lambda_o} \tag{2.13}$$

$$= \frac{d_x \cos\theta \sin\phi}{\lambda_o} + \frac{d_z \sin\theta}{\lambda_o}. \tag{2.14}$$

The x-axis and z-axis spatial frequencies are given by

$$\vartheta_x = \frac{d_x \cos\theta \sin\phi}{\lambda_o} \tag{2.15}$$

and

$$\vartheta_z = \frac{d_z \sin\theta}{\lambda_o}, \tag{2.16}$$

respectively. Equation (2.12) is then rewritten as

$$\omega_o \tau'_{np} = -2\pi(n\vartheta_x + p\vartheta_z). \tag{2.17}$$

Incorporating Equation (2.17) into Equation (2.6) results in

$$s_{np}(t) = a_r u(t - T_R) e^{j2\pi(f_o + f_d)t} e^{-j2\pi(f_o + f_d)T_R} e^{jf_d \tau'_{np}} e^{j2\pi(n\vartheta_x + p\vartheta_z)} e^{j\varphi} \tag{2.18}$$

Since f_o, f_d, and T_R are not functions of time and are constants for a given $s_{np}(t)$, the $e^{-j2\pi(f_o + f_d)T_R}$ terms is rolled into the random phase φ. The complete receive signal therefore becomes [3]

$$s_{np}(t) = a_r u(t - T_R) e^{j2\pi(f_o + f_d)t} e^{j2\pi(n\vartheta_x + p\vartheta_z)} e^{j\varphi}. \tag{2.19}$$

Characterization of the signal at each receiver channel is now complete. Each receiver channel performs a matched filtering operation and analog to digital conversion after stripping the carrier frequency, as depicted in Figure 2.3. The resulting signal is [3]

$$x_{mnp} = \alpha_t e^{j2\pi(n\vartheta_x + p\vartheta_z)} e^{j2\pi m\bar{\omega}}, \tag{2.20}$$

10
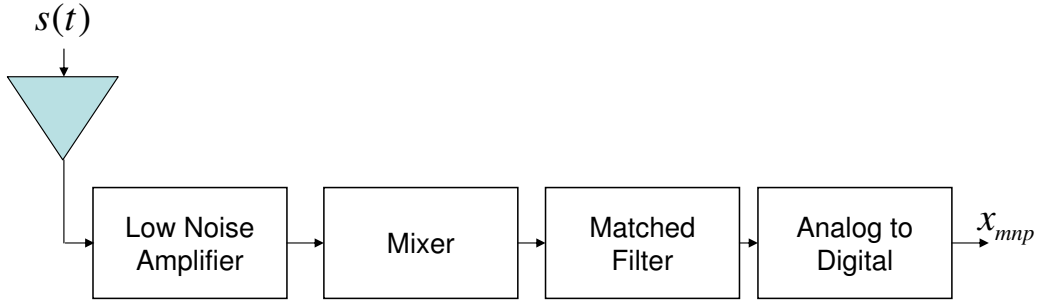
Figure 2.3: Element channel block diagram. The received signal $s(t)$ passes through a low noise amplifier, is stripped of its carrier frequency, match filtered, then converted to the digital signal x_{mnp}.

where α_t is a complex amplitude accounting for amplitude a_r and phase φ, m is the pulse within the CPI corresponding to the single time instance (range cell) the signal was sampled, and $\bar{\omega}$ is the normalized doppler frequency given by

$$\bar{\omega} = \frac{f_d}{f_r}. \tag{2.21}$$

Complex amplitude a_t accounts for all range effects of the radar range equation [9]. The matched filtering step glossed over in Equation (2.20) assumed a Doppler tolerant waveform. The step is valid as long as [5]

$$v_r \le \frac{cB}{2f_o}, \tag{2.22}$$

where f_o is the transmit frequency and B is the receiver bandwidth. An unrealistic relative velocity on the order of 90×10^3 meters per second would be required to invalidate the step for the parameters investigated in this research.

2.2.4 Formatting. For a given range cell, the radar has returns from M pulses, N azimuth channels, and P elevation channels for a total of MNP returns. These MNP returns are arranged in a compact manner suitable for linear algebra operations to integrate the returns. Arrangement is accomplished in [3] through spatial

11

(azimuth and elevation) and temporal steering vectors. The azimuth steering vector describes the element to element phase progression due to the physical separation among N azimuth channels. The elevation steering vector describes the element to element phase progression due to the physical separation among P elevation channels. And the temporal steering vector describes the pulse to pulse phase progression due to the time separation of arrival of the M pulses. The three steering vectors are arranged to represent the element to element, pulse to pulse phase progression and amplitudes of the MNP returns. This $MNP \times 1$ vector is the steering vector $\mathbf{v}_t$ to location (θ, ϕ).

The spatial steering vectors, $\mathbf{a}(\vartheta_{\mathbf{x}})$ and $\mathbf{e}(\vartheta_{\mathbf{z}})$, describe the element to element phase progression of the return. With the upper-left most element labeled the 0 reference element and the last of N azimuth channels labeled $N-1$, the element to element phase progression in azimuth becomes,

$$\mathbf{a}(\vartheta_x) = e^{j2\pi\vartheta_x(0:N-1)^T}. \tag{2.23}$$

With the upper-left most element labeled the 0 reference element and the last of P elevation channels labeled $P-1$, the element to element phase progression in elevation becomes,

$$\mathbf{e}(\vartheta_z) = e^{j2\pi\vartheta_z(0:P-1)^T}. \tag{2.24}$$

The temporal steering vector, $\mathbf{b}(\bar{\omega})$, describes the pulse to pulse phase progression of a return at a single normalized doppler frequency, $\bar{\omega}$. The pulse to pulse phase delay due to Doppler is a linear function of $\bar{\omega}$ if $\bar{\omega}$ is constant,

$$\mathbf{b}(\bar{\omega}) = e^{j2\pi\bar{\omega}(0:M-1)^T} \tag{2.25}$$

The spatial and temporal steering vectors are combined into the single steering vector $\mathbf{v}_t$ using the Kronecker product $\otimes$ [3],

$$\mathbf{v}_t(\theta, \phi) = \mathbf{e}(\vartheta_z) \otimes \mathbf{b}(\bar{\omega}) \otimes \mathbf{a}(\vartheta_x). \qquad (2.26)$$

The steering vector $\mathbf{v}_t$ captures the element to element, pulse to pulse, phase progression of a signal return from a single θ, single ϕ, and single $\bar{\omega}$. Incorporating the signal amplitude α_t yields the element to element, pulse to pulse, return signal (magnitude and phase) called the space-time snapshot and given by,

$$\boldsymbol{\chi}_t = \alpha_t \mathbf{v}_t. \qquad (2.27)$$

Actual airborne radar returns may contain multiple targets, clutter, noise, jamming, and other undesirable effects. The complete space-time snapshot therefore contains each of these factors. However, the only effects considered in this thesis are target, noise, and clutter. The complete snapshot therefore contains the target snapshot $\boldsymbol{\chi}_t$, the noise snapshot $\boldsymbol{\chi}_n$, and the clutter snapshot $\boldsymbol{\chi}_c$. The target present scenario is called the H_1 hypothesis,

$$\boldsymbol{\chi}_{\mathrm{H1}} = \boldsymbol{\chi}_t + \boldsymbol{\chi}_n + \boldsymbol{\chi}_c. \qquad (2.28)$$

The target absent scenario is called the H_0 hypothesis and contains only undesirable effects,

$$\boldsymbol{\chi}_{\mathrm{H0}} = \boldsymbol{\chi}_n + \boldsymbol{\chi}_c. \qquad (2.29)$$

The signal model and formatting are now in place. The overall goal remains characterization of the target and the interference (thermal noise and clutter for this research) environment. The next step is using the formatting framework developed to accurately characterize target, noise, and clutter space-time snapshots. These snapshots then create the models themselves. The antenna pattern is an important

13

component of the target and clutter models as it directly relates to the return ampli-tudes. The antenna pattern is defined next, followed by the target, noise, and clutter model.

2.2.5 Antenna Pattern. The magnitude of target and clutter returns depend on the power with which they are illuminated. That illumination depends on the array's antenna pattern. Antenna pattern development requires an element pattern and an array factor. Multiplication of the element pattern and array factor yield the complete antenna pattern.

The array elements are assumed identical in power and voltage patterns. A cosine pattern in both azimuth and elevation with a backlobe attenuation factor of b_e fully defines the element voltage pattern [3],

$$f(\theta, \phi) = \begin{cases} \cos\theta\cos\phi & -90^o \le \theta, \phi \le 90^o \\ b_e \cos\theta\cos\phi & 90^o > \theta, \phi > 270^o \end{cases}$$

Backlobe attenuation represents a screen behind the array [9]. The array factor for an array steered to zero azimuth and zero elevation is [1],

$$W(\theta, \phi) = \sum_{p=0}^{P-1}\sum_{n=0}^{N-1} e^{j2\pi n\vartheta_x} e^{j2\pi p\vartheta_z}. \tag{2.30}$$

Manipulation into an easily implemented form is accomplished in [3] using geometric series properties,

$$W(\theta, \phi) =$$
$$e^{j\frac{\pi dz}{\lambda_o}(P-1)\sin\theta} e^{j\frac{\pi dz}{\lambda_o}(N-1)\cos\theta\sin\phi} \frac{\sin(\frac{\pi dz}{\lambda_o}P\sin\theta)}{\sin(\frac{\pi dz}{\lambda_o}\sin\theta)} \frac{\sin(\frac{\pi dx}{\lambda_o}N\cos\theta\sin\phi)}{\sin(\frac{\pi dx}{\lambda_o}\cos\theta\sin\phi)} \tag{2.31}$$

14

Undefined points in the form given by Equation (2.31) are determined in [3] using L'Hopital's rule,

$$W(\theta, 0) = Ne^{j\frac{\pi dz}{\lambda_o}(P-1)\sin\theta} \frac{\sin(\frac{\pi dz}{\lambda_o}P\sin\theta)}{\sin(\frac{\pi dz}{\lambda_o}\sin\theta)},$$ (2.32)

$$W(0, \phi) = Pe^{j\frac{\pi dx}{\lambda_o}(N-1)\sin\phi} \frac{\sin(\frac{\pi dx}{\lambda_o}N\sin\phi)}{\sin(\frac{\pi dx}{\lambda_o}\sin\phi)},$$ (2.33)

and

$$W(0, 0) = NP.$$ (2.34)

The product of the element pattern and array factor yields the spatial array pattern in volts,

$$F(\theta, \phi) = W(\theta, \phi)f(\theta, \phi),$$ (2.35)

or can be expressed in watts,

$$G(\theta, \phi) = |W(\theta, \phi)f(\theta, \phi)|^2$$ (2.36)

$$= |W(\theta, \phi)|^2 g(\theta, \phi).$$ (2.37)

Equation (2.37) describes the radiated power in any (θ, ϕ) direction, representing the final component needed to accurately capture a target or clutter space-time snapshot. The target, noise, and clutter models are now ready to be defined.

2.2.6 *Target Model.* The $MNP \times 1$ target snapshot describes the target return amplitude, α_t, and pulse to pulse, element to element phase progression for a target at a single θ, single ϕ, and single $\bar{\omega}$,

$$\chi_t = \alpha_t \mathbf{v}_t$$ (2.38)

$$= \alpha_t \mathbf{e}(\vartheta_z) \otimes \mathbf{b}(\bar{\omega}) \otimes \mathbf{a}(\vartheta_x).$$ (2.39)

Equations (2.23) and (2.24) define the spatial steering vectors $\mathbf{a}(\vartheta_z)$ and $\mathbf{e}(\vartheta_z)$, while Equations (2.15) and (2.16) define the spatial frequencies ϑ_x and ϑ_z. Equation (2.25)

defines the temporal steering vector $\mathbf{b}(\bar{\omega})$. The normalized Doppler frequency $\bar{\omega}$ is defined [9],

$$\bar{\omega} = \frac{2v_r}{\lambda f_r}, \tag{2.40}$$

where v_r is the relative velocity between the aircraft and target, λ is the radar transmit wavelength, and f_r is the pulse repetition frequency (PRF). The relative velocity between two objects is the time rate of change of the distance between them,

$$v_r = \frac{dR}{dt}. \tag{2.41}$$

This time rate of change is the projection of the aircraft velocity vector $\vec{\mathbf{v}}_a$ onto $\hat{\mathbf{k}}$ plus the projection of the target velocity vector $\vec{\mathbf{v}}_t$ onto $\hat{\mathbf{k}}$,

$$v_r = \hat{\mathbf{k}} \cdot \vec{\mathbf{v}}_a + \hat{\mathbf{k}} \cdot \vec{\mathbf{v}}_t \tag{2.42}$$

In the stationary model of [3, 10], aircraft velocity is restricted to the $\hat{\mathbf{x}}$ direction and thus given by

$$\vec{\mathbf{v}}_a = v_a \hat{\mathbf{x}}. \tag{2.43}$$

Target velocity may include $\hat{\mathbf{x}}$, $\hat{\mathbf{y}}$, and $\hat{\mathbf{z}}$ components, denoted v_t^x, v_t^y, and v_t^z respectively,

$$\vec{\mathbf{v}}_t = v_t^x \hat{\mathbf{x}} + v_t^y \hat{\mathbf{y}} + v_t^z \hat{\mathbf{z}}. \tag{2.44}$$

The normalized Doppler frequency for a target at (θ, ϕ) is therefore

$$\bar{\omega} = 2\frac{(v_a + v_t^x) \cos\theta \sin\phi + v_t^y \cos\theta \cos\phi + v_t^z \sin\theta}{\lambda f_r}. \tag{2.45}$$

Any change in the relative velocity requires a recalculation of the normalized Doppler frequency. In the stationary model of [3, 10], the relative velocity and subsequently Doppler frequency of the target remains constant throughout the CPI. Complete characterization of $\vec{\mathbf{v}}_t$ is therefore not required. In the maneuver model of Chapter III,

16

relative velocity and subsequently Doppler frequency are not constant and characterization of $\vec{\mathbf{v}}_t$ is required.

The remaining component of the target space-time snapshot is the target amplitude, α_t. A target to noise ratio is defined [3],

$$\xi_t = \frac{P_t G(\theta,\phi) g(\theta,\phi) \lambda^2 \sigma_t}{(4\pi)^3 N_o B L_s R(\theta)^4} \tag{2.46}$$

where P_t is the transmit power, G is the array gain on transmit, g is the element gain upon receive, σ_t is the target RCS, R is the range to target, and $N_o B L_s$ accounts for system noise and losses. The target RCS is assumed independent of aspect angle and constant throughout the CPI. The complex amplitude α_t obeys

$$\mathcal{E}\{\alpha_t \alpha_t\} = \sigma^2 \xi_t, \tag{2.47}$$

where σ^2 is the receiver thermal noise power and $\mathcal{E}\{\ \}$ is the expected value operator. The thermal noise power is defined by the receiver operating temperature and bandwidth,

$$\sigma^2 = k T_o B = N_o B, \tag{2.48}$$

where k is Boltzmann's constant. In the implementation of the stationary model [3, 10], ξ_t is set equal to one. In Chapter III's maneuver model, ξ_t is recalculated for every change in platform orientation.

The target space-time snapshot is now described. Equation (2.46) and (2.47) produce the target return amplitude. The target return phase progression is described by Equations (2.23), (2.24) and (2.25). The remaining components of the stationary model are the noise and clutter characterizations.

2.2.7 Noise Model. Only internally generated receiver noise is considered and each element has its own receiver. The noise is therefore temporally and spatially white and uncorrelated. The noise correlation matrix is found with the expected value

of the outer product of the noise snapshot and its Hermitian,

$$\mathbf{R}_n = \mathcal{E}\{\boldsymbol{\chi}_n \boldsymbol{\chi}_n^H\}. \tag{2.49}$$

The subscript n throughout Equation (2.49) represents "noise", not to be confused with array elements. The lack of correlation temporally and spatially reduces the non-diagonal values of $\mathcal{E}\{\boldsymbol{\chi}_n \boldsymbol{\chi}_n^H\}$ to zero. The diagonal values take the form $\mathcal{E}\{\chi_{\mathrm{mnp}}\chi_{\mathrm{mnp}}^*\}$, where the subscript n here represents the element number. The notation is somewhat ambiguous, but follows the convention of [3, 10]. The expected value of the thermal noise voltage return times its conjugate is simply the thermal noise power, σ^2. The resulting noise correlation matrix is the thermal noise power times a $MNP \times MNP$ identity matrix [3],

$$\mathbf{R}_n = \sigma^2 \mathbf{I}_{MNP}. \tag{2.50}$$

The presence of thermal noise is vital to STAP applications. Thermal noise ensures the interference covariance matrix is invertible. The final piece of that interference environment for this research is the clutter model.

2.2.8 *Clutter Model.*   A $MNP \times 1$ clutter snapshot describes the target return amplitude, α_c, and pulse to pulse, element to element phase progression for a clutter patch at a single θ, single ϕ, and single $\bar{\omega}$,

$$\boldsymbol{\chi}_c \;=\; \alpha_c \mathbf{v}_c \tag{2.51}$$

$$\;=\; \alpha_c \mathbf{e}(\vartheta_z) \otimes \mathbf{b}(\bar{\omega}) \otimes \mathbf{a}(\vartheta_x). \tag{2.52}$$

Equations (2.23) and (2.24) define the spatial steering vectors $\mathbf{a}(\vartheta_z)$ and $\mathbf{e}(\vartheta_z)$, while Equations (2.15) and (2.16) define the spatial frequencies ϑ_x and ϑ_z. Equation (2.25) defines the temporal steering vector $\mathbf{b}(\bar{\omega})$. The normalized Doppler frequency $\bar{\omega}$ is defined in Equation (2.21. The clutter patch is stationary, meaning the relative velocity

18

depends solely on the aircraft velocity,

$$v_r = \hat{\mathbf{k}} \cdot \vec{\mathbf{v}}_a \tag{2.53}$$

$$= v_a \cos\theta \sin\phi \tag{2.54}$$

The normalized Doppler frequency of a clutter patch at (θ,ϕ) is therefore

$$\bar{\omega} = 2\frac{v_a \cos\theta \sin\phi}{\lambda f_r}. \tag{2.55}$$

Next, the clutter amplitude α_c must be characterized. The elevation angle, grazing angle, and physical attributes of the clutter patch must first be described. Referring to Figure 2.4, the spherical Earth model uses a 4/3 effective radius [3, 10],

$$a_e = r_e \frac{4}{3}, \tag{2.56}$$

where r_e represents the Earth's true radius. The effective radius model assumes a uniform vertical gradient of atmospheric refractive index, accounting for the atmospheric refraction of the propagated waveform. The elevation angle represents the angle between the line to a clutter patch at range R_c and boresight, and is found using the law of cosines [3],

$$\theta = -\sin^{-1}\left(\frac{R_c{}^2 + h_a(h_a + 2a_e)}{2R_c(h_a + a_e)}\right) \tag{2.57}$$

The grazing angle represents the angle between the line tangential to the surface at R_c and the line from the reference element to the patch at R_c [3],

$$\psi = -\sin^{-1}\left(\frac{R_c{}^2 - h_a(h_a + 2a_e)}{2R_c a_e}\right). \tag{2.58}$$

The horizon range is defined at the range at which the grazing angle is zero,

$$R_h = \sqrt{h_a^2 + 2h_a a_e}. \tag{2.59}$$
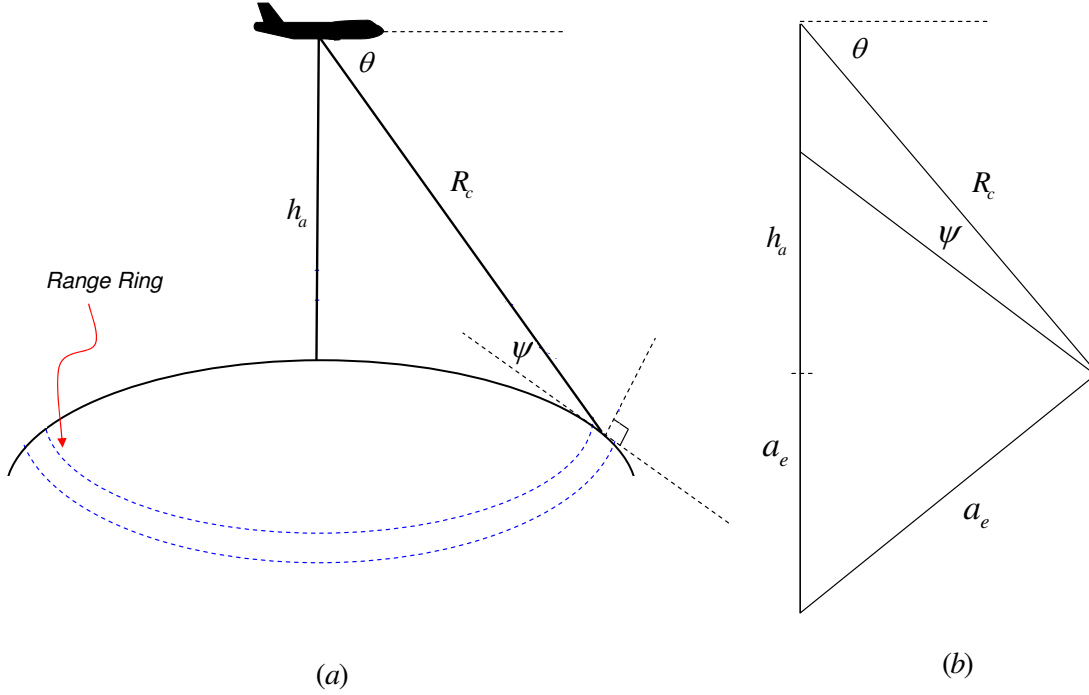
Figure 2.4: Clutter model Earth geometry. The Earth is modeled with a $4/3$ effective radius $a_e = 4/3 r_e$. The aircraft is located at height h_a. The elevation angle θ represents the angle from boresight to patches at range R_c. The grazing angle ψ represents the angle between the line tangential to the surface at R_c and the line from the reference element to the patch at R_c.

The ground plane, located in the x-y plane at height $-h_a$ and depicted in Figure 2.5, is divided into $i \times k$ individual clutter patches. The dimensions of these patches are determined by the radar operating parameters. The number of clutter patches, N_c, determines the clutter patch angular extent, $\Delta\phi$,

$$\Delta\phi = \frac{2\pi}{N_c}. \tag{2.60}$$

The radar range resolution, $\frac{c}{2\tau}$ for the uncompressed pulse, determines the clutter patch range extent, ΔR,

$$\Delta R = \frac{c}{2\tau}. \tag{2.61}$$

20
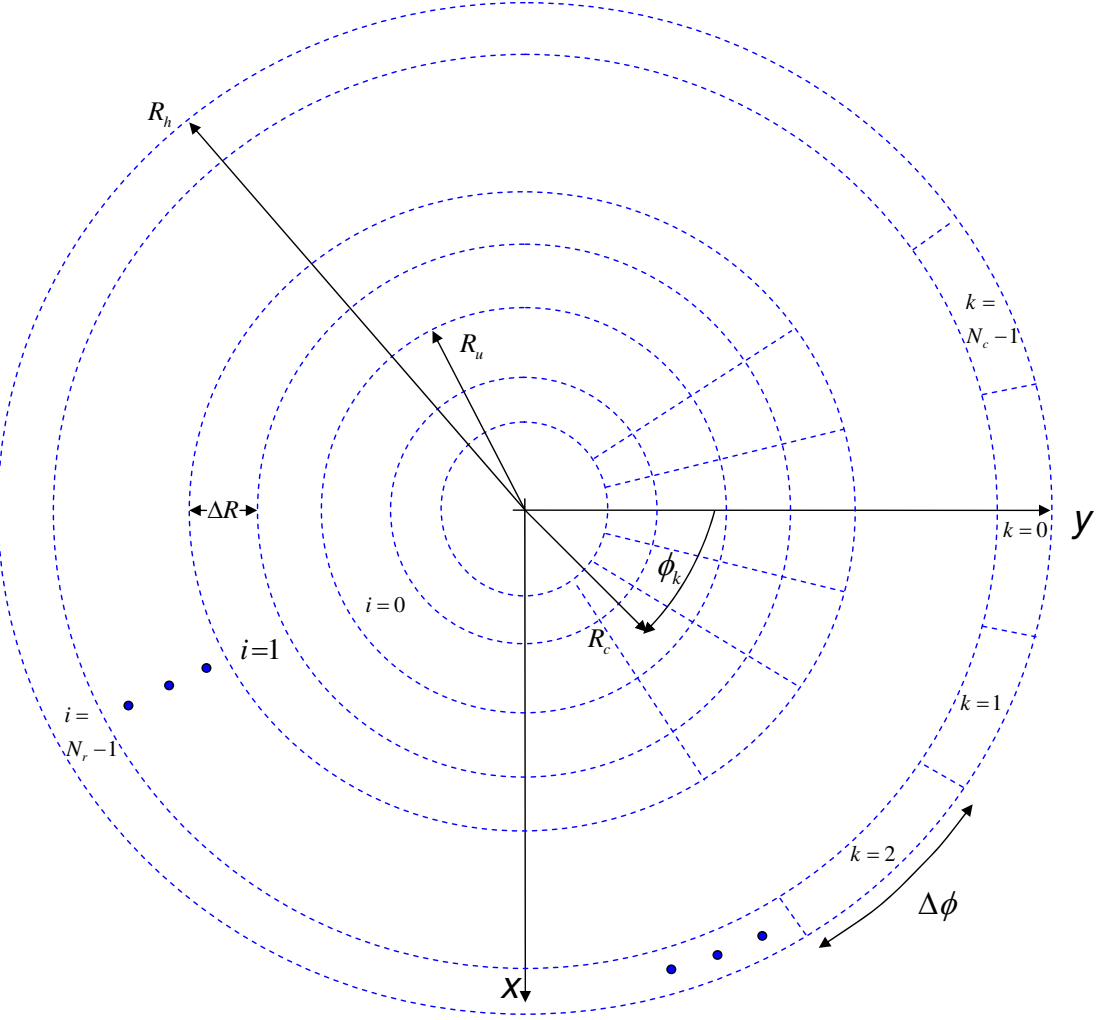
Figure 2.5: Clutter ground plane. The ground plane is divided into $i \times k$ individual clutter patches of angular extent $\Delta\phi = 2\pi/N_c$ and range extent $\Delta R = c\tau/2$. The radar's unambiguous range R_u and horizon range R_h determine the range ambiguities N_r. The range cell under test at R_c is the unambiguous ring and therefore labeled $i = 0$. Ambiguous rings are located at integer multiples of the unambiguous ring. In the condensed illustration above, the unambiguous ring at R_c is the second range ring. The first ambiguous ring, labeled $i = 1$, is therefore the fourth range ring. The next ambiguous ring (not shown), is the sixth range ring. Ambiguous rings are counted until the horizon range R_h is reached.

The number of range ambiguities, N_r, are given by,

$$
N_r = \begin{cases} \lfloor \frac{R_h}{R_u} \rfloor & R_c N_r > R_h \\ \lceil \frac{R_h}{R_u} \rceil & R_c N_r \leq R_h. \end{cases}
$$

21

With the angles and physical attributes defined, the clutter patch amplitude α_c is quantifiable. The Clutter-to-Noise-Ratio (CNR), ξ_c is defined [3],

$$\xi_c = \frac{P_t G(\theta, \phi) g(\theta, \phi) \lambda^2 \sigma_c(\theta)}{(4\pi)^3 NBL_s R_c(\theta)^4},$$ (2.62)

where P_t, G, g, λ, NBL_s, and R_c were previously defined. Unlike the target model, the clutter patch RCS, σ_c, varies with respect to the angle of incident illumination. The clutter patch RCS is a function of the clutter patch area $\Delta R \Delta \phi R$, reflectivity $\gamma \sin \psi$ [9], range R_c, and grazing angle ψ,

$$\sigma_c = \gamma \sin \psi \Delta R \Delta \phi R \sec \psi.$$ (2.63)

The patch reflectivity is modeled as constant gamma (γ) [9]. The complex amplitude α_c of a *single* clutter patch obeys [3]

$$\mathcal{E}\{\alpha_c \alpha_c^*\} = \sigma^2 \xi_c.$$ (2.64)

But the antenna array radiates in all directions, illuminating *every* $i \times k$ clutter patch. Therefore, the complete clutter space-time snapshot is the sum of $i \times k$ clutter patch snapshots [3],

$$\boldsymbol{\chi}_c = \sum_{i=0}^{N_r-1} \sum_{k=0}^{N_c-1} \alpha_{ik} \mathbf{e}(\vartheta_{z(i)}) \otimes \mathbf{b}(\bar{\omega}_{ik}) \otimes \mathbf{a}(\vartheta_{x(i,k)}).$$ (2.65)

And the complex amplitude α_{ik} obeys [3]

$$\mathcal{E}\{\alpha_{ik} \alpha_{jl}^*\} = \sigma^2 \xi_{ik} \delta_{i-j} \delta_{k-l},$$ (2.66)

22

meaning the returns from different clutter patches are uncorrelated. The final piece of the clutter model is the clutter covariance matrix from [3],

$$
\begin{aligned}
\mathbf{R}_c &= \mathcal{E}\{\boldsymbol{\chi}_c\boldsymbol{\chi}_c^H\} \\
&= \sigma^2 \sum_{i=0}^{N_r-1}\sum_{k=0}^{N_c-1} \xi_{ik}\mathbf{e}(\vartheta_z)\mathbf{e}(\vartheta_z)^H \otimes \mathbf{b}(\bar{\omega})\mathbf{b}(\bar{\omega})^H \otimes \mathbf{a}(\vartheta_x)\mathbf{a}(\vartheta_x)^H.
\end{aligned}
\qquad (2.67)
$$

Environment characterization is now complete. The target, clutter, and noise models are described and the stationary SL radar is able to be simulated. The framework and concepts of this stationary model serve as the foundation of the maneuver model in Chapter III. There are two final areas to visit before maneuver model development begins. The first covers an overview of STAP fundamentals, followed by a succinct review of previously published work modeling platform maneuver effects on STAP.

2.3 Fundamental STAP Concepts and Metrics

This section discusses four fundamental areas critical to understanding the objectives of this research. The first is general STAP concepts, discussed in Section 2.3.1. The second is sample support homogeneity discussed in Section 2.3.2. The third is clutter spectrum estimation techniques discussed in Section 2.3.3. And the final area is STAP metrics discussed in Section 2.3.4.

2.3.1 *General STAP Concepts .*   The motivation for STAP, and radar detection in general, is maximizing target detection and minimizing interference effects. The general definition for a radar filtered output is

$$
y = \mathbf{w}^H\boldsymbol{\chi},
\qquad (2.68)
$$

where $\boldsymbol{\chi}$ is all available returns, and $\mathbf{w}$ is the weight vector describing how those returns are combined. The stationary model of [3,10] reviewed in Section 2.2 provides

a method to model those radar returns $\boldsymbol{\chi}$. The scalar output y is then threshold detected to determine if a target is present. The choice of weight vectors $\mathbf{w}$ has a significant impact on detection performance. A poor selection of weights fails to mitigate the interference environment and losses in SINR and detection are incurred. Non-adaptive processing refers to the weight vector being the steering vector $\mathbf{v}$ to the radar look location (θ, ϕ), given by Equation (2.26), i.e.

$$y_{\mathrm{na}} = \mathbf{v}^H \boldsymbol{\chi}, \tag{2.69}$$

STAP seeks to optimize SINR and target detection by *intelligently* selecting the weight vector $\mathbf{w}$ based on the interference statistics of the environment. The model of [3, 10] characterizes the interference by,

$$\mathbf{R} = \mathbf{R}_n + \mathbf{R}_c, \tag{2.70}$$

where $\mathbf{R}_n$ and $\mathbf{R}_c$ are defined by Equations (2.49) and (2.67) respectively. The optimum weight vector is known as the Matched Filter (MF) and given by,

$$\mathbf{w}_{\mathrm{mf}} = \mathbf{R}^{-1}\mathbf{v}, \tag{2.71}$$

where $\mathbf{R}$ is the *known* interference covariance and $\mathbf{v}$ is the steering vector to the target location. Unfortunately, the interference environment is never known and must be estimated. The interference estimate is accomplished using snapshots at range cells (referred to as "sample support vectors") surrounding the Range-cell-Under-Test (RUT),

$$\hat{\mathbf{R}} = \frac{1}{K} \sum_{i=1}^{K} \boldsymbol{\chi}_i \boldsymbol{\chi}_i^H. \tag{2.72}$$

2.3.2   Sample Support Homogeneity .   The accuracy of the interference estimate depends on the sample support vectors used. An underlying premise of inter-

ference estimation is independent-identically-distributed (i.i.d.) sample support data. I.i.d. sample support means all support vectors have the same probability distribution and are mutually independent. Non-homogeneities within the sample support vectors cause a poor interference estimate. A Non-Homogeneity Detector (NHD) is a method to select the most homogenous sample support vectors, thereby minimizing degradation caused by non-homogeneous support data. For this research, NHD will be used to evaluate platform maneuver induced heterogeneities in the support data. The generalized inner-product,

$$\text{GIP}_\text{k} = \boldsymbol{\chi}_\text{k}^H \mathbf{R}_\text{RUT} \boldsymbol{\chi}_\text{k}. \tag{2.73}$$

provides a test for measuring the homogeneity of sample support data [11]. Using the known covariance of the RUT, the GIP compares the magnitude and phase of snapshots at surrounding range cells (designated k). The larger the GIP variance and range across a set of sample support vectors, the greater the non-homogeneity.

One of the reasons NHD is important is the unavailability of sufficient sample support for interference estimation. Real world radars have MNP degrees of freedom (DOF) on the order of several thousand. Reed's rule [2] states the number of sample support range cells required to achieve SINR within 3 dB of MF performance is two times the DOF. Rarely are there anywhere near $2MNP$ range cells available for fully adaptive processing. The lack of sufficient sample support, as well as prohibitive processing requirements for fully adaptive processing, necessitates partially adaptive processing techniques like Factored-Time Space (FTS) and Joint-Domain-Localized (JDL). While these techniques are not examined in this research, the maneuver induced heterogeneities modeled are important to these partially adaptive processes. FTS requires a minimum of $2N$ i.i.d. sample support vectors. JDL requires $2\eta_a\eta_b\eta_e$ i.i.d. sample support vectors, where η_a, η_b, and η_e are the DOF used. Therefore, maneuver effects on data homogeneity will influence iid sample support availability and selection.

The development of the maneuver model is the primary research focus, followed by examination of maneuver effects on MF performance and data homogeneity. While the GIP provides an evaluation of sample support homogeneity, clutter spectral estimation allows insight into the interference environment and potential impact on detection performance. Two spectral estimation techniques are employed in this effort.

2.3.3 Spectral Estimation .   The first spectral technique used is the low-resolution Signal Match (SM). The SM technique steers through the interference data with the steering vector $\mathbf{v}$, producing a maximum when the steering vector and interference data match. The technique produces spurious sidelobes due to the 3-D discrete Fourier transform equivalence of the $MNP \times 1$ steering vector used in the [3,10] model and this research. These sidelobes are not a part of the clutter model, but are what the radar "sees" when processing interference data with the the steering vector and are thus well suited for detection purposes. The SM spectral estimate is given by [5]

$$P = \frac{\mathbf{v}^H \mathbf{R} \mathbf{v}}{\mathbf{v}^H \mathbf{v}}. \tag{2.74}$$

The second technique is the high-resolution Minimum-Variance Estimate (MVE). The MVE technique, given by [5]

$$P_{\mathrm{mve}} = (\mathbf{v}^H \mathbf{R}^{-1} \mathbf{v})^{-1}, \tag{2.75}$$

and seeks minimums and provides the location of interference in the environment. MVE amplitude information is useless as it only provides interference source location. The MVE leads to realistic spectral estimates if the signal is composed of single spectral lines, but unrealistic estimates if it is a continuous spectrum [5].

2.3.4 Metrics .   Output SINR is one of the most common metrics for radar performance. As its name suggests, it is a ratio of the desired target power over the

undesired interference power. Output SINR is given by

$$\text{SINR} = \frac{\sigma^2 \xi_t \mid \mathbf{w}^H \mathbf{v}_t \mid^2}{\mathbf{w}^H \mathbf{R} \mathbf{w}}, \tag{2.76}$$

where $\mathbf{v}_t$ is the steering vector to the target, ξ_t is the Signal-to-Noise-Ratio, and $\mathbf{w}$ is the weight vector applied. Another useful metric is SINR Loss,

$$\text{SINR}_L = \frac{\text{SINR}}{\xi_t MNP}. \tag{2.77}$$

SINR Loss references the output SINR to the thermal noise only situation. SINR Loss is a convenient tool to compare results from scenarios with different MNP values since it is normalized by MNP. The final metric used is the Improvement Factor. The Improvement factor is the ratio of the output SINR to input SINR. The larger the improvement factor, the better the radar is adapting to the interference environment. The improvement factor is given by,

$$\text{IF} = \frac{\text{SINR} \xi_t}{1 + \xi_c}. \tag{2.78}$$

where ξ_c is the Clutter-to-Noise-Ratio.

These metrics are used in Chapter IV to analyze the effects of platform maneuver.

2.4 Literature Review

Peter G. Richardson first explored platform maneuver effects on STAP in 1997 [7]. Richardson focused on roll effects for the forward-looking (FL) circular planar array and their implications to airborne intercept applications. The aircraft velocity vector was fixed in [7], while the maneuver model developed in Chapter III has the ability to model a fixed or moving aircraft velocity vector. Richardson observed an 11 dB drop in SINR when roll was introduced, but predicted motion compensated steering would reduce the degradation. Motion compensated steering is not investigated in this re-

search, since the main objectives are model development and homogeneous sample support investigation. However, the maneuver model developed has the ability to fully simulate motion compensated steering.

In 1998 and 1999, Richardson extended his original work for the FL circular planar array and determined roll rates as small as 0.005 degrees per PRI significantly impacted slow moving target detection [8]. These results were for slow moving ground targets with the antenna steered to the ground location. He also showed allowing aircraft velocity vector movement had minimal impact on the results. This minimum impact was also observed in the Chapter III maneuver model developed. A significant portion of Richardson's work in [7,8] was roll effects on jammer rejection performance in the FL scenario.

Minimal research was published after Richardson's until George M. Herbert revisited the topic in 2005 [4]. Herbert investigated roll, pitch, and yaw effects for the FL planar array. Using similar simulation parameters to Richardson in [7] and [8], Herbert concluded roll effects were not nearly as significant as [7, 8] suggested. Herbert attributed the pessimistic results of [7, 8] to discontinuities in the antenna pattern and a simplistic clutter model. Additionally, Herbert investigated motion compensated steering and determined it indeed compensated the negative effects of platform maneuver as Richardson suggested.

The research to follow builds a framework to model pitch, roll, and yaw platform maneuver for the SL planar array. Several deviations from the previously published work of Richardson and Herbert exist. The most obvious is the SL array is investigated instead of the FL. Next, the STAP model and framework is based on that of [10] and [3]. Third, aircraft velocity vector movement is allowed. Motion compensated steering will not be explored and the antenna mainbeam is steered to boresight in this research. And finally, both linear and planar arrays are modeled instead of circular or linear arrays. Rotation rates, total degree of rotations, and CPI lengths are similar to [4, 7, 8].

The overall goal of both the stationary model of [3,10] and the maneuver model developed in this research are accurate characterization of the interference environment. The approaches taken are similar, but the paths are slightly different. Chapter II describes the stationary model and the approach, while Chapter III describes the maneuver model path. Once the interference environment is characterized, STAP can be applied in Chapter IV. The stationary model, the foundation of the maneuver model developed in Chapter III, is presented next.

III. Platform Maneuver Model for Side Looking Arrays

The popular model described in Chapter II assumed the aircraft platform was perfectly stationary throughout the coherent processing interval (CPI). Abandoning that assumption and allowing platform maneuver creates a more realistic model and is the focus of this research. An important point concerning the meaning of "maneuver" in this research. Range walk refers to the aircraft moving forward in the direction of travel during the CPI. Range walk decorrelation effects have been derived and simulated in [5]. The focus of this research is platform rotation, *not* range walk. Therefore, the aircraft remains fixed in space while the platform rotates for this model.

The previous model of [3, 10] serves as the maneuver model foundation. Development of the platform maneuver STAP model begins with the antenna and physical geometry. A mathematical framework incorporating platform maneuver about any axis is developed. Once the framework is constructed, the rotation behavior of the platform itself is defined. The result is propagated through the development of new signal, target, and clutter models. The thermal noise model is unaffected by platform maneuver and remains unchanged. Major deviations from the previous model include: a single location now has M different (θ, ϕ) pairs and M $\hat{\mathbf{k}}$ unit vectors, the aircraft velocity vector changes each pulse, targets and clutter are illuminated differently each pulse, and target and clutter Doppler frequencies change each pulse. Additionally, modification of the the stationary model formatting is required. All steering vectors in the maneuver model are $MNP \times 1$, versus $M \times 1$, $N \times 1$, or $P \times 1$ in the stationary model. Maneuver model space-time snapshots are created with the Hadamard product ($\odot$), versus the Kronecker product ($\otimes$) in the stationary model. The foundation of these differences begins with the geometry and rotation behavior.

3.1 Geometry and Rotation

Consider the side-looking (SL) antenna array mounted on an aircraft, as depicted in Figures 3.1- 3.2 and discussed in Chapter II. Recall the unit vector from
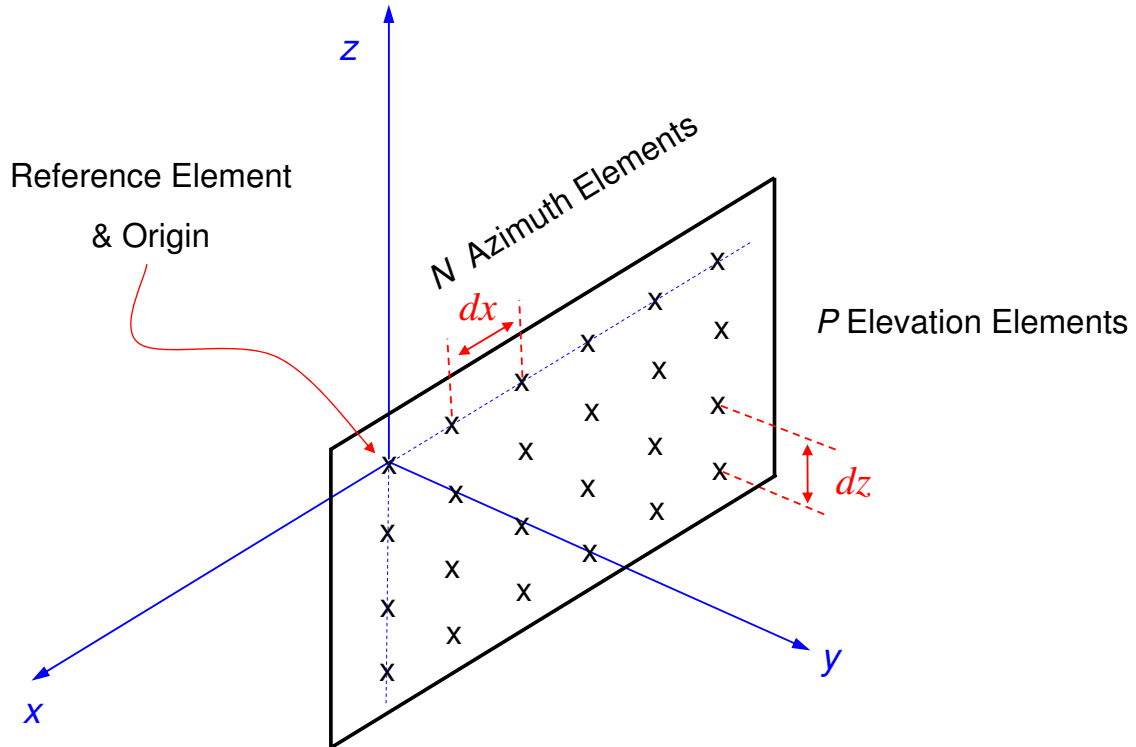
Figure 3.1:   Antenna array geometry. The antenna array is oriented in the x-z plane. Its reference element, defined as the upper-left most element, serves as the origin of the cartesian and radar coordinate systems. The elements are uniformly spaced with inner-element spacings of dx in the x direction and dz in the z direction. The N azimuth channels are numbered 0 to $N-1$, and the P elevation channels 0 to $P-1$.

the reference element to the np^{th} element is [3]

$$\hat{\mathbf{d}}_{np} = -nd_x\hat{\mathbf{x}} - pd_z\hat{\mathbf{z}}. \tag{3.1}$$

!   The antenna array always defines the reference coordinate system for this research. Any platform rotation equates to a rotation of the reference coordinate system.
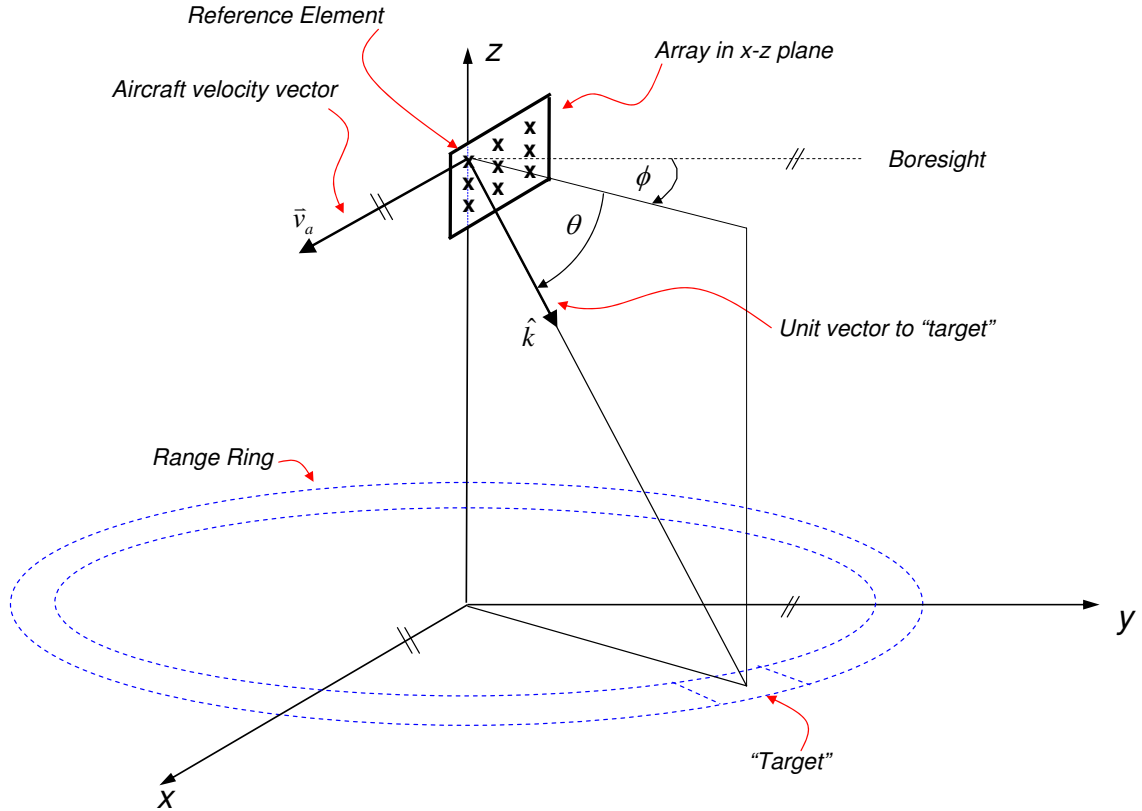
Figure 3.2: Radar platform geometry. The array is mounted on an aircraft in a side-looking (SL) configuration with boresight defined in the $\hat{\mathbf{y}}$ direction. The aircraft travels at speed v_a in the $\hat{\mathbf{x}}$ direction. The vector $\hat{\mathbf{k}}$ is the unit vector from the reference element to the target.

The (x,y,z) coordinates of a target or clutter patch at elevation angle θ, azimuth angle ϕ, and range R_t are

$$x = R_t \cos\theta \sin\phi, \tag{3.2}$$

$$y = R_t \cos\theta \cos\phi, \tag{3.3}$$

and

$$z = R_t \sin\theta. \tag{3.4}$$

The elevation and azimuth angles can be expressed as

$$\theta \;=\; -\sin^{-1}\left(\frac{z}{R_t}\right), \tag{3.5}$$

and

$$\phi \;=\; \cos^{-1}\left(\frac{y}{R_t \cos\theta}\right) \tag{3.6}$$

$$\;=\; \cos^{-1}\left(\frac{y}{R_t \cos\left(\sin^{-1}(\frac{z}{R_t})\right)}\right) \tag{3.7}$$

The negative sign in Equation (3.5) ensures the elevation angle to the ground is negative, as expected in radar coordinates. Figure 3.2 never changed in the stationary model and introduction of maneuver at this point serves as the start of the maneuver model.

The platform is allowed to rotate about the reference element about any axis. Rotations about the x,y, and z axes depicted in Figure 3.3 correspond to aircraft roll, pitch, and yaw respectively. Consider an arbitrary point located at (θ, ϕ) in Figure 3.2. The antenna then rotates about any axis. That point at (θ, ϕ) still resides in the same physical space, but its position *relative to the antenna* has changed. The overall goal is accurate characterization of the clutter and target. The snapshots depend on the scenario geometry and the resulting radar angles (and Doppler values) to the location. Therefore, the (θ, ϕ) location's new position relative to the rotated antenna must be found. A mathematical framework is needed to describe the radar coordinates to any location, with any amount of platform pitch, roll, or yaw. The mathematical framework is constructed with rotation matrices.

A general linear rotation about an axis can be described with a rotation matrix. Rotations about all three $(x$,y,$z)$ axes can be described using Euler's rotation theorem. No universal convention exists defining rotation direction, i.e. clockwise (CW) or
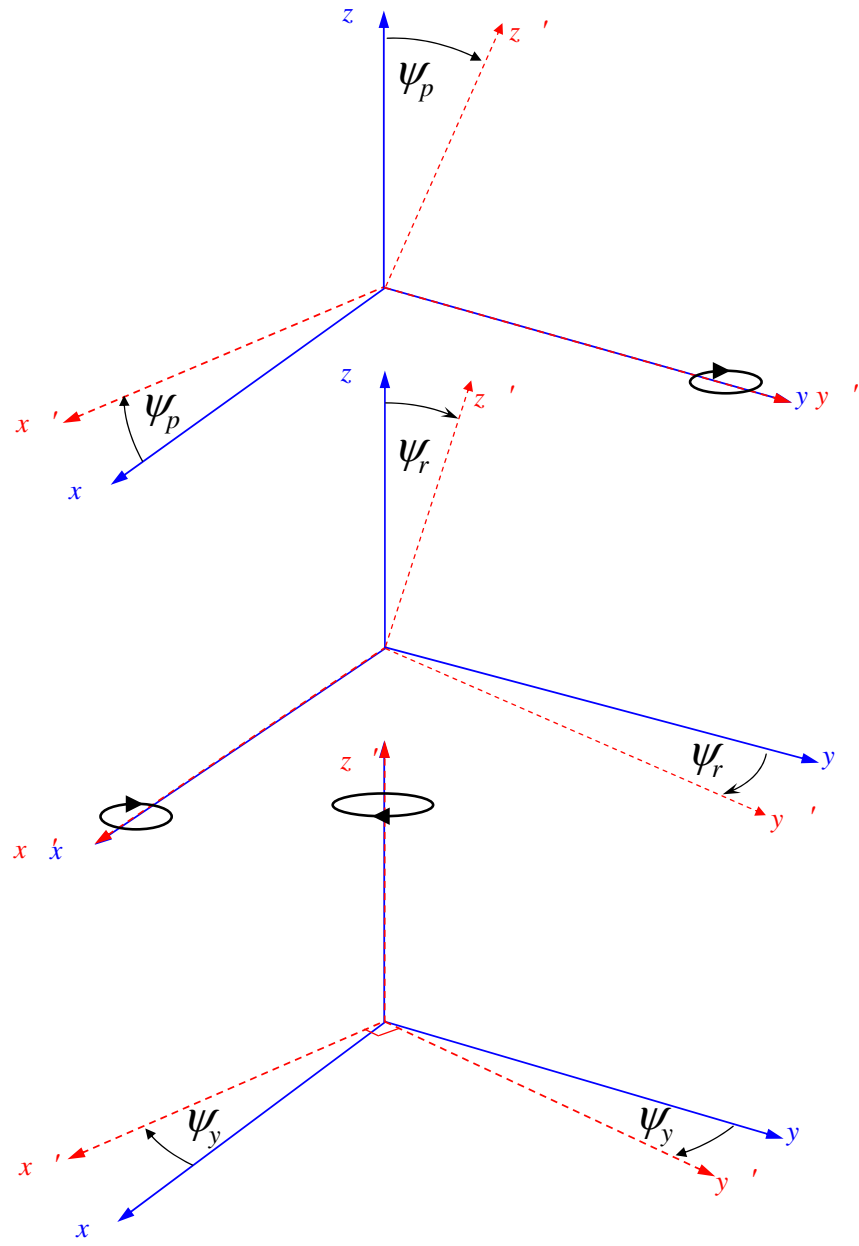
Figure 3.3:   Rotation illustration. The antenna rotates about the x, y, or z axis corresponding to roll (middle picture), pitch (top picture), and yaw (bottom picture) respectively. Rotation occurs about the reference element and the antenna array resides in the x'-z' plane. The reference coordinate system therefore rotates, designated by the primed notation. Rotation can occur in a clockwise or counter-clockwise direction, although only clockwise rotation is depicted above. The subscript corresponds to the type of rotation. Subscript "p" is pitch, "r" is roll, and "y" is yaw.
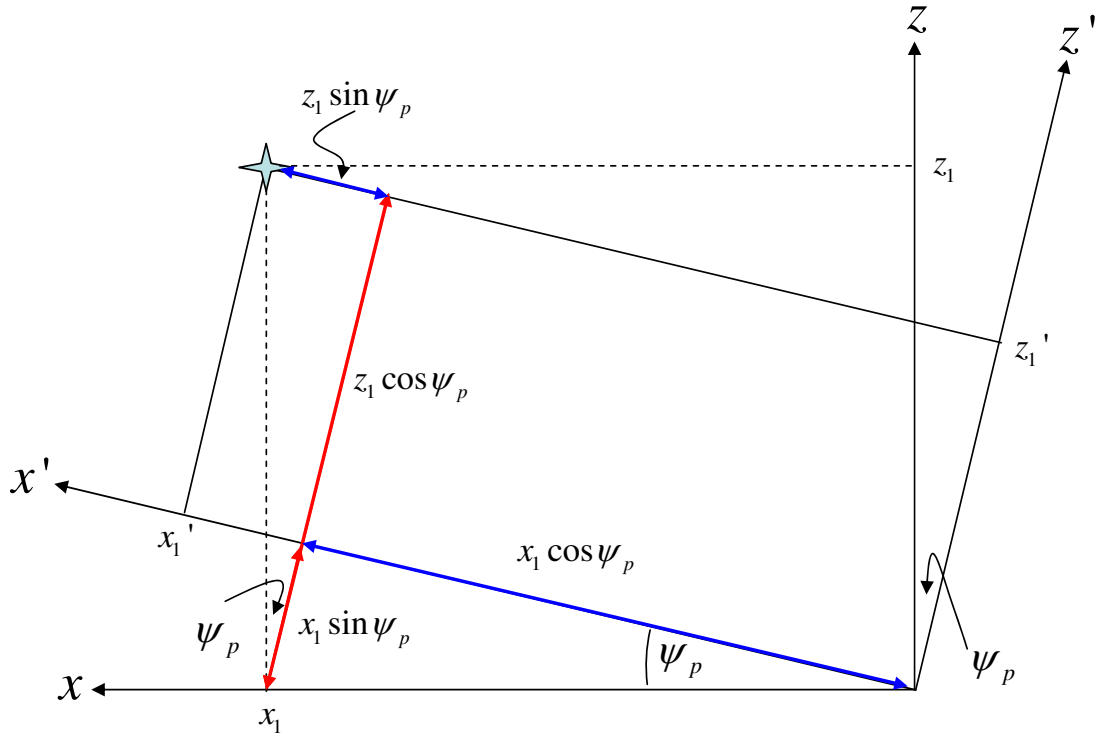
Figure 3.4: Pitch up geometry. The array reference element serves as the origin of the x-y-z and x'-y'-z' cartesian coordinate systems. The coordinate system rotates ψ_p degrees in a CW direction about the reference element and y-axis, corresponding to the aircraft's nose rotating upward. The rotated coordinates (x'_1, y'_1, z'_1) to the point (x_1, y_1, z_1) are then found.

counter-clockwise (CCW). The convention used for this research is based on the pilot's perspective.

> ⚠️ 'Pitch up' refers to a CW rotation about the y-axis, i.e. the aircraft's nose rotates skyward. 'Roll right' refers to a CCW rotation about the x-axis, i.e. the aircraft's right wing dips and left wing rises. 'Yaw right' refers to a CW rotation about the z-axis, i.e. the aircraft's nose rotates right.

Consider the case of pitch up, depicted in Figure 3.4. The original target is located at (x_1, z_1). The platform rotates ψ_p CW about the y-axis at the origin of the x-y-z coordinate system (the reference element). The original target has not moved and exists at the exact same location in physical space. However, the relative frame of reference defined by the antenna array's location has changed. Inspection of Figure

3.4 yields the new coordinates of the target in the rotated x'-y'-z' coordinate system,

$$x'_1 = x_1 \cos \psi_p + z_1 \sin \psi_p, \tag{3.8}$$

$$y'_1 = y_1, \tag{3.9}$$

$$z'_1 = -x_1 \sin \psi_p + z_1 \cos \psi_p. \tag{3.10}$$

The relationship can be expressed in matrix form,

$$\begin{bmatrix} x'_1 \\ y'_1 \\ z'_1 \end{bmatrix} = \begin{bmatrix} \cos \psi_p & 0 & \sin \psi_p \\ 0 & 1 & 0 \\ -\sin \psi_p & 0 & \cos \psi_p \end{bmatrix} \begin{bmatrix} x_1 \\ y_1 \\ z_1 \end{bmatrix}.$$

The 3×3 rotation matrix describes the location of the target with respect to the y-axis rotated platform frame of reference. The matrix is dubbed $\mathbf{P}_p^u$ with subscript p referring to rotation type pitch and superscript u to rotation direction up,

$$\mathbf{P}_p^u(\psi_p) = \begin{bmatrix} \cos \psi_p & 0 & \sin \psi_p \\ 0 & 1 & 0 \\ -\sin \psi_p & 0 & \cos \psi_p \end{bmatrix}.$$

The next case considered is roll right, depicted in Figure 3.5. The platform rotates ψ_r degrees about the reference element and x-axis. Inspection of Figure 3.5 reveals the relationship,

$$x'_1 = x_1, \tag{3.11}$$

$$y'_1 = y_1 \cos \psi_r + z_1 \sin \psi_r, \tag{3.12}$$

$$z'_1 = -y \sin \psi_r + z \cos \psi_r. \tag{3.13}$$
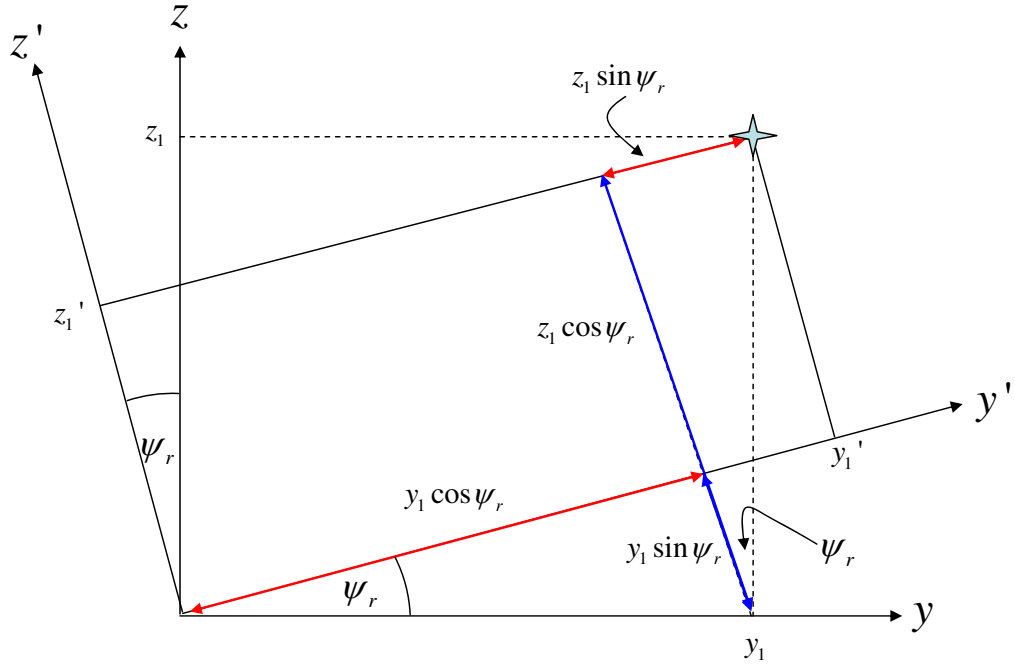
Figure 3.5:   Roll right geometry. The array reference element serves as the origin of the x-y-z and x'-y'-z' cartesian coordinate systems. The coordinate systems rotates ψ_r degrees in a CCW direction about the reference element and x-axis, corresponding to the aircraft's right wing dipping downward. The rotated coordinates (x'_1, y'_1, z'_1) to the point (x_1, y_1, z_1) are then found.

The relationship in matrix form is,

$$
\begin{bmatrix} x'_1 \\ y'_1 \\ z'_1 \end{bmatrix} = \begin{bmatrix} 1 & 0 & 0 \\ 0 & \cos\psi_r & \sin\psi_r \\ 0 & -\sin\psi_r & \cos\psi_p \end{bmatrix} \begin{bmatrix} x_1 \\ y_1 \\ z_1 \end{bmatrix}.
$$

This 3×3 rotation matrix describes the location of the target with respect to the x-axis rotated platform frame of reference. The matrix is dubbed $\mathbf{P}^r_r$ with subscript
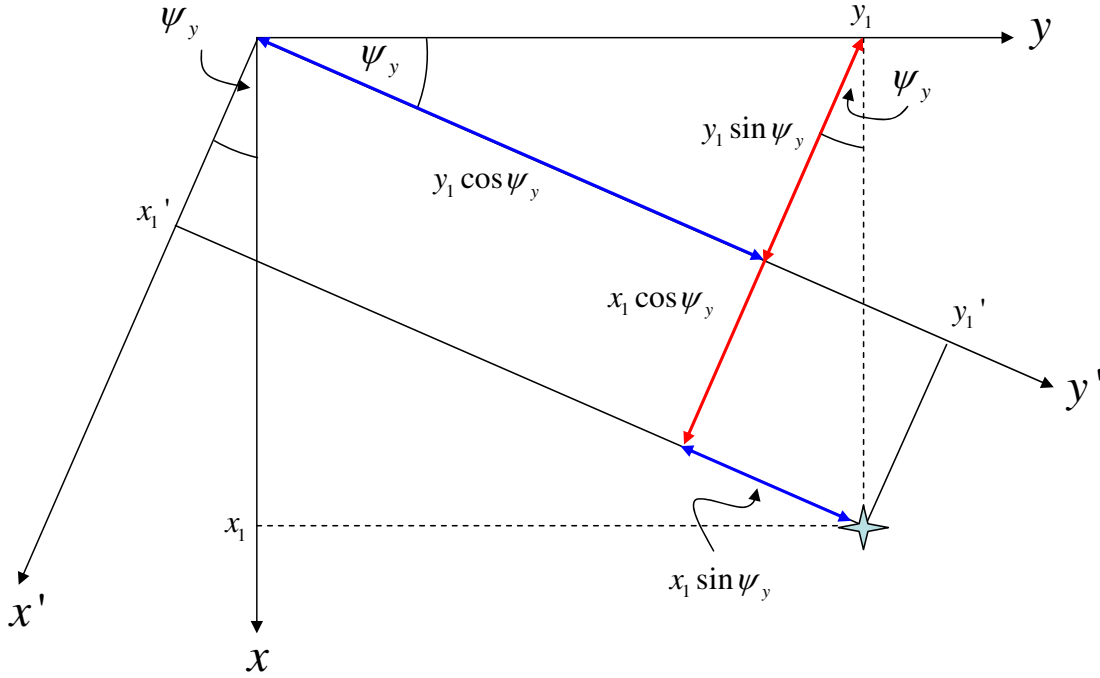
Figure 3.6: Yaw right geometry. The array reference element serves as the origin of the x-y-z and x'-y'-z' cartesian coordinate systems. The coordinate systems rotates ψ_y degrees in a CW direction about the reference element and z-axis, corresponding to the aircraft's nose rotating to the right. The axis label "y" and rotation type designated by subscript "y" in ψ_y are unrelated. The notation ambiguity is cleared with the context of use. The rotated coordinates (x'_1, y'_1, z'_1) to the point (x_1, y_1, z_1) are then found.

r referring to rotation type roll and superscript r to rotation direction right,

$$\mathbf{P}^r_r(\psi_p) = \begin{bmatrix} 1 & 0 & 0 \\ 0 & \cos\psi_r & \sin\psi_r \\ 0 & -\sin\psi_r & \cos\psi_r \end{bmatrix}.$$

Rotation about the y (pitch) and x (roll) axes have been defined, leaving rotation about the z-axis (yaw). Figure 3.6 depicts the platform yawing right a total of ψ_y degrees. Inspection of Figure 3.6 reveals the relationship,

$$x_1' = x_1 \cos \psi_y - y_1 \sin \psi_y, \qquad (3.14)$$

$$y_1' = x_1 \sin \psi_y + y_1 \cos \psi_y, \qquad (3.15)$$

$$z_1' = z_1. \qquad (3.16)$$

And the relationship in matrix form is,

$$
\begin{bmatrix} x_1' \\ y_1' \\ z_1' \end{bmatrix} = \begin{bmatrix} \cos \psi_y & -\sin \psi_y & 0 \\ \sin \psi_y & \cos \psi_y & 0 \\ 0 & 0 & 1 \end{bmatrix} \begin{bmatrix} x_1 \\ y_1 \\ z_1 \end{bmatrix} .
$$

This 3×3 rotation matrix describes the location of the target with respect to the z-axis rotated platform frame of reference. The matrix is dubbed $\mathbf{P}_y^r$ with subscript r referring to rotation type yaw and superscript r to rotation direction right,

$$
\mathbf{P}_y^r(\psi_y) = \begin{bmatrix} \cos \psi_y & -\sin \psi_y & 0 \\ \sin \psi_y & \cos \psi_y & 0 \\ 0 & 0 & 1 \end{bmatrix} .
$$

Realistically, the platform is not restricted to *upward* pitch, *right* roll, and *right* yaw. The platform may maneuver opposite each of these respective directions, necessitating examination of *downward* pitch, *left* roll, and *left* yaw. These three maneuver scenarios are depicted in Figures 3.7-3.9. And the rotation matrices corresponding to pitch down, roll left, and yaw left are

$$
\mathbf{P}_p^d(\psi_p) = \begin{bmatrix} \cos \psi_p & 0 & -\sin \psi_p \\ 0 & 1 & 0 \\ \sin \psi_p & 0 & \cos \psi_p \end{bmatrix} ,
$$

$$
\mathbf{P}_r^l(\psi_r) = \begin{bmatrix} 1 & 0 & 0 \\ 0 & \cos \psi_r & -\sin \psi_r \\ 0 & \sin \psi_r & \cos \psi_r \end{bmatrix} ,
$$
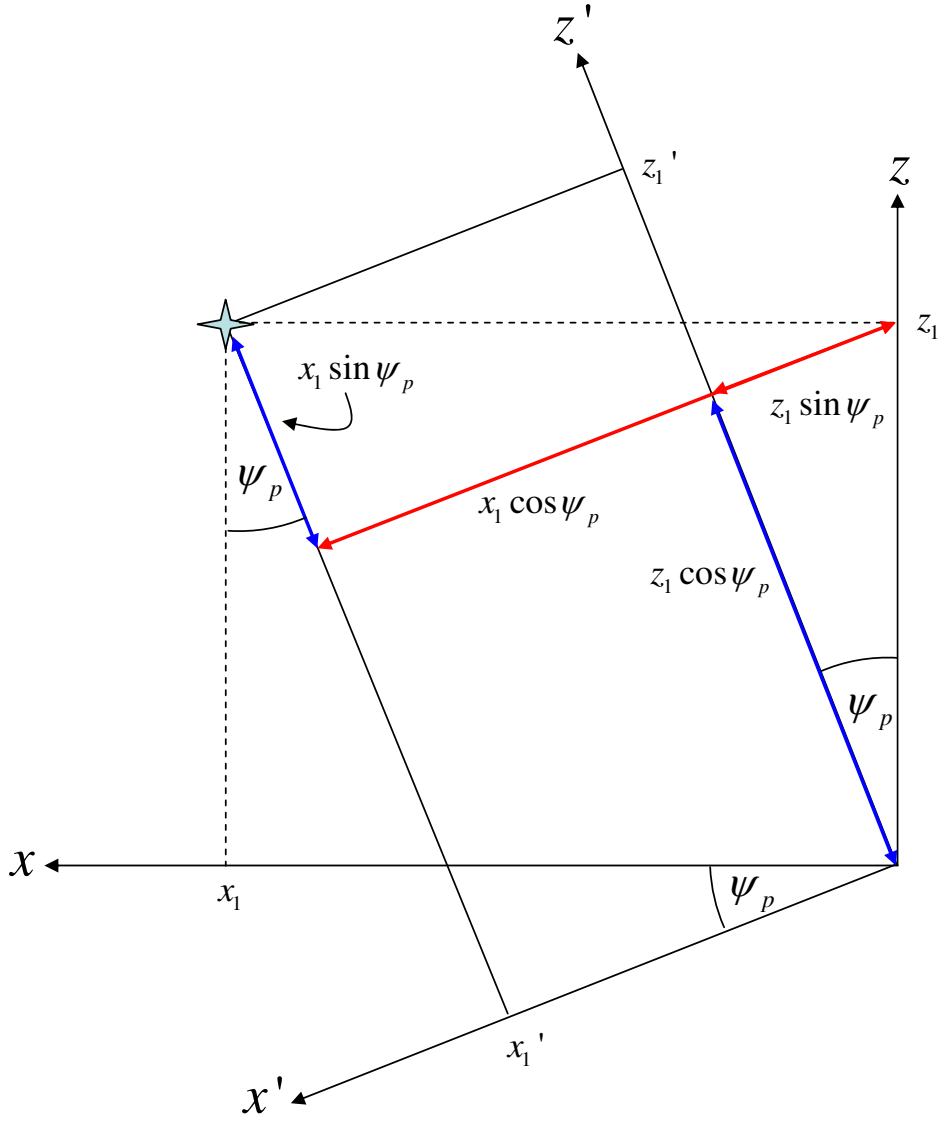
Figure 3.7: Pitch down geometry. The array reference element serves as the origin of the x-y-z and x'-y'-z' cartesian coordinate systems. The coordinate systems rotates ψ_p degrees in a CCW direction about the reference element and zy-axis, corresponding to the aircraft's nose rotating to the right. The rotated coordinates (x'_1, y'_1, z'_1) to the point (x_1, y_1, z_1) are then found.

and

$$\mathbf{P}_y^l(\psi_y) = \begin{bmatrix} \cos\psi_y & \sin\psi_y & 0 \\ -\sin\psi_y & \cos\psi_y & 0 \\ 0 & 0 & 1 \end{bmatrix},$$

40
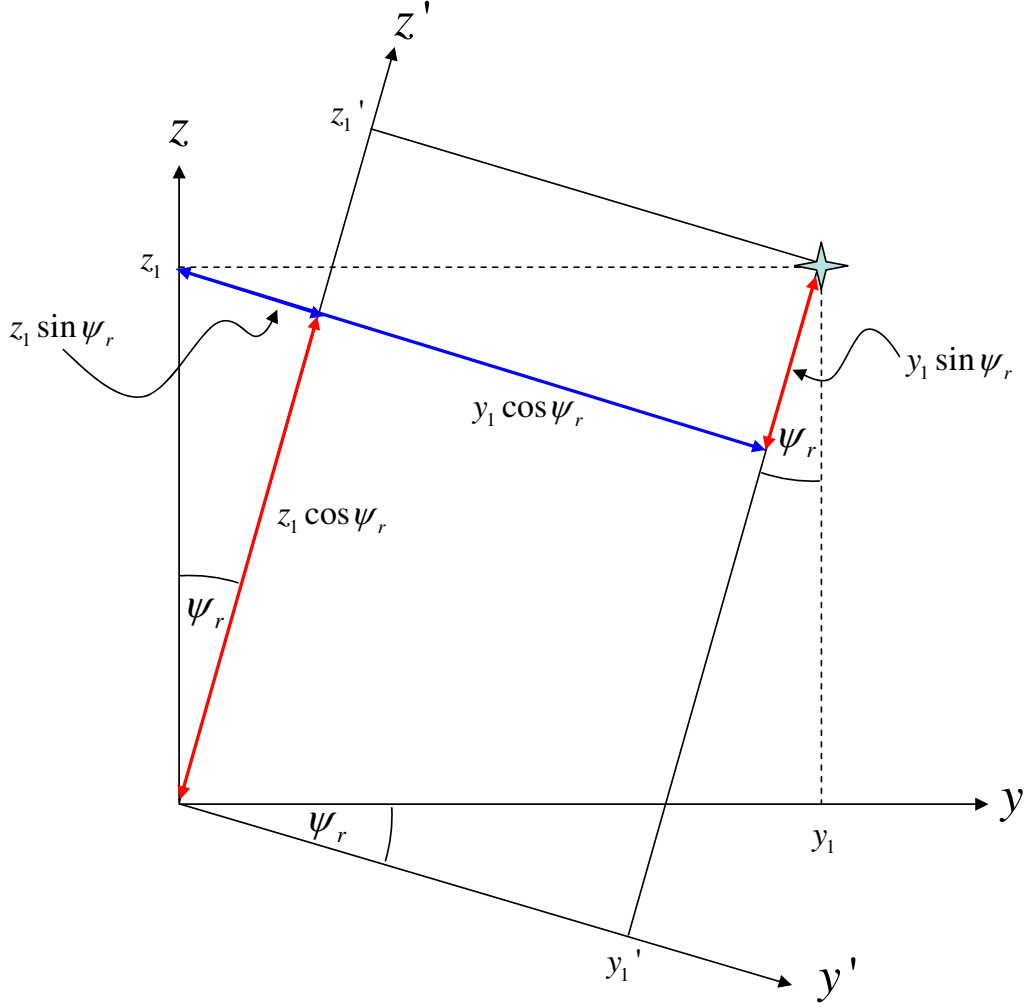
Figure 3.8: Roll left geometry. The array reference element serves as the origin of the x-y-z and x'-y'-z' cartesian coordinate systems. The coordinate systems rotates ψ_r degrees in a CCW direction about the reference element and x-axis, corresponding to the aircraft's left wing dipping and right wing rising. The rotated coordinates (x'_1, y'_1, z'_1) to the point (x_1, y_1, z_1) are then found.

respectively. The six rotation matrices, $\mathbf{P}_p^u$, $\mathbf{P}_p^d$, $\mathbf{P}_r^r$, $\mathbf{P}_r^l$, $\mathbf{P}_y^r$, $\mathbf{P}_y^l$, enable description of any rotation (CW or CCW) about any axis. Each reduces to an identity matrix when $\psi_p = \psi_r = \psi_y = 0$, as expected. Examination of pitch matrices $\mathbf{P}_p^u$ and $\mathbf{P}_p^d$ reveal the matrices are nearly identical with the exception of the sign of $\sin \psi_p$. The same similarity holds for roll matrices $\mathbf{P}_r^r$ and $\mathbf{P}_r^l$, and yaw matrices $\mathbf{P}_y^r$ and $\mathbf{P}_y^l$. The
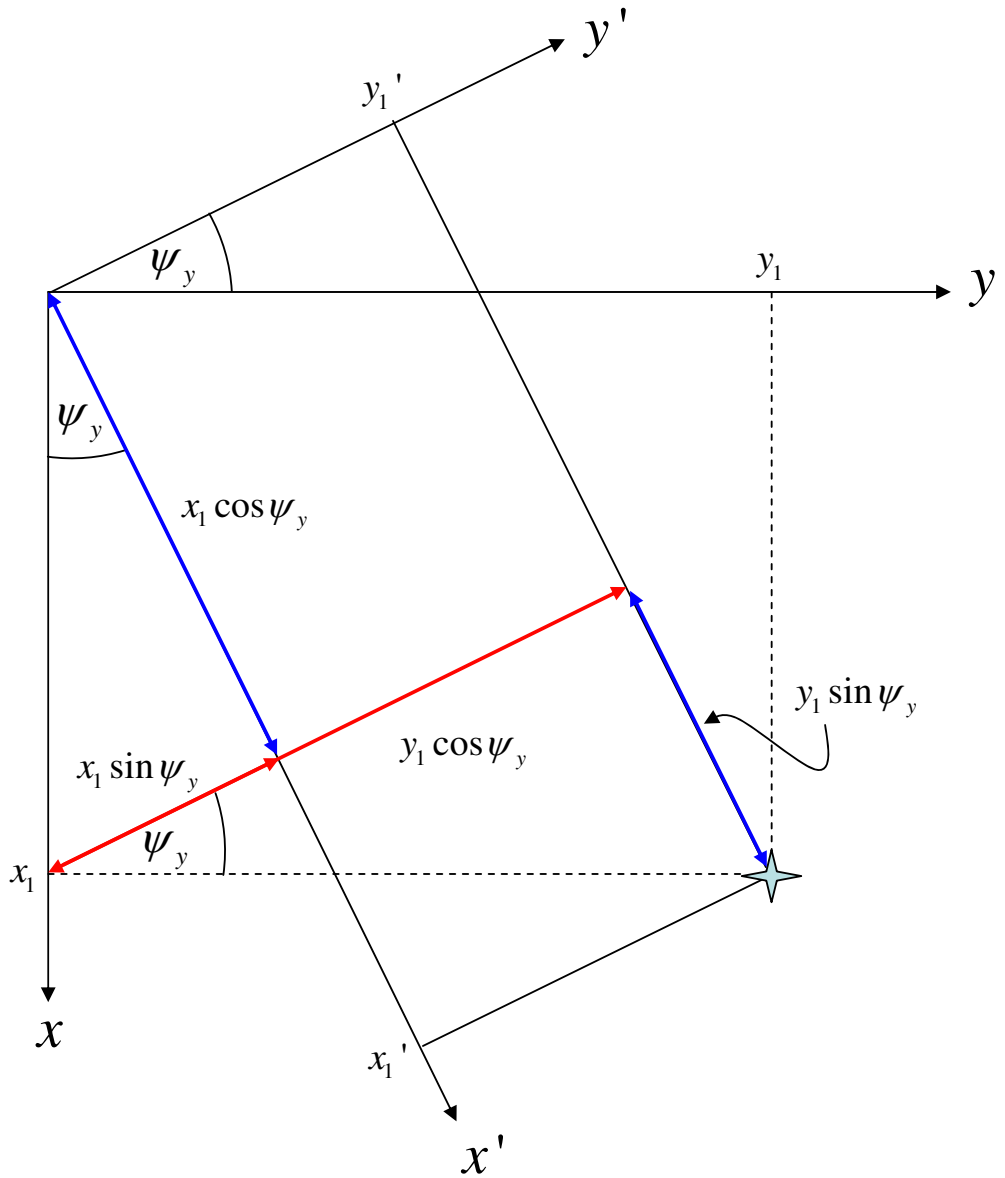
Figure 3.9: Yaw left geometry. The array reference element serves as the origin of the x-y-z and x'-y'-z' cartesian coordinate systems. The coordinate systems rotates ψ_y degrees in a CCW direction about the reference element and z-axis, corresponding to the aircraft's nose rotating to the left. The rotated coordinates (x_1',y_1',z_1') to the point (x_1,y_1,z_1) are then found.

oddness property of the sin function allows reduction from the six rotation matrices

to three: $\mathbf{P}_p$, $\mathbf{P}_r$, and $\mathbf{P}_y$,

$$\mathbf{P}_p(\psi_p) = \begin{bmatrix} \cos \psi_p & 0 & \sin \psi_p \\ 0 & 1 & 0 \\ -\sin \psi_p & 0 & \cos \psi_p \end{bmatrix},$$

$$\mathbf{P}_r(\psi_r) = \begin{bmatrix} 1 & 0 & 0 \\ 0 & \cos \psi_r & \sin \psi_r \\ 0 & -\sin \psi_r & \cos \psi_r \end{bmatrix},$$

and

$$\mathbf{P}_y(\psi_y) = \begin{bmatrix} \cos \psi_y & -\sin \psi_y & 0 \\ \sin \psi_y & \cos \psi_y & 0 \\ 0 & 0 & 1 \end{bmatrix}.$$

! Convention for this research:
A positive ψ_p refers to a CW rotation about the y-axis, i.e. 'Pitch Up'.
A positive ψ_r refers to a CCW rotation about the x-axis, i.e. 'Roll Right'.
A positive ψ_y refers to CW rotation about the z-axis, i.e. 'Yaw Right'.

The complete rotation matrix describing any rotation three axes is found by

$$\mathbf{P}_{p,r,y}(\psi_p, \psi_r, \psi_y) = \mathbf{P}_p(\psi_p) \times \mathbf{P}_r(\psi_r) \times \mathbf{P}_y(\psi_y). \tag{3.17}$$

However, the order of operations will affect the rotation being modeled. The rotation $\mathbf{P}_p(\psi_p) \times [\mathbf{P}_r(\psi_r) \times \mathbf{P}_y(\psi_y)]$ is not the same as $[\mathbf{P}_p(\psi_p) \times \mathbf{P}_r(\psi_r)] \times \mathbf{P}_y(\psi_r)$ or $[\mathbf{P}_y(\psi_p) \times \mathbf{P}_r(\psi_y)] \times \mathbf{P}_p(\psi_r)$. In other words, the order of successive rotations impacts the overall rotation and the resulting geometry. A simple example depicted in Figure 3.10 illustrates the concept. Three rotations are performed in different orders, resulting in two different results. The different resulting geometries is a consequence of the approach taken in this research. Specifically, the rotation matrices describe the location of point (x,y,z) in the (x',y',z') rotated reference coordinate system. The as-
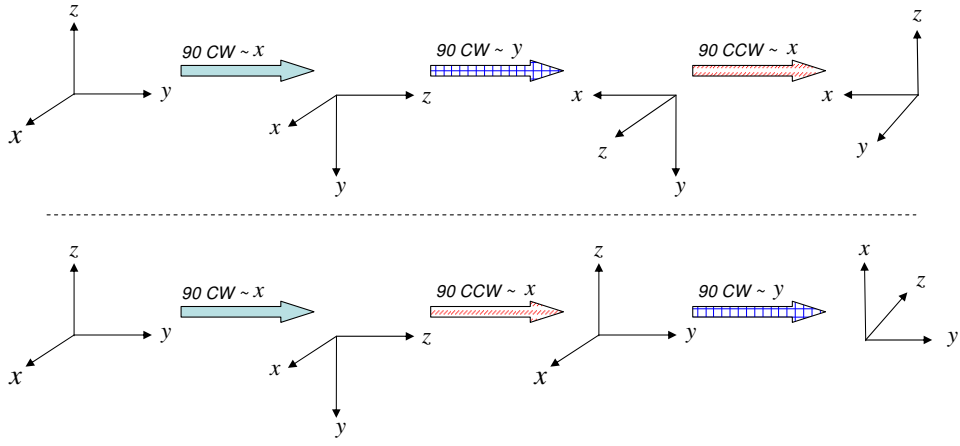
Figure 3.10: Rotation order impact. The axes undergo three rotations: a 90° CW rotation about the x-axis, a $90°$ CW rotation about the y-axis, and a $90°$ CCW rotation about the x-axis. The rotations are applied in different orders, resulting in different ending geometries.

sumption in this research is the rotated reference coordinate system does not remain fixed. In the maneuver model, six (6) unique rotation orders exist, each with their own unique rotation matrix: pitch-roll-yaw, pitch-yaw-roll, roll-pitch-yaw, roll-yaw-pitch, yaw-roll-pitch, and yaw-pitch-roll. It is also feasible to change rotation order during the coherent processing interval (CPI), i.e. perform a pitch-roll-yaw rotation on one pulse, then a yaw-pitch-roll rotation on the next. The focus of this research is characterization of *individual* platform maneuver effects. While the rotation framework constructed allows any combination of maneuver, each will be investigated separately.

A brief summary is in order. Rotation matrices for aircraft pitch, roll, and yaw were constructed using a relative reference frame (the platform). These rotation matrices produce the (x'_1, y'_1, z'_1) coordinates of the original (x_1, y_1, z_1) location. The overall goal remains characterization of the target and clutter environment. The (x'_1, y'_1, z'_1) coordinates are therefore transformed into their corresponding radar coordinates (θ'_1, ϕ'_1). Analogously to Equations (3.5) and (3.6), the elevation angle θ'_1 and azimuth

angle ϕ_1' to a target with coordinates (x_1',y_1',z_1') at range R_t are given by

$$\theta_1' = \sin^{-1}\left(\frac{z_1'}{R_t}\right),\tag{3.18}$$

and

$$\phi_1' = \cos^{-1}\left(\frac{y_1'}{R_t\cos\theta_1'}\right).\tag{3.19}$$

However, Equation (3.19)'s general definition of azimuth angle will not suffice in the platform maneuver model. Equation (3.19) is based on the geometry of Figure 3.2. It provides the angle from the axis on which y_1' exists, as depicted in Figure 3.11. This subtlety was a non-issue in the stationary model, since the azimuth angle to a target or clutter patch was constant and never required recalculation. A target was simply placed at an elevation and azimuth angle, while the ground plane was divided into $i \times k$ patches and the azimuth angles to the patches were N_c linearly spaced angles from 0-2π. The maneuver model azimuth angle is therefore first calculated using Equation (3.19), then modified appropriately depending on the quadrant the original (x_1,y_1,z_1) location resides in the rotated (x_1',y_1',z_1') space:

$$\phi_1' = \begin{cases} \phi_1' & x_1', y_1' \geq 0 \\ \pi - \phi_1' & x_1' > 0 \text{ and } y_1' < 0 \\ \phi_1' - \pi & x_1', y_1' \leq 0 \\ -\phi_1' & x_1' < 0 \text{ and } y_1' > 0 \end{cases}$$

Expressions for azimuth and elevation angle for pitch, roll, can now be derived. Recall (x_1',y_1',z_1') are functions of rotation type, rotation amount, and the original (x_1,y_1,z_1) coordinates. In the case of pitch, Equations (3.8 - 3.10) are substituted for (x_1,y_1,z_1) in Equations (3.18 - 3.19) producing,

$$\theta_p' = \sin^{-1}\left(\frac{-x\sin\psi_p + z\cos\psi_p}{R_t}\right),\tag{3.20}$$

45
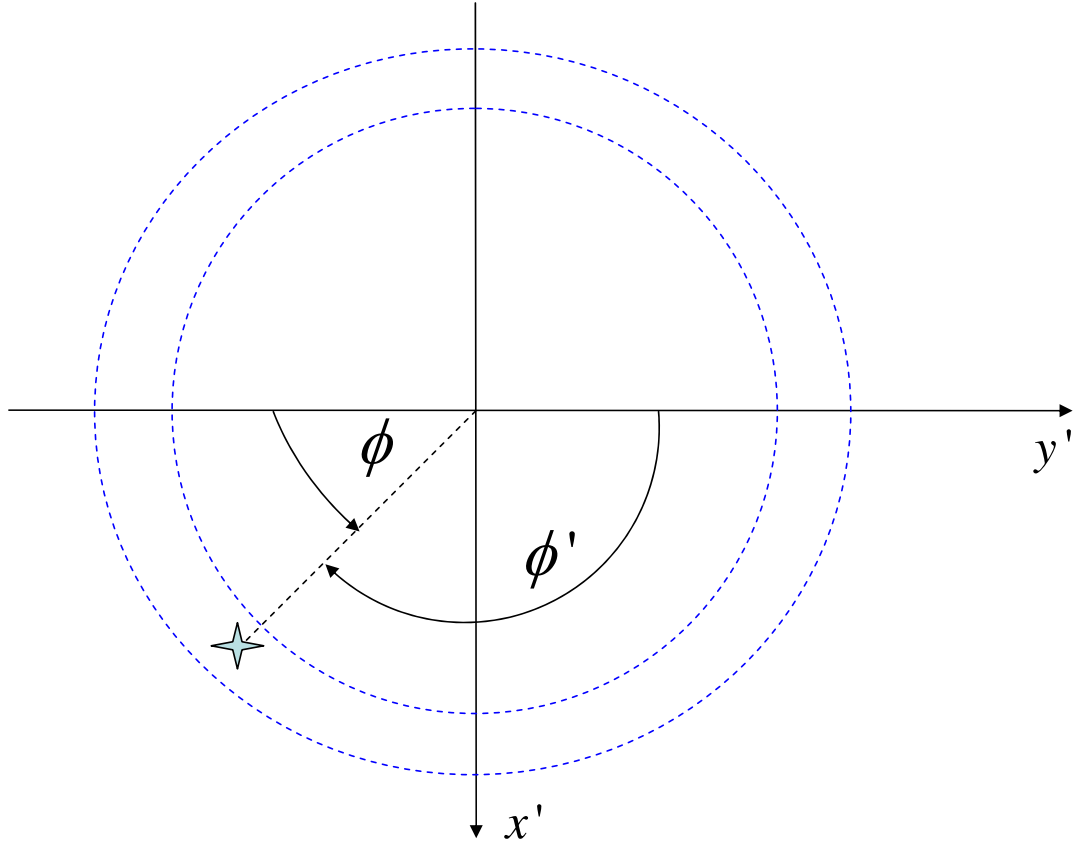
Figure 3.11: Azimuth angle calculation. The azimuth angle to the (x'_1, y'_1, z'_1) location depends on the quadrant it resides in the rotated coordinate system. Equation (3.19) calculates the angle from the y'-axis in the specific quadrant. The result must therefore be translated to the corresponding angle from boresight.

and

$$\phi'_p \;=\; \cos^{-1}\left(\frac{y}{R_t \cos \theta'_p}\right). \tag{3.21}$$

Substituting Equations (3.2 - 3.4) into (3.20 - 3.21) yields the elevation and azimuth angles to the original (x_1, y_1, z_1) given any amount of pitch ψ_p,

$$\theta'_p \;=\; \sin^{-1}\left(-\cos \theta \sin \phi \sin \psi_p + \sin \theta \cos \psi_p\right), \tag{3.22}$$

and

$$\phi'_p \;=\; \cos^{-1}\left(\frac{\cos\theta\cos\phi}{\cos\theta'_p}\right). \tag{3.23}$$

Pitch effect on azimuth and elevation angle is illustrated in Figure 3.12. An $(x,\,y,\,z)$ ground location was chosen in each quadrant. The degree of pitch was varied from 0°-360° corresponding to the platform making one full rotation about its x-axis. While unrealistic for the airborne radar platform, the full rotation allows insight into pitch effects on the angles to various locations. The results match physical intuition. Consider the ground location at boresight ($\phi = 0°$), labeled with a diamond ($\diamond$) in the plot. The location is originally located at $-3°$ elevation. Recall the definition of the elevation angle of Equation (3.18), stating the elevation angle is dependant on z'. As the platform begins to pitch up (CW), the z'-axis rotates CW, the z' coordinate of the ground location becomes less negative, and Equation (3.18) approaches zero. When the pitch rotation is $90°$, the ground location is at $z' = 0$ and the elevation angle to the original location is now $0°$. Continuing the rotation past $90°$ places the platform upsidedown, and the elevation angle to the original location becomes positive. At $180°$ pitch, the platform is completely inverted and the elevation angle to the location is $+3^o$. Similar basic exercises for the other locations plotted and azimuth angles show the results match physical intuition.

Next, roll effects on elevation and azimuth angles are found by substituting Equations (3.12 - 3.13) for (x_1,y_1,z_1) in Equations (3.18 - 3.19) producing,

$$\theta'_r \;=\; \sin^{-1}\left(-\cos\theta\cos\phi\sin\psi_r + \sin\theta\cos\psi_r\right), \tag{3.24}$$

and

$$\phi'_r \;=\; \cos^{-1}\left(\frac{\cos\theta\cos\phi\cos\psi_r + \sin\theta\sin\psi_r}{\cos\theta'_r}\right). \tag{3.25}$$

Roll effects on azimuth and elevation angle are illustrated in Figure 3.13. Once again

47
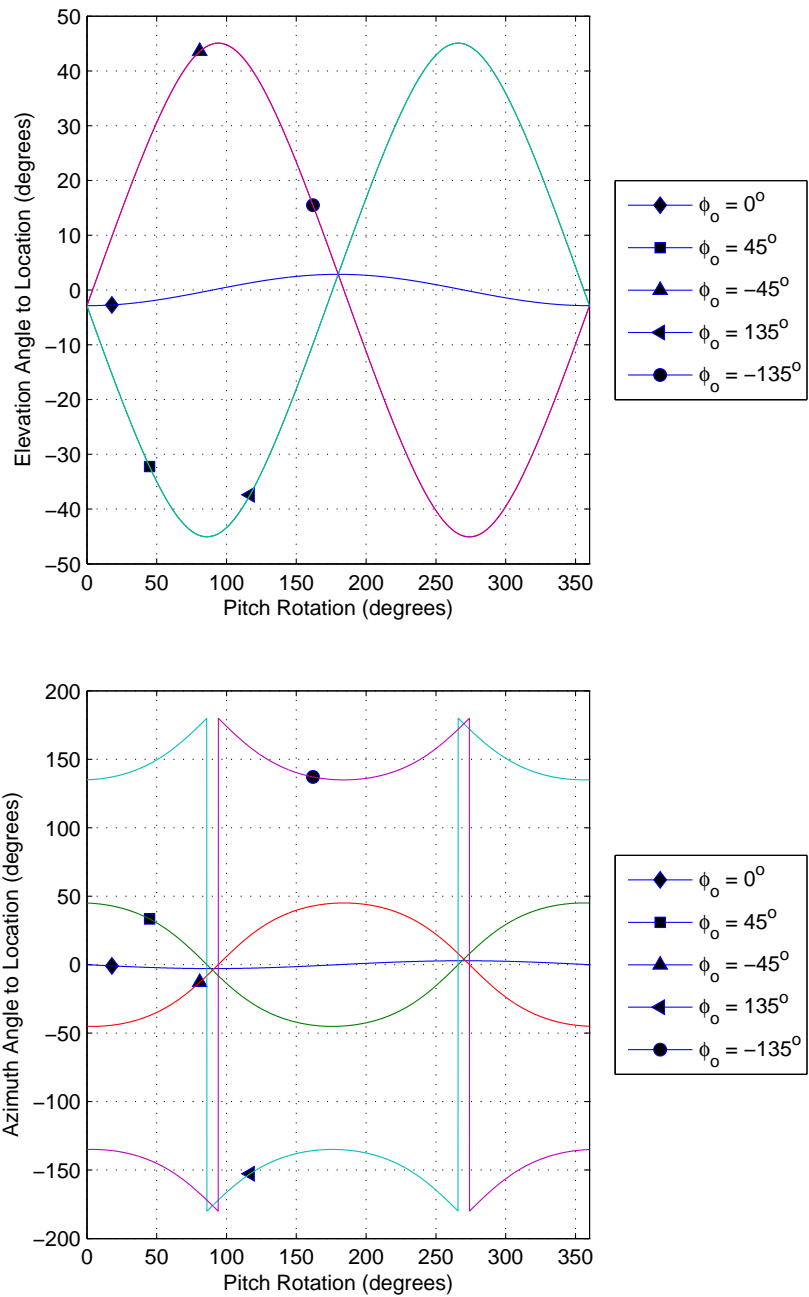
Figure 3.12: Pitch effect on azimuth and elevation angles. Five different azimuth locations on a single range ring are plotted. The top figure shows the pitch effect on elevation angle to various ground locations at a range of 60 km. The bottom figure shows the effect on azimuth angle to those same locations. The sharp jumps to/from $\pm 180°$ correspond to the location passing through radar the boresight (y') axis.
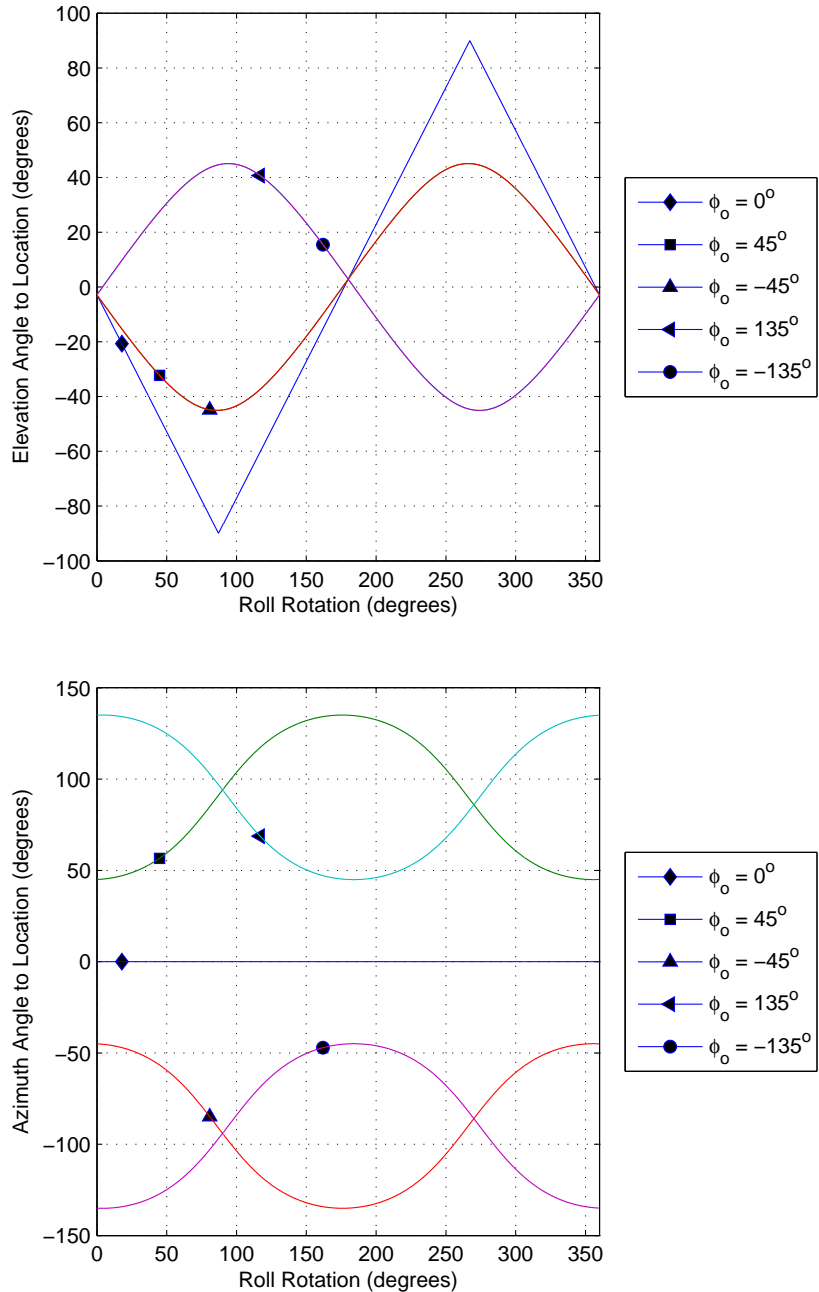
Figure 3.13: Roll effect on azimuth and elevation angles. Five different azimuth locations on a single range ring are plotted. The top figure shows the roll effect on elevation angle to various ground locations at a range of 60 km. The bottom figure shows the effect on azimuth angle to those same locations. The sharp jumps to/from ±90° correspond to the location passing to/from the front/back side on the array.

physical intuition and the results match. Consider the ground location at boresight ($\phi = 0$), labeled with a diamond ($\diamond$) in the plot. Elevation angle changes linearly with ψ_r for the location $\phi = 0$, and azimuth angle to $\phi = 0$ is constant despite the roll.

And finally, the elevation and azimuth angles for yaw are found by substituting Equations (3.15 - 3.16) for (x_1, y_1, z_1) in Equations (3.18 - 3.19) producing,

$$\theta'_y = \sin^{-1}(\sin\theta) = \theta, \tag{3.26}$$

and

$$\phi'_y = \cos^{-1}\left(\frac{\cos\theta\sin\phi\sin\psi_y + \cos\theta\cos\phi\cos\psi_y}{\cos\theta'_y}\right). \tag{3.27}$$

The result of Equation (3.26) states the elevation angle to any location is unchanged, despite any amount of platform yaw. The result makes physical sense since yaw corresponds to a rotation of the x-y plane. The elevation angle θ is measured from the x-y plane to the target, as depicted in Figure 3.2. The rotated x-y plane remains in the original plane for any values of yaw and more importantly the point from which θ is measured does not move. Therefore, the elevation angle remains unchanged. Substituting $\theta'_y = \theta$ into the expression for ϕ'_y (Equation 3.27) gives

$$\phi'_y = \cos^{-1}\left(\frac{\cos\theta\sin\phi\sin\psi_y + \cos\theta\cos\phi\cos\psi_y}{\cos\theta}\right). \tag{3.28}$$

The $\cos\theta$ terms cancel, and the compound angle identity

$$\sin A\sin B + \cos A\cos B = \cos(A - B), \tag{3.29}$$

produces

$$\phi'_y = \cos^{-1}\left(\cos(\phi - \psi_y)\right) \tag{3.30}$$

$$= \phi - \psi_y. \tag{3.31}$$

Equation (3.31) demonstrates the azimuth angle in the rotated coordinate system, ϕ'_y, is a linear function of the yaw amount ψ_y. Yaw effects are illustrated in Figure 3.14. The unchanging elevation angle and linearity of the azimuth angle are shown.

In this section, a mathematical framework enabling description of the radar angles to any location with any amount of pitch, roll, or yaw was constructed. With this mathematical framework in place, the logical progression is characterization of the platform rotation itself. Equations (3.22 - 3.27) were defined for a total degree of rotation, but the platform maneuvers continuously throughout the CPI. That movement must be discretized and the total degree of rotation at each discretization quantified in order to apply the framework developed in this section.

3.2   Rotation Behavior

The first step in describing the rotation behavior is defining the time space. The radar transmits an *uncompressed* pulse of width τ seconds then samples the environment at the center of each range cell, as depicted in Figure 3.15. The radar begins transmitting at time $t = 0$, ends transmitting at time $t = \tau$, then samples L range cells at τ intervals.

> ⚠ ! ⚠ For this development, the platform rotates continuously. The platform orientation on transmit is therefore different than the orientation on receive.

The process is repeated M times, once for each pulse in the CPI. The entire time span of the CPI is therefore $M(L+1)$ samples, beginning at the transmit time for the zeroth pulse $(\frac{\tau}{2})$ and ending at the sampling time for the Lth range cell on the $(M-1)^{th}$ pulse,

$$\mathbf{t} = \tau \left[\frac{1} {2} \ : \ 1 \ : \ (M(L+1)) \right]^{T} . \tag{3.32}$$

The transmit and receive times are subsets of the entire time span. The first time sample $\frac{\tau}{2}$ corresponds to the first transmitted pulse. The next pulse is transmitted $L+1$ samples later, after the radar has sampled the L range cells. The third pulse is transmitted $L+1$ samples after the second, or $2K+2$ after the first. The M transmit
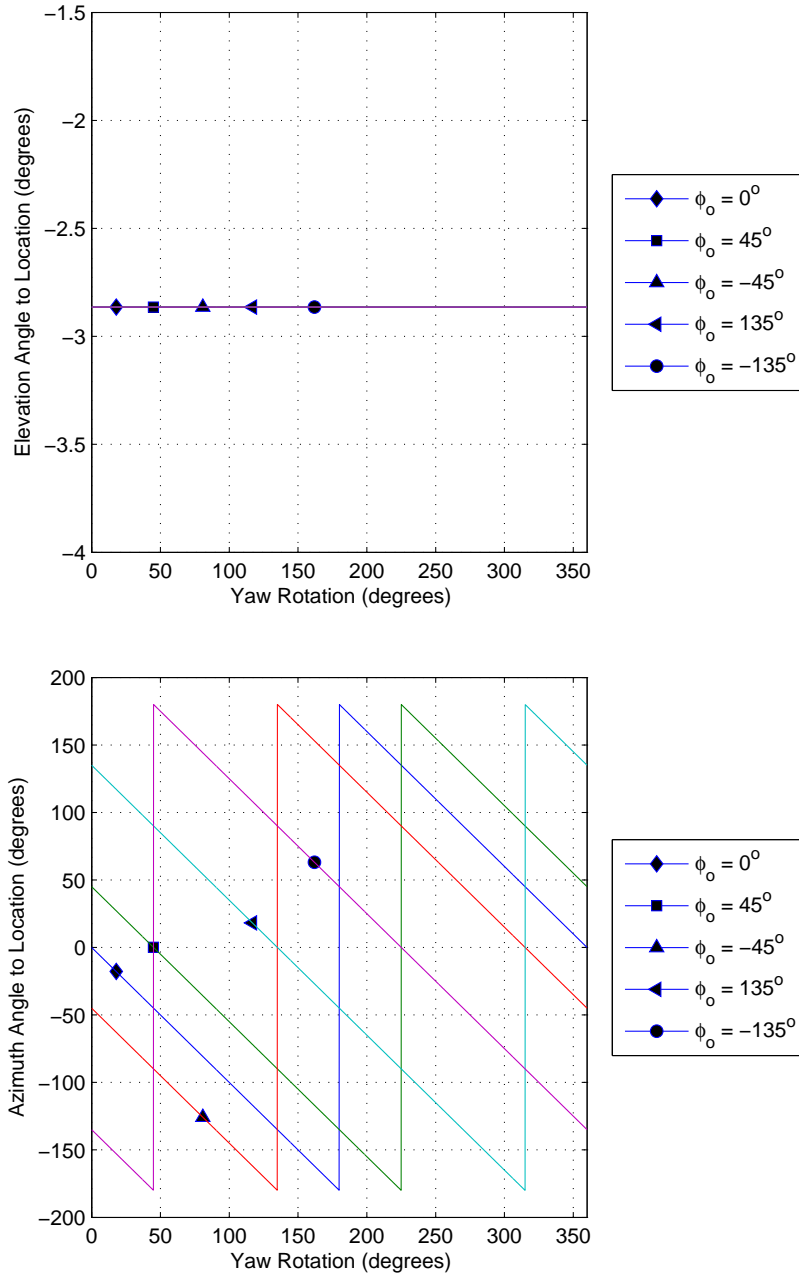
Figure 3.14: Yaw effect on azimuth and elevation angles. Five different azimuth locations on a single range ring are plotted. The top figure shows the yaw effect on elevation angle to various ground locations at a range of 60 km. As shown in Equation 3.26, yaw has no effect on elevation angle. The bottom figure shows the effect on azimuth angle to those same locations. As shown in Equation 3.31, the azimuth angle changes linearly with the amount of yaw. The sharp jumps at various locations correspond to each location passing through the radar boresight axis.
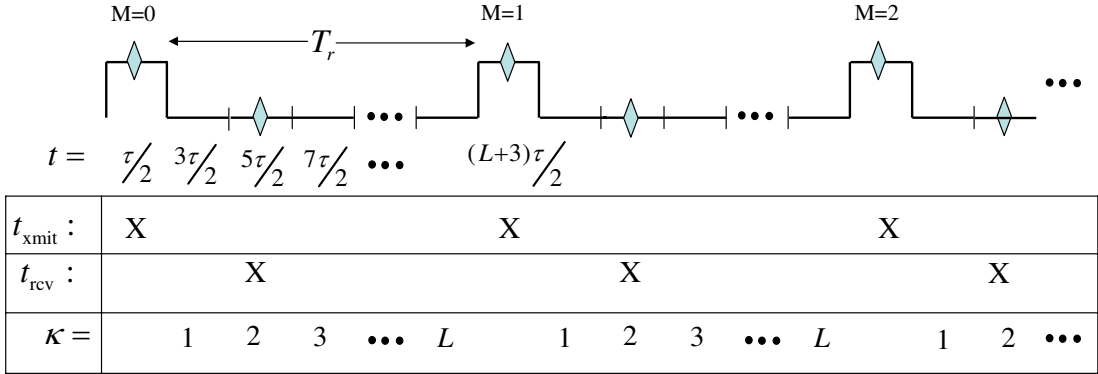
Figure 3.15: Maneuver model pulse train and time span. The CPI begins at $t = 0$ with the platform in its original position. Platform rotation begins immediately at $t = 0$. The platform rotation is discretized into τ intervals. Transmit times, noted with diamonds on the pulses, are designated t_{xmit} and the corresponding azimuth and elevation angle to the location (θ, ϕ) are designated $(\theta^{\text{tx}}, \phi^{\text{tx}})$. Receive times, noted with diamonds on range cells, are designated t_{rcv} and the corresponding azimuth and elevation angle to the location (θ, ϕ) are designated $(\theta^{\text{rv}}, \phi^{\text{rv}})$. There are M values for each of these quantities, corresponding to the M pulses in the CPI. Range cells, κ, are numbered 1 to L.

times are therefore the subset of the entire time span given by,

$$\mathbf{t}_{\text{xmit}} = \mathbf{t}(1 : L + 1 : M(L + 1)) \tag{3.33}$$

The receive times depend on the range cell under test (RUT). A CPI contains M different returns sampled at M different times corresponding to the same range R_t. The total number of range cells is defined as

$$L = \left\lfloor \frac{T_r}{\tau} \right\rfloor, \tag{3.34}$$

where $\lfloor \ \rfloor$ represents the flooring function. The range bin of interest, κ, corresponding to the time sample at range R_t is

$$\kappa = \frac{R_t L}{R_u}, \tag{3.35}$$

53

where R_u is the radar's unambiguous range,

$$R_u = \frac{cT_p}{2}. \tag{3.36}$$

The first receive time corresponds to the $\kappa + 1$ sample, as depicted in Figure 3.15. The next receive time is $L + 1$ samples later. And the third receive time is $L + 1$ samples after the second, or $2L + 2$ after the first. The M receive times are therefore a subset of the entire time span given by

$$\mathbf{t}_{\mathrm{rcv}} = \mathbf{t}(\kappa + 1 : L + 1 : M(L + 1)). \tag{3.37}$$

Given complete characterization of the CPI time span, the platform orientation at each transmit and receive time must be defined. Pitch, roll, and yaw rates (degrees per second) are defined as ρ_p, ρ_r, and ρ_y respectively. These rotations rates are assumed constant throughout the CPI.

> **!** As previously mentioned, the focus of this research is the effect of individual rotations. While the development of each rotation to follow will mirror one another, only one rotation type will be implemented at a time. Equations (3.38 - 3.40) yield M linear rotation angles based on the constant rotation rates. If modeling combinations of maneuver effects were of interest, a deviation from the constant rotation rate could be employed, i.e. platform rolls right for several time samples, then yaws up, then rolls left. The constant rotation rate limits the modeling capability to linear combinations (pitch-roll-yaw, pitch-yaw-roll, roll-pitch-yaw, roll-yaw-pitch, yaw-pitch-roll, or yaw-roll-pitch) of a set number of degrees each time sample.

At any given time the total degree of rotation is the product of rotation rate and time. The total degree of rotation at each instance of transmit are therefore the rotation rates times the transmit times,

$$\boldsymbol{\psi}_p^{\mathrm{tx}} = \rho_p \mathbf{t}_{\mathrm{xmit}}, \tag{3.38}$$

$$\boldsymbol{\psi}_r^{\mathrm{tx}} = \rho_r \mathbf{t}_{\mathrm{xmit}}, \tag{3.39}$$

and

$$\boldsymbol{\psi}_y^{\text{tx}} = \rho_y \mathbf{t}_{\text{xmit}}. \tag{3.40}$$

And the total degree of rotation at each instance of receive are the rotation rates time the receive times,

$$\boldsymbol{\psi}_p^{\text{rv}} = \rho_p \mathbf{t}_{rcv}(R_t), \tag{3.41}$$

$$\boldsymbol{\psi}_r^{\text{rv}} = \rho_r \mathbf{t}_{rcv}(R_t), \tag{3.42}$$

and

$$\boldsymbol{\psi}_y^{\text{rv}} = \rho_y \mathbf{t}_{rcv}(R_t). \tag{3.43}$$

> ! All angles corresponding to array orientation upon transmit are designated with superscript tx. All angles corresponding to array orientation upon receive are designated with superscript rv. The subscript indicates the type of rotation.

The M elevation angles to the location (θ,ϕ) on transmit are therefore the rotation amounts (Equations (3.38-3.40)) evaluated by the expressions for elevation angle (Equations (3.22-3.26)):

$$\boldsymbol{\theta}_p^{\text{tx}} = \sin^{-1}\left(-\cos\theta\sin\phi\sin\boldsymbol{\psi}_p^{\text{tx}} + \sin\theta\cos\boldsymbol{\psi}_p^{\text{tx}}\right), \tag{3.44}$$

$$\boldsymbol{\theta}_r^{\text{tx}} = \sin^{-1}\left(-\cos\theta\cos\phi\sin\boldsymbol{\psi}_r^{\text{tx}} + \sin\theta\cos\boldsymbol{\psi}_r^{\text{tx}}\right), \tag{3.45}$$

or

$$\boldsymbol{\theta}_y^{\text{tx}} = \theta\mathbf{1}_M, \tag{3.46}$$

depending on the rotation being modeled. The $\mathbf{1}_M$ represents a $M \times 1$ vector of ones, and therefore $\theta \odot \mathbf{1}_M$ is a $M \times 1$ vector with M values of the original θ (yaw does not affect elevation angle).

$\boxed{!}$ A element by element division operator must be introduced to proceed. For this research, element by element division is represented with the $\odot$ in the denominator of an expression. The $\odot$ precedes the vector quantity that performs the element by element division.

The M azimuth angles to location (θ,ϕ) on transmit are:

$$\boldsymbol{\phi}_p^{\text{tx}} = \cos^{-1}\left(\frac{\cos\theta\cos\phi}{\odot\cos\boldsymbol{\theta}_p^{\text{tx}}}\right), \tag{3.47}$$

$$\boldsymbol{\phi}_r^{\text{tx}} = \cos^{-1}\left(\frac{\cos\theta\cos\phi\cos\boldsymbol{\psi}_r^{\text{tx}}+\sin\theta\sin\boldsymbol{\psi}_r^{\text{tx}}}{\odot\cos\boldsymbol{\theta}_r^{\text{tx}}}\right), \tag{3.48}$$

or

$$\boldsymbol{\phi}_y^{\text{tx}} = \cos^{-1}\left(\frac{\cos\theta\sin\phi\cos\boldsymbol{\psi}_y^{\text{tx}}+\cos\theta\cos\phi\cos\boldsymbol{\psi}_y^{\text{tx}}}{\odot\cos\boldsymbol{\theta}_y^{\text{tx}}}\right), \tag{3.49}$$

depending on the rotation being modeled. And the M elevation and azimuth angles on receive are:

$$\boldsymbol{\theta}_p^{\text{rv}} = \sin^{-1}\left(-\cos\theta\sin\phi\sin\boldsymbol{\psi}_p^{\text{rv}}+\sin\theta\cos\boldsymbol{\psi}_p^{\text{rv}}\right), \tag{3.50}$$

$$\boldsymbol{\theta}_r^{\text{rv}} = \sin^{-1}\left(-\cos\theta\cos\phi\sin\boldsymbol{\psi}_r^{\text{rv}}+\sin\theta\cos\boldsymbol{\psi}_r^{\text{rv}}\right), \tag{3.51}$$

or

$$\boldsymbol{\theta}_y^{\text{rv}} = \theta\mathbf{1}_M, \tag{3.52}$$

and

$$\boldsymbol{\phi}_p^{\text{rv}} = \cos^{-1}\left(\frac{\cos\theta\cos\phi}{\odot\cos\boldsymbol{\theta}_p^{\text{rv}}}\right), \tag{3.53}$$

56

$$\phi_r^{\text{rv}} = \cos^{-1}\left(\frac{\cos\theta\cos\phi\cos\psi_r^{\text{rv}} + \sin\theta\sin\psi_r^{\text{rv}}}{\boxdot\cos\theta_r^{\text{rv}}}\right), \tag{3.54}$$

or

$$\phi_y^{\text{rv}} = \cos^{-1}\left(\frac{\cos\theta\sin\phi\cos\psi_y^{\text{rv}} + \cos\theta\cos\phi\cos\psi_y^{\text{rv}}}{\boxdot\cos\theta_y^{\text{rv}}}\right), \tag{3.55}$$

depending on the rotation being modeled.

The mathematical framework characterizing aircraft pitch, roll, or yaw in either CW or CCW directions was established in Section 3.1. The rotation behavior was characterized in this section. The net result is locations (targets and clutter patches) previously defined by a single (θ,ϕ) pair now are defined by M $(\boldsymbol{\theta}^{\text{tx}}, \boldsymbol{\phi}^{\text{tx}})$ pairs on transmit and M $(\boldsymbol{\theta}^{\text{rv}}, \boldsymbol{\phi}^{\text{rv}})$ pairs on receive. The objective remains accurate characterization of the target and the clutter environment. The stationary model framework discussed in Chapter II serves as the foundation for that characterization, but requires modification. Components of the stationary model requiring modification include the signal model, formatting, target model, and clutter model.

3.3   *Platform Maneuver Signal Model*

While the orientation of the platform on transmit changes on a pulse to pulse basis, the transmit signal itself is unchanged and remains [3],

$$s(t) = a_t u(t)e^{j(\omega_o t + \varphi)}. \tag{3.56}$$

However, modification of the receive signal model is required. Quantities that were time independent in the stationary model now have time dependencies. Derivation of the platform maneuver receive signal model begins with the original *stationary* model receive waveform defined by [3]

$$s_{np}(t) = a_r u(t - \tau_{np})e^{j2\pi f_o(t - \tau_{np})}e^{j2\pi f_d(t - \tau_{np})}e^{j\varphi}, \tag{3.57}$$

where the time delay τ_{np} is the sum of the round trip time from the array face to the target, T_R, and the differential time τ'_{np} from the reference element to each individual np^{th} element [3],

$$\tau_{np} = T_R + \tau'_{np}. \tag{3.58}$$

The narrowband assumption,

$$\tau \gg \frac{\sqrt{(Nd_x)^2 + (Pd_z)^2}}{c}, \tag{3.59}$$

remains and is unaffected by platform maneuver. The physical dimensions of the array and time duration of the signal have not changed. Each element receives the signal at the same time under the assumption, and the signal is rewritten as

$$s_{np}(t) \quad = \quad a_r u(t - T_R) e^{j2\pi f_o(t - T_R - \tau'_{np})} e^{j2\pi f_d(t - T_R - \tau'_{np})} e^{j\varphi}, \tag{3.60}$$

Platform maneuver equates to time-varying array orientation and velocity vector. Therefore, the differential time delay τ'_{np} and Doppler frequency f_d now have time dependencies. Additionally, the receive amplitude is no longer assumed constant for the CPI. The environment is illuminated differently as the platform rotates and the receive amplitude therefore requires a time dependence as well. The total time delay becomes

$$\tilde{\tau}_{np}(t) = T_R + \tilde{\tau}'_{np}(t). \tag{3.61}$$

And the differential time delay with time dependance is given by,

$$\tilde{\tau}'_{np} \quad = \quad \frac{\hat{\mathbf{k}}(\theta^{\mathrm{rv}}(t), \phi^{\mathrm{rv}}(t) \cdot \hat{\mathbf{d}}_{np}(t)}{c}, \tag{3.62}$$

$$= \quad \frac{-nd_x \cos\theta^{\mathrm{rv}}(t)\sin\phi^{\mathrm{rv}}(t) - pd_z \sin\theta^{\mathrm{rv}}(t)}{c}, \tag{3.63}$$

where the radar angles and platform orientation are both now time dependant. The time-variant spatial frequencies, describing the phase behavior of the return signal

across element, are given by

$$\tilde{\vartheta}_x(t) = \frac{d_x \cos \theta^{\text{rv}}(t) \sin \phi^{\text{rv}}(t)}{\lambda_o} \tag{3.64}$$

and

$$\tilde{\vartheta}_z(t) = \frac{d_z \sin \phi^{\text{rv}}(t)}{\lambda_o}. \tag{3.65}$$

Incorporating these time dependencies into the signal model yields

$$\tilde{s}_{np}(t) = a_r(t)u(t - T_R)e^{j2\pi(f_o + f_d(t))t}e^{-j2\pi(f_o + f_d(t))T_R}e^{jf_d(t)\tau'_{np}(t)}e^{j2\pi(n\tilde{\vartheta}_x(t) + p\tilde{\vartheta}_z(t))}e^{j\varphi} \tag{3.66}$$

The $e^{-j2\pi f_o T_R}$ phase terms is not a function of time and therefore rolled into the random phase term $e^{j\varphi}$,

$$\tilde{s}_{np}(t) = a_r(t)u(t - T_R)e^{j2\pi(f_o + f_d(t))t}e^{-j2\pi f_d(t)T_R}e^{jf_d(t)\tau'_{np}(t)}e^{j2\pi(n\tilde{\vartheta}_x(t) + p\tilde{\vartheta}_z(t))}e^{j\varphi}. \tag{3.67}$$

Referring to Equation 3.63, $f_d(t)\tau'_{np}(t) \approx 0$ because the element spacing is on the order of several meters while the propagation speed is the speed of light (on the order of 10^8 meters). Expected Doppler frequencies are not large enough to make the $f_d\tau'_{np}(t) \approx 0$ approximation invalid. This reduction is not performed on the $f_o\tau'_{np}(t)$ term because the transmit frequency f_o can be on the same order of magnitude as c. Approximating $e^{jf_d(t)\tau'_{np}(t)}$ as $e^0 = 1$ leaves the return signal given by

$$\tilde{s}_{np}(t) = a_r(t)u(t - T_R)e^{j2\pi(f_o + f_d(t))t}e^{-j2\pi f_d(t)T_R}e^{j2\pi(n\tilde{\vartheta}_x(t) + p\tilde{\vartheta}_z(t))}e^{j\varphi}. \tag{3.68}$$

Each element, with its own receiver chain depicted in Figure 2.3, strips the carrier frequency f_o to an intermediate frequency assumed baseband:

$$\tilde{s}_{np}(t) = a_r(t)u(t - T_R)e^{j2\pi f_d(t)t}e^{-j2\pi f_d(t)T_R}e^{j2\pi(n\tilde{\vartheta}_x(t) + p\tilde{\vartheta}_z(t))}e^{j\varphi}. \tag{3.69}$$

Platform maneuver has no effect on the Doppler tolerance condition of [5]

$$v_r \leq \frac{cB}{2f_o}. \tag{3.70}$$

The time-frequency autocorrelation function is therefore assumed unity and the match filtered signal is given by

$$\tilde{x}_{np}(t) = a_r(t)e^{j2\pi(n\vartheta_x(t)+p\vartheta_z(t))}e^{j2\pi f_d(t)T_R}e^{j\varphi}. \tag{3.71}$$

The radar samples the environment at the RUT M times during the CPI. The round trip delay time for the mth pulse is given by $T_R + mT_r$. The match filtered signal at pulse m is therefore

$$\tilde{x}_{mnp} = a_r(m)e^{j\varphi}e^{j2\pi(n\vartheta_x(m)+p\vartheta_z(m))}\sum_{i=0}^{M-1}e^{j2\pi f_d(i)(T_R+iT_r)}. \tag{3.72}$$

The T_R term can be extracted from the summation and rolled into the random phase $e^{j\varphi}$. And the term $f_d \times T_r$ is the definition of normalized Doppler frequency $\bar{\omega}$. The final match filtered signal for pulse m is given by

$$\tilde{x}_{mnp} = a_t(m)e^{j2\pi(n\vartheta_x(m)+p\vartheta_z(m))}\sum_{i=0}^{m}e^{j2\pi\bar{\omega}(i)}, \tag{3.73}$$

where a_r and $e^{j\varphi}$ were rolled into the complex amplitude $\alpha_t(m)$.

Reduction to the stationary model waveform is achieved when $\vartheta_x(m) = \vartheta_x$, $\vartheta_z(m) = \vartheta_z$, $\bar{\omega}(i) = \bar{\omega}$, and $\alpha_t(m) = \alpha_t$.

Several differences are apparent when comparing the maneuver and stationary signal models. The spatial frequencies now depend on the platform orientation at pulse m. The phase due to Doppler is no longer a linear function of a single $\bar{\omega}$, as the Doppler from each pulse depends on platform orientation at that pulse. The return amplitude is no longer constant throughout the CPI. The environment is illuminated differently each pulse as the platform maneuvers. In order to accurately characterize

60

the target and clutter, space-time snapshots must be created. However, these signal model differences created by platform maneuver necessitate a modification of the stationary model framework. The time dependencies of spatial and Doppler frequencies, as well as amplitude, does not "fit" into the previous framework. The next section creates a new framework to create accurate space-time snapshots and model the target and interference environment.

3.4   Formatting

The discussion to follow describes maneuver steering vector and maneuver space-time snapshot construction to a single location originally at (θ, ϕ) in the stationary platform scenario. The format developed here is then applied to the modified target (Section 3.5) and clutter (Section 3.6) models. A target or clutter patch was previously located at one θ and one ϕ during a single CPI. That single (θ, ϕ) translated to single valued spatial frequencies, $\hat{\mathbf{k}}$ unit vector to (θ, ϕ), relative velocity, Doppler frequency, platform orientation, antenna pattern to (θ, ϕ), and return amplitude. The spatial steering vectors were $N \times 1$ and $P \times 1$ column vectors, while the temporal steering vector was $M \times 1$. The $MNP \times 1$ steering vector to (θ, ϕ) was created with the Kronecker product $(\otimes)$,

$$\mathbf{v}_t(\theta, \phi) = \mathbf{e}(\vartheta_z) \otimes \mathbf{b}(\bar{\omega}) \otimes \mathbf{a}(\vartheta_x). \tag{3.74}$$

And the complete space-time snapshot was

$$\boldsymbol{\chi}_t(\theta, \phi) = \alpha_t \mathbf{v}_t. \tag{3.75}$$

Incorporating platform maneuver creates M different values of the aforementioned quantities for each (θ, ϕ) location, necessitating modification of the Chapter II steering vector framework. Capturing the $MNP \times 1$ space-time snapshot describing the per pulse per element signal return remains the goal, but a new steering vector and amplitude framework is required. The steering vectors will no longer be separable as

61
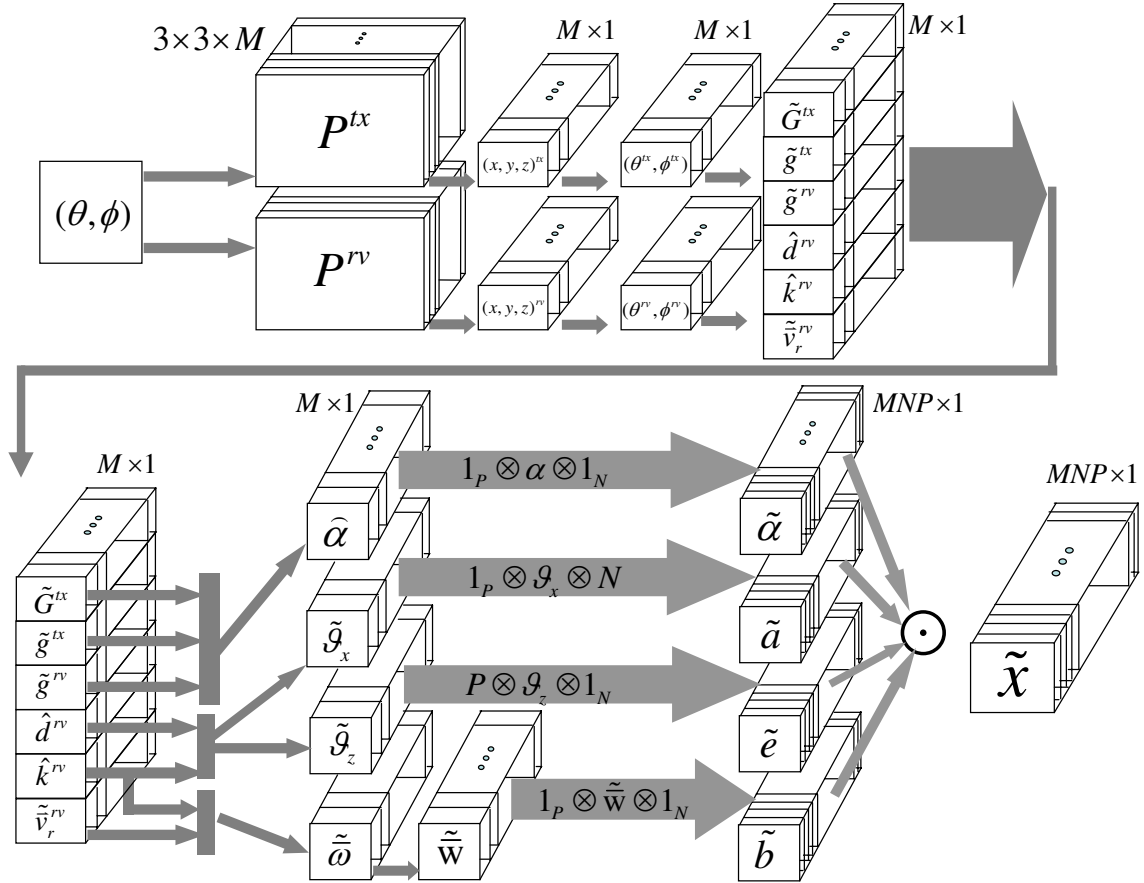
Figure 3.16:   Maneuver model formatting block diagram. The following depiction applies to a single location located at (θ,ϕ) in the original coordinate system. The location is transformed into M transmit and M receive coordinates using the rotation matrices developed in Section 3.1. The M pairs are then transformed into radar coordinates. The M transmit and M receive angles to location (θ,ϕ) translate to M different array gains, element gains, element location unit vectors, unit vectors to (θ,ϕ), and aircraft velocity vectors. $M \times 1$ amplitudes, spatial steering vectors, and temporal steering vectors result. These are then recast into $MNP \times 1$ spatial-temporal steering vectors. The snapshot is given by the Hadamard product of the four $MNP \times 1$ vectors.

spatial and temporal in the strictest sense, because each will contain spatial and temporal phase information. Figure 3.16 offers a visualization of the formatting approach for the platform maneuver model.

Section 3.1 derived the rotation matrices for pitch, yaw, and roll. Section 3.2 described the discretized platform maneuver, resulting in differing platform orientations

on transmit and receive for each pulse. The first maneuver model formatting step is applying two (one for transmit and one for receive) $3 \times 3 \times M$ rotation matrices, $\mathbf{P}^{\text{tx}}$ and $\mathbf{P}^{\text{rv}}$, to the original (x,y,z) coordinates of the (θ,ϕ) location as depicted in Figure 3.16. $\mathbf{P}^{\text{tx}}$ and $\mathbf{P}^{\text{rv}}$ are filled with rotation values based on the constant rate of rotation throughout the CPI as defined in Section 3.2. Equations (3.18-3.19) transform the resulting M $(x^{\text{tx}},y^{\text{tx}},z^{\text{tx}})$ and $(x^{\text{rv}},y^{\text{rv}},z^{\text{rv}})$ values into M radar coordinate values $(\theta^{\text{tx}},\phi^{\text{tx}})$ and $(\theta^{\text{rv}},\phi^{\text{rv}})$. The M radar coordinate values to (θ,ϕ) are cast into $M \times 1$ column vectors $\boldsymbol{\theta}^{\text{tx}},\boldsymbol{\phi}^{\text{tx}},\boldsymbol{\theta}^{\text{rv}}$, and $\boldsymbol{\phi}^{\text{rv}}$.

Recall the $\hat{\mathbf{k}}$ unit vector describes the direction to the (θ, ϕ) location referenced from the array orientation *in the rotated frame*. A different target unit vector therefore exists for each platform orientation. The platform orientations on receive provide the needed phase information and Doppler information of the return signal. The $M \times 1$ column vector of unit vectors to (θ, ϕ) on receive are designated $\hat{\mathbf{k}}^{\text{rv}}$ and given by

$$\hat{\mathbf{k}}^{\text{rv}} = [\cos\boldsymbol{\theta}^{\text{rv}} \odot \sin\boldsymbol{\phi}^{\text{rv}}]\hat{\mathbf{x}}^{\text{rv}} + [\cos\boldsymbol{\theta}^{\text{rv}} \odot \cos\boldsymbol{\phi}^{\text{rv}}]\hat{\mathbf{y}}^{\text{rv}} + [\sin\boldsymbol{\theta}^{\text{rv}}]\hat{\mathbf{z}}^{\text{rv}} \qquad (3.76)$$

The array reference element defines the reference frame origin at any orientation, and the element locations therefore remain in the x-z reference plane. There are now M x-z reference planes, corresponding to M platform orientations on receive. The M unit vectors from the reference element to the np^{th} element are thus given by

$$\hat{\mathbf{d}}_{np}^{\text{rv}} = -nd_x\hat{\mathbf{x}}^{\text{rv}} - pd_z\hat{\mathbf{z}}^{\text{rv}}. \qquad (3.77)$$

The newly defined $\boldsymbol{\theta}^{\text{tx}},\boldsymbol{\phi}^{\text{tx}}, \boldsymbol{\theta}^{\text{rv}}, \boldsymbol{\phi}^{\text{rv}},\hat{\mathbf{k}}^{\text{rv}}$, and $\hat{\mathbf{d}}_{np}^{\text{rv}}$, and resulting dimensionality drive the creation of $MNP \times 1$ spatial-temporal steering vectors.

3.4.1 Spatial-Temporal Steering Vectors with Motion. The differential time delay, τ_{np}', describes the return signal time difference of arrival between elements. That time difference of arrival depends on the platform orientation and the general

definition is given by [3]

$$\tau'_{np} = \frac{\hat{\mathbf{k}} \cdot \hat{\mathbf{d}}_{np}}{c}, \tag{3.78}$$

for the stationary model. There are now M target unit vectors and M platform orientations, thereby creating M differential time delays

$$\boldsymbol{\tau}'_{np} = \frac{\hat{\mathbf{k}}^{\mathrm{rv}}(\boldsymbol{\theta}^{\mathrm{rv}}, \boldsymbol{\phi}^{\mathrm{rv}}) \cdot \hat{\mathbf{d}}^{\mathrm{rv}}_{np}}{c}, \tag{3.79}$$

$$= \frac{-n d_x \cos \boldsymbol{\theta}^{\mathrm{rv}} \odot \sin \boldsymbol{\phi}^{\mathrm{rv}} - p d_z \sin \boldsymbol{\theta}^{\mathrm{rv}}}{c}, \tag{3.80}$$

Analogously to the stationary model development, spatial frequencies are defined from the differential time delay $\boldsymbol{\tau}'_{np}$ as

$$\tilde{\boldsymbol{\vartheta}}^{\mathrm{rv}}_x = \frac{d_x \cos \boldsymbol{\theta}^{\mathrm{rv}} \odot \sin \boldsymbol{\phi}^{\mathrm{rv}}}{c} \tag{3.81}$$

and

$$\tilde{\boldsymbol{\vartheta}}^{\mathrm{rv}}_z = \frac{d_z \sin \boldsymbol{\theta}^{\mathrm{rv}}}{c}. \tag{3.82}$$

Physically, Equation (3.81) describes the x^{rv}-axis phase behavior for each platform orientation while Equation (3.82) describes the z^{rv}-axis phase behavior for each platform orientation. The *stationary* model azimuth and elevation steering vectors are given by the $N \times 1$ and $P \times 1$ vectors [3]

$$\mathbf{a}(\vartheta_x) = e^{j 2 \pi \vartheta_x (0:N-1)^T}, \tag{3.83}$$

and

$$\mathbf{e}(\vartheta_z) = e^{j 2 \pi \vartheta_z (0:P-1)^T}. \tag{3.84}$$

Similar steering vectors can accurately model phase across elements in the maneuver model, but only for a single platform orientation:

$$\dot{\mathbf{a}}(\boldsymbol{\vartheta}_x^{\mathrm{rv}}|_m) = e^{j2\pi\boldsymbol{\vartheta}_x^{\mathrm{rv}}|_m(0:N-1)^T}.\tag{3.85}$$

and

$$\dot{\mathbf{e}}(\boldsymbol{\vartheta}_z^{\mathrm{rv}}|_m) = e^{j2\pi\boldsymbol{\vartheta}_z^{\mathrm{rv}}|_m(0:P-1)^T}.\tag{3.86}$$

The formatting difficulty arises because there are now M unique azimuth steering vectors like $\dot{\mathbf{a}}$ and M unique elevation steering vectors like $\dot{\mathbf{e}}$ needed to model phase across elements. The $\mathbf{e}\otimes\mathbf{b}\otimes\mathbf{a}$ steering vector paradigm is therefore abandoned. Instead, the M spatial frequencies describing the x^{rv} and z^{rv}-axis phase behavior are recast into $MNP\times 1$ spatial-temporal steering vectors. These $MNP\times 1$ spatial-temporal steering vectors contain the phase contribution due to physical element separation for each element and pulse. The per element per pulse phase contribution due to horizontal element is created by,

$$\tilde{\mathbf{a}}(\boldsymbol{\vartheta}_x^{\mathrm{rv}}) = e^{j2\pi\mathbf{1}_p\otimes\boldsymbol{\vartheta}_x^{\mathrm{rv}}\otimes\mathbf{N}},\tag{3.87}$$

where $N = [0:N-1]^T$ and $\mathbf{1}_{\mathrm{P}}$ is a $P\times 1$ vector of ones. And the per element per pulse phase contribution due to vertical element separation is created by

$$\tilde{\mathbf{e}}(\boldsymbol{\vartheta}_z^{\mathrm{rv}})e^{j2\pi\mathbf{P}\otimes\boldsymbol{\vartheta}_z^{\mathrm{rv}}\otimes\mathbf{1}_{\mathbf{N}}},\tag{3.88}$$

where $P = [0:P-1]^T$ and $\mathbf{1}_{\mathrm{N}}$ is a $N\times 1$ vector of ones. The total spatial-temporal phase due to element separation is simply $\tilde{\mathbf{e}}\odot\tilde{\mathbf{a}}$. The final component needed to capture the total spatial-temporal phase of the return signal is the Doppler phase contribution.

3.4.2 Temporal-Spatial Steering Vector with Motion. The temporal phase delay depends on the pulse to pulse Doppler frequency of the returns, just as it did

in the stationary model. The normalized Doppler frequency $\bar{\omega}$ is defined [9],

$$\bar{\omega} = \frac{2v_r}{\lambda f_r}, \tag{3.89}$$

where v_r is the relative velocity between the aircraft and target, λ is the radar transmit wavelength, and f_r is the PRF. The relative velocity between two objects is the time rate of change of the distance between them,

$$v_r = \frac{dR}{dt}. \tag{3.90}$$

This time rate of change is the projection of the aircraft velocity vector $\vec{\mathbf{v}}_a$ onto the unit vector to the target, $\hat{\mathbf{k}}$, plus the projection of the target velocity vector $\vec{\mathbf{v}}_t$ onto $\hat{\mathbf{k}}$. There are now M unit vectors to the target and M aircraft velocity vectors due to platform maneuver, resulting in M different relative velocities

$$\mathbf{v}_r = \hat{\mathbf{k}}^{\mathrm{rv}} \cdot \vec{\mathbf{v}}_a^{\mathrm{rv}} + \hat{\mathbf{k}}^{\mathrm{rv}} \cdot \vec{\mathbf{v}}_t^{\mathrm{rv}} \tag{3.91}$$

and M different Doppler frequencies

$$\bar{\boldsymbol{\omega}}^{\mathrm{rv}} = 2 \frac{\hat{\mathbf{k}}^{\mathrm{rv}} \cdot \vec{\mathbf{v}}_a^{\mathrm{rv}} + \hat{\mathbf{k}}^{\mathrm{rv}} \cdot \vec{\mathbf{v}}_t^{\mathrm{rv}}}{\lambda f_p} \tag{3.92}$$

In the stationary model, the relative velocity between a location (be it a target or clutter) remained constant throughout the CPI. The Doppler frequency, $\bar{\omega}$, was constant and the resulting pulse to pulse phase due to Doppler was a linear function of a single Doppler frequency:

$$\mathbf{b}(\bar{\omega}) = [e^{j2\pi\bar{\omega}(0:M-1)}]^T. \tag{3.93}$$

In the maneuver model, the M different relative velocities lead to M different Doppler frequencies and the pulse to pulse phase change due to Doppler is no longer a linear function of a single normalized doppler value. The M Doppler frequency values given

66

by Equation (3.92) correspond to individual Doppler frequencies,

$$\bar{\boldsymbol{\omega}} = [\bar{\omega}^{\mathrm{rv}}(0) \quad \bar{\omega}^{\mathrm{rv}}(1) \quad \ldots \quad \bar{\omega}^{\mathrm{rv}}(M-1)]^T. \tag{3.94}$$

The corresponding pulse to pulse phase progression due to these individual Doppler frequencies is sought. Capturing that phase progression requires the M individual Doppler values recast in the form,

$$\bar{\mathbf{w}} = [\bar{\omega}^{\mathrm{rv}}(0) \quad [\bar{\omega}^{\mathrm{rv}}(0) + \bar{\omega}^{\mathrm{rv}}(1)] \quad \ldots \quad \sum_{m=0}^{M-1} \bar{\omega}^{\mathrm{rv}}(m)]^T. \tag{3.95}$$

Notice Equation (3.94) collapses to the stationary model linear form $[\bar{\omega} \quad 2\bar{\omega} \quad \ldots \quad M\bar{\omega}]^T$ if $\bar{\omega}(0) = \bar{\omega}(1) = \ldots \bar{\omega}(M)$. A convenient matrix algebra structure is created to transform the M Doppler values in Equation (3.94) into the pulse to pulse Doppler progression of Equation (3.95). An upper triangular matrix of $\bar{\omega}$ values is first created,

$$\bar{\boldsymbol{\Omega}} = \begin{bmatrix} \bar{\omega}^{\mathrm{rv}}(0) & \bar{\omega}^{\mathrm{rv}}(1) & \bar{\omega}^{\mathrm{rv}}(2) & \ldots & \bar{\omega}^{\mathrm{rv}}(M-1) \\ 0 & \bar{\omega}^{\mathrm{rv}}(0) & \bar{\omega}^{\mathrm{rv}}(1) & \ldots & \bar{\omega}^{\mathrm{rv}}(M-2) \\ 0 & 0 & \bar{\omega}^{\mathrm{rv}}(0) & \ldots & \vdots \\ 0 & 0 & \ldots & \ddots & \vdots \\ 0 & 0 & \ldots & \ldots & \bar{\omega}^{\mathrm{rv}}(0) \end{bmatrix}$$

where the subscript represents the pulse number within the CPI. Multiplying $\bar{\boldsymbol{\Omega}}$ by a ones column vector of length M yields the progression given in Equation (3.95),

$$\bar{\mathbf{w}}^{\mathrm{rv}} = \bar{\boldsymbol{\Omega}} \mathbf{1}_{\mathrm{M}} \tag{3.96}$$

$$= [\bar{\omega}^{\mathrm{rv}}(0) \quad [\bar{\omega}^{\mathrm{rv}}(0) + \bar{\omega}^{\mathrm{rv}}(1)] \quad \ldots \quad \sum_{m=0}^{M-1} \bar{\omega}^{\mathrm{rv}}(m)]^T. \tag{3.97}$$

And the corresponding pulse to pulse Doppler phase contribution is the $M \times 1$ vector $e^{j2\pi\bar{\mathbf{w}}}$. Although Equation (3.97) produces a $M \times 1$ column vector dimensionally the same as the stationary model, the $M \times 1$ vector must be recast into a MNP vector

67

to match $\tilde{\mathbf{a}}(\boldsymbol{\vartheta}_x^{\mathrm{rv}})$ and $\tilde{\mathbf{e}}(\boldsymbol{\vartheta}_z^{\mathrm{rv}})$. The per element per pulse phase contribution due to Doppler element is created by,

$$\tilde{\mathbf{b}}(\bar{\mathbf{w}}) = e^{j2\pi \mathbf{1_P} \otimes \bar{\mathbf{w}} \otimes \mathbf{1_N}}. \tag{3.98}$$

And the complete steering vector with motion to location (θ, ϕ) is therefore given by

$$\tilde{\mathbf{v}} = \tilde{\mathbf{e}}(\boldsymbol{\vartheta}_z^{\mathrm{rv}}) \odot \tilde{\mathbf{b}}(\bar{\mathbf{w}}) \odot \tilde{\mathbf{a}}(\boldsymbol{\vartheta}_x^{\mathrm{rv}}), \tag{3.99}$$

where $\tilde{\mathbf{e}}$ represents the spatial-temporal phase contribution due to vertical element separation, $\tilde{\mathbf{b}}$ represents the temporal-spatial phase contribution due to Doppler, and $\tilde{\mathbf{a}}$ represents the spatial-temporal phase contribution due to horizontal element separation. Both the maneuver steering vector of Equation (3.99) and stationary steering vector of Equation (2.26) are $MNP \times 1$.

The introduction of platform maneuver resulted in M values for previously defined single value characteristics. New $MNP \times 1$ spatial-temporal ($\tilde{\mathbf{e}}$, $\tilde{\mathbf{a}}$) and temporal-spatial ($\tilde{\mathbf{b}}$) steering vectors replaced the original spatial ($\mathbf{e}$, $\mathbf{a}$) and temporal ($\mathbf{b}$) steering vectors of the stationary model. The $\mathbf{e} \otimes \mathbf{b} \otimes \mathbf{a}$ steering vector paradigm was subsequently replace by $\tilde{\mathbf{e}} \odot \tilde{\mathbf{b}} \odot \tilde{\mathbf{a}}$. The final piece needed for a space-time snapshot remains the return amplitude with motion.

3.4.3   Return Amplitude with Motion.   The complete space-time snapshot to a location is the return amplitude times the steering vector,

$$\boldsymbol{\chi} = \alpha \mathbf{v}. \tag{3.100}$$

Previously α was assumed constant throughout the CPI. The assumption was viable because the environment was identically illuminated throughout the CPI. Platform maneuver invalidates that assumption as locations are now illuminated differently as the platform rotates. The amplitude must be recalculated each pulse, resulting in a

$M \times 1$ vector of amplitudes. The actual calculations of these amplitudes are discussed in the target model (Section 3.5) and clutter model (Section 3.6). The formatting of these $M \times 1$ vector of amplitudes to match the maneuver steering vector framework is discussed here. With the $M \times 1$ vector of amplitudes given by $\boldsymbol{\alpha}$, the $MNP \times 1$ amplitude vector is

$$\tilde{\boldsymbol{\alpha}} = \mathbf{1}_\mathrm{P} \otimes \boldsymbol{\alpha} \otimes \mathbf{1}_\mathrm{N}. \tag{3.101}$$

And the complete space-time snapshot with platform maneuver is given by

$$\tilde{\boldsymbol{\chi}} = \tilde{\boldsymbol{\alpha}} \odot \tilde{\mathbf{e}}(\boldsymbol{\vartheta}_z^\mathrm{rv}) \odot \tilde{\mathbf{b}}(\bar{\mathbf{w}}) \odot \tilde{\mathbf{a}}(\boldsymbol{\vartheta}_x^\mathrm{rv}). \tag{3.102}$$

The target and clutter models are next developed incorporating platform maneuver. Note the four $M \times 1$ components required to build the target and clutter models: return amplitude $\boldsymbol{\alpha}$, spatial frequencies $\boldsymbol{\vartheta}_x^\mathrm{rv}$ and $\boldsymbol{\vartheta}_z^\mathrm{rv}$, and normalized Doppler frequency $\bar{\boldsymbol{\omega}}$. Once these $M \times 1$ quantities are characterized, the formatting methodology built in this section produces the space-time snapshot. Equation (3.101) formats the M return amplitudes $\boldsymbol{\alpha}$ into the $MNP \times 1$ $\tilde{\boldsymbol{\alpha}}$. Equation (3.87) formats the M horizontal spatial frequencies into the $MNP \times 1$ spatial-temporal steering vector $\tilde{\mathbf{a}}(\boldsymbol{\vartheta}_x^\mathrm{rv})$. Equation (3.88) formats the M vertical spatial frequencies into the $MNP \times 1$ spatial-temporal steering vector $\tilde{\mathbf{e}}(\boldsymbol{\vartheta}_z^\mathrm{rv})$. Equations (3.94-3.97) format the M normalized Doppler frequencies into the $MNP \times 1$ temporal-spatial steering vector $\tilde{\mathbf{b}}(\bar{\mathbf{w}})$. And finally Equation (3.102) combines the three $MNP \times 1$ steering vectors capturing the return phase and one $MNP \times 1$ steering vector capturing the return magnitudes into the complete space-time snapshot.

3.5   Target Model

The four $M \times 1$ components required to build the target model are: return amplitude $\boldsymbol{\alpha}_t$, spatial frequencies $\boldsymbol{\vartheta}_x^\mathrm{rv}$ and $\boldsymbol{\vartheta}_z^\mathrm{rv}$, and normalized Doppler frequency $\bar{\boldsymbol{\omega}}_t$. The target location is defined as (θ_t, ϕ_t) as measured from the stationary platform orientation. Platform maneuver yields M azimuth and elevation angles on transmit,

$(\boldsymbol{\theta}^{\mathrm{tx}}, \boldsymbol{\phi}^{\mathrm{tx}})$, and M on receiver, $(\boldsymbol{\theta}^{\mathrm{rv}}, \boldsymbol{\phi}^{\mathrm{rv}})$. The stationary model Signal-to-Noise-Ratio (SNR) is defined as [3]

$$\xi_t = \frac{P_t G(\theta_t, \phi_t) g(\theta_t, \phi_t) \lambda^2 \sigma_t}{(4\pi)^3 N B L_s R_t(\theta)^4}, \tag{3.103}$$

where P_t is transmit power, G is transmit array gain, g is element pattern power on receive, λ is transmit wavelength, σ_t is target radar cross section (RCS), NBL_s are noise and system losses, and R_t is range to target. In the stationary model's implementation the SNR is set to unity. In both models the target snapshot amplitudes obey [3]

$$\mathcal{E}\{\alpha_t \alpha_t\} = \sigma^2 \xi_t, \tag{3.104}$$

where σ^2 is the noise power. A constant SNR in the stationary model is valid because the target is illuminated identically throughout the CPI. However, a constant maneuver model SNR fails to capture the true target return magnitude. A target may reside in the mainbeam, sidelobes, and nulls within a single CPI and returns from pulse to pulse may have varying SNR. Returning to the stationary model SNR definition of Equation (3.103), the only platform maneuver induced changes are the transmit array gain $G(\theta_t, \phi_t)$ and receive element pattern $g(\theta_t, \phi_t)$, introducing M values of each quantity. Compared to the stationary model, the maneuver model SNR will be greater if $G(\boldsymbol{\theta}^{\mathrm{tx}}, \boldsymbol{\phi}^{\mathrm{tx}}) g(\boldsymbol{\theta}^{\mathrm{rv}}, \boldsymbol{\phi}^{\mathrm{rv}}) > G(\theta_t, \phi_t) g(\theta_t, \phi_t)$, and less if $G(\boldsymbol{\theta}^{\mathrm{tx}}, \boldsymbol{\phi}^{\mathrm{tx}}) g(\boldsymbol{\theta}^{\mathrm{rv}}, \boldsymbol{\phi}^{\mathrm{rv}}) < G(\theta_t, \phi_t) g(\theta_t, \phi_t)$. The maneuver model SNR is therefore defined as a scaled function of the stationary model $G(\theta_t, \phi_t) g(\theta_t, \phi_t)$,

$$\dot{\boldsymbol{\xi}}_t = \xi_t \frac{\mathbf{G}(\boldsymbol{\theta}^{\mathrm{tx}}, \boldsymbol{\phi}^{\mathrm{tx}}) \odot \mathbf{g}(\boldsymbol{\theta}^{\mathrm{rv}}, \boldsymbol{\phi}^{\mathrm{rv}})}{G(\theta_t, \phi_t) g(\theta_t, \phi_t)}. \tag{3.105}$$

Anytime $G(\boldsymbol{\theta}^{\mathrm{tx}}, \boldsymbol{\phi}^{\mathrm{tx}}) g(\boldsymbol{\theta}^{\mathrm{rv}}, \boldsymbol{\phi}^{\mathrm{rv}}) = G(\theta_t, \phi_t) g(\theta_t, \phi_t)$, the target is illuminated exactly the same in both models and the maneuver SNR will be equal to the stationary SNR. Anytime $G(\boldsymbol{\theta}^{\mathrm{tx}}, \boldsymbol{\phi}^{\mathrm{tx}}) g(\boldsymbol{\theta}^{\mathrm{rv}}, \boldsymbol{\phi}^{\mathrm{rv}}) > G(\theta_t, \phi_t) g(\theta_t, \phi_t)$, the target is illuminated at a higher power in the maneuver model and the SNR will be greater than the stationary SNR. And anytime $G(\boldsymbol{\theta}^{\mathrm{tx}}, \boldsymbol{\phi}^{\mathrm{tx}}) g(\boldsymbol{\theta}^{\mathrm{rv}}, \boldsymbol{\phi}^{\mathrm{rv}}) < G(\theta_t, \phi_t) g(\theta_t, \phi_t)$, the target is illuminated at a lower power in the maneuver model and the SNR will be less than the stationary

SNR. The $M \times 1$ SNR values of Equation (3.105) are reshaped into the $MNP \times 1$ values by

$$\tilde{\boldsymbol{\xi}}_t = \mathbf{1}_{\text{P}} \otimes \dot{\boldsymbol{\xi}}_t \otimes \mathbf{1}_{\text{N}}. \tag{3.106}$$

And by the definition in Equation (3.104), the $MNP \times 1$ vector of target amplitudes is

$$\tilde{\boldsymbol{\alpha}}_t = \sigma \sqrt{\tilde{\boldsymbol{\xi}}_t} \tag{3.107}$$

With the target amplitude characterized in Equation (3.107), the next target model component requiring characterization is normalized Doppler. Target velocity may include $\hat{\mathbf{x}}$, $\hat{\mathbf{y}}$, and $\hat{\mathbf{z}}$ components, denoted v_{t_x}, v_{t_y}, and v_{t_z}.

$$\vec{\mathbf{v}}_t = v_{t_x}\hat{\mathbf{x}} + v_{t_y}\hat{\mathbf{y}} + v_{t_z}\hat{\mathbf{z}} \tag{3.108}$$

The normalized Doppler frequency for a target at (θ_t, ϕ_t) was present in Equation (2.45) as

$$\bar{\omega}_t = 2\frac{(v_a + v_t^x)\cos\theta_t \sin\phi_t + v_t^y \cos\theta_t \cos\phi_t + v_t^z \sin\theta_t}{\lambda f_r}. \tag{3.109}$$

No consideration of the target direction of travel was necessary in the stationary model. Because the relative velocity between the aircraft and target was constant, the Doppler frequency was constant and $\bar{\omega}$ could simply be assigned a value that would not change during the CPI. When platform maneuver is induced, a target will possess a different Doppler frequency at each platform orientation. Target velocity is restricted to $v_{t_y}\hat{\mathbf{y}}$ in this model's implementation, corresponding to the target travelling toward the aircraft along the y-axis at speed v_{t_y} and given by

$$\vec{\mathbf{v}}_t = v_{t_y}\hat{\mathbf{y}}. \tag{3.110}$$

The normalized Doppler expression with restricted target velocity becomes

$$\bar{\omega}_t = 2\frac{v_a \cos\theta_t \sin\phi_t + v_t^y \cos\theta_t \cos\phi_t}{\lambda f_r}. \tag{3.111}$$

71

In the production of SINR plots, a target normalized Doppler is specified. The maneuver target model will therefore calculate the target velocity required to produce the original normalized Doppler value of interest by

$$v_{t_y} = \frac{\bar{\omega}_t \lambda f_r - v_a \cos \theta_t \sin \phi_t}{\cos \theta_t \cos \phi_t}.$$
(3.112)

And the M normalized Doppler values for the target at (θ_t, ϕ_t) then become

$$\bar{\boldsymbol{\omega}}_t = 2 \frac{v_a \cos \boldsymbol{\theta}^{\text{rv}} \odot \sin \boldsymbol{\phi}^{\text{rv}} + v_t^y \cos \boldsymbol{\theta}^{\text{rv}} \odot cos\boldsymbol{\phi}^{\text{rv}}}{\lambda f_r}.$$
(3.113)

The target temporal steering vector with motion is constructed with the upper triangular matrix

$$\bar{\boldsymbol{\Omega}}_t = \begin{bmatrix} \bar{\omega}_t(0) & \bar{\omega}_t(1) & \bar{\omega}_t(2) & \dots & \bar{\omega}_t(M-1) \\ 0 & \bar{\omega}_t(0) & \bar{\omega}_t(1) & \dots & \bar{\omega}_t(M-2) \\ 0 & 0 & \bar{\omega}_t(0) & \dots & \vdots \\ 0 & 0 & \dots & \ddots & \vdots \\ 0 & 0 & \dots & \dots & \bar{\omega}_t(0) \end{bmatrix}$$

multiplied by the $M \times 1$ vector of ones

$$\bar{\mathbf{w}}_t = \bar{\boldsymbol{\Omega}}_t \mathbf{1}_M,$$
(3.114)

and recast into the $MNP \times 1$ snapshot sequence by

$$\tilde{\mathbf{b}}_t(\bar{\mathbf{w}}_t) = e^{j2\pi \mathbf{1_P} \otimes \bar{\mathbf{w}}_t \otimes \mathbf{1_N}}.$$
(3.115)

The final two pieces of the target space-time snapshot are the spatial-temporal steering vectors describing the phase contribution due to element separation. The $M \times 1$ spatial frequencies are given by

$$\tilde{\boldsymbol{\vartheta}}_x^{\text{rv}} = \frac{d_x \cos \boldsymbol{\theta}^{\text{rv}} \odot \sin \boldsymbol{\phi}^{\text{rv}}}{c}$$
(3.116)

and

$$\tilde{\boldsymbol{\vartheta}}_z^{\text{rv}} = \frac{d_z \sin \boldsymbol{\theta}'}{c}, \tag{3.117}$$

where $\boldsymbol{\theta}^{\text{rv}}$ and $\boldsymbol{\phi}^{\text{rv}}$ are the M radar angles to the target at (θ, ϕ). The corresponding steering vectors are given by

$$\tilde{\mathbf{a}}_t(\boldsymbol{\vartheta}_x^{\text{rv}}) = e^{j 2\pi \mathbf{1_p} \otimes \boldsymbol{\vartheta}_x^{\text{rv}} \otimes \mathbf{N}} \tag{3.118}$$

and

$$\tilde{\mathbf{e}}_t(\boldsymbol{\vartheta}_z^{\text{rv}}) = e^{j 2\pi \mathbf{P} \otimes \boldsymbol{\vartheta}_z^{\text{rv}} \otimes \mathbf{1_N}}, \tag{3.119}$$

And the complete target snapshot can now be assembled as

$$\tilde{\boldsymbol{\chi}}_t = \tilde{\boldsymbol{\alpha}}_t \odot \tilde{\mathbf{e}}_t(\boldsymbol{\vartheta}_z^{\text{rv}}) \odot \tilde{\mathbf{b}}_t(\bar{\mathbf{w}}_t) \odot \tilde{\mathbf{a}}_t(\boldsymbol{\vartheta}_x^{\text{rv}}) \tag{3.120}$$

3.6 Clutter Model

Accurate characterization of the clutter environment requires a return amplitude $\boldsymbol{\alpha}_{ik}$, spatial frequencies $\boldsymbol{\vartheta}_x^{\text{rv}}$ and $\boldsymbol{\vartheta}_z^{\text{rv}}$, and normalized Doppler frequency $\bar{\boldsymbol{\omega}}_{ik}$ for each ik patch. The clutter location is defined as (θ_{ik}, ϕ_{ik}) as measured from the stationary platform orientation. Platform maneuver yields M azimuth and elevation angles on transmit, $(\theta^{\text{tx}}, \phi^{\text{tx}})$, and M on receiver, $(\theta^{\text{rv}}, \phi^{\text{rv}})$.

The patch is now illuminated differently each pulse, requiring per pulse calculation of Clutter-to-Noise-Ration (CNR) ξ_{ik} and amplitude α_{ik}. The stationary model CNR is defined as [3]

$$\xi_{ik} = \frac{P_t G(\theta_t, \phi_t) g(\theta_t, \phi_t) \lambda^2 \sigma_{ik}}{(4\pi)^3 NBL_s R_{ik}(\theta)^4}, \tag{3.121}$$

where P_t is transmit power, G is transmit array gain, g is element pattern power on receive, λ is transmit wavelength, σ_{ik} is clutter patch RCS, NBL_s are noise and system losses, and R_{ik} is range to the patch. The patch RCS definition of Equation (2.63) remains unchanged because the patch area, grazing angle, and reflectivity are

unchanged. The M CNR values are given by

$$\dot{\boldsymbol{\xi}}_{ik} = \xi_{ik} \frac{P_t \mathbf{G}(\boldsymbol{\theta}^{\mathrm{tx}}, \boldsymbol{\phi}^{\mathrm{tx}}) \odot \mathbf{g}(\boldsymbol{\theta}^{\mathrm{rv}}) \lambda^2 \sigma_{ik}}{(4\pi)^3 NBL_s R_{ik}(\theta)^4}, \tag{3.122}$$

and are recast into $MNP \times 1$ column vector by

$$\tilde{\boldsymbol{\xi}}_{ik} = \mathbf{1_P} \otimes \dot{\boldsymbol{\xi}}_{ik} \otimes \mathbf{1_N}. \tag{3.123}$$

The complex amplitude $\tilde{\boldsymbol{\alpha}}_{ik}$ obeys

$$\mathcal{E}\{\tilde{\boldsymbol{\alpha}}_{ikm}\tilde{\boldsymbol{\alpha}}^*_{jln}\} = \sigma^2 \sqrt{\tilde{\boldsymbol{\xi}}_{ikm}\tilde{\boldsymbol{\xi}}_{jln}} \delta_{i-j}\delta_{k-l}, \tag{3.124}$$

meaning the returns from different clutter patches are uncorrelated. Next consider the M Doppler values a single patch and the construction of the $MNP \times 1$ temporal-spatial steering vector that captures the phase contribution due to Doppler.

A clutter patch was previously located at one θ, one ϕ, one $\bar{\omega}$, and one return amplitude α_c. The normalized Doppler frequency for a patch at (θ,ϕ) was presented in Equation (2.55) as

$$\bar{\omega}_{ik} = 2\frac{v_a \cos\theta_{ik}\sin\phi_{ik}}{\lambda f_r}. \tag{3.125}$$

The M normalized Doppler values for a target at (θ,ϕ) are given by

$$\bar{\boldsymbol{\omega}}_{ik} = 2\frac{v_a \cos\boldsymbol{\theta}^{\mathrm{rv}} \odot \sin\boldsymbol{\phi}^{\mathrm{rv}}}{\lambda f_r}. \tag{3.126}$$

The clutter patch temporal steering vector with motion is constructed with the upper triangular matrix

$$
\bar{\boldsymbol{\Omega}}_{ik} = \begin{bmatrix}
\bar{\omega}_{ik}(0) & \bar{\omega}_{ik}(1) & \bar{\omega}_{ik}(2) & \dots & \bar{\omega}_{ik}(M-1) \\
0 & \bar{\omega}_{ik}(0) & \bar{\omega}_{ik}(1) & \dots & \bar{\omega}_{ik}(M-2) \\
0 & 0 & \bar{\omega}_{ik}(0) & \dots & \vdots \\
0 & 0 & \dots & \ddots & \vdots \\
0 & 0 & \dots & \dots & \bar{\omega}_{ik}(0)
\end{bmatrix}
$$

multiplied by the $M \times 1$ vector of ones

$$
\bar{\mathbf{w}}_{ik} = \bar{\boldsymbol{\Omega}}_{ik}\mathbf{1}_{\mathrm{M}}. \tag{3.127}
$$

And recast into the $MNP \times 1$ form by

$$
\tilde{\mathbf{b}}_{ik}(\bar{\mathbf{w}}_{ik}) = e^{j2\pi\mathbf{1}_{\mathbf{P}}\otimes\bar{\mathbf{w}}_{ik}\otimes\mathbf{1}_{\mathbf{N}}}. \tag{3.128}
$$

The final pieces needed for the clutter space-time snapshot are the spatial-temporal steering vectors, given by

$$
\tilde{\mathbf{a}}_{ik}(\boldsymbol{\vartheta}_x^{\mathrm{rv}}) = e^{j2\pi\mathbf{1}_{\mathbf{P}}\otimes\boldsymbol{\vartheta}_x^{\mathrm{rv}}\otimes\mathbf{N}} \tag{3.129}
$$

and

$$
\tilde{\mathbf{e}}_{ik}(\boldsymbol{\vartheta}_z^{\mathrm{rv}}) = e^{j2\pi\mathbf{P}\otimes\boldsymbol{\vartheta}_z^{\mathrm{rv}}\otimes\mathbf{1}_{\mathbf{N}}}. \tag{3.130}
$$

The antenna array radiates in all directions, illuminating every $i \times k$ clutter patch. Therefore, the complete clutter space-time snapshot is the sum of $i \times k$ clutter patch snapshot

$$
\tilde{\boldsymbol{\chi}}_c = \sum_{i=0}^{N_r-1}\sum_{k=0}^{N_c-1} \tilde{\boldsymbol{\alpha}}_{ik} \odot \tilde{\mathbf{e}}(\boldsymbol{\vartheta}_z^{\mathrm{rv}}) \odot \tilde{\mathbf{b}}(\bar{\mathbf{w}}_{ik}) \odot \tilde{\mathbf{a}}(\boldsymbol{\vartheta}_{ik}^{\mathrm{rv}}) \tag{3.131}
$$

75

And the clutter covariance matrix with platform maneuver is given by,

$$
\begin{aligned}
\tilde{\mathbf{R}}_c &= \mathcal{E}\{\tilde{\boldsymbol{\chi}}_c \tilde{\boldsymbol{\chi}}_c^H\} \tag{3.132}\\
&= \sigma^2 \sum_{i=0}^{N_r-1} \sum_{k=0}^{N_c-1} \left(\sqrt{\tilde{\boldsymbol{\xi}}_{ik}} \odot \tilde{\mathbf{e}}(\boldsymbol{\vartheta}_z^{\mathrm{rv}}) \odot \tilde{\mathbf{b}}(\bar{\mathbf{w}}_{ik}) \odot \tilde{\mathbf{a}}(\boldsymbol{\vartheta}_x^{\mathrm{rv}}) \right) \\
&\qquad \left(\sqrt{\tilde{\boldsymbol{\xi}}_{ik}} \odot \tilde{\mathbf{e}}(\boldsymbol{\vartheta}_z^{\mathrm{rv}}) \odot \tilde{\mathbf{b}}(\bar{\mathbf{w}}_{ik}) \odot \tilde{\mathbf{a}}(\boldsymbol{\vartheta}_x^{\mathrm{rv}}) \right)^H . \tag{3.133}
\end{aligned}
$$

3.7 Maneuver Model Summary

This Chapter developed a maneuver model based on the popular stationary model of [3, 10]. The maneuver model developed can simulate any degree of pitch, roll, yaw, or any combination of the three. This research focuses on development of the model itself, and therefore the model investigates individual rotations versus specific innovative and complex maneuver scenarios. The overriding theme of the maneuver model is that singular quantities in the stationary model of [3, 10] possess M unique quantities in the maneuver model. The platform defines the reference coordinate system at all times. The (θ, ϕ) radar coordinates of each clutter patch and the target are first transformed into their cartesian counterparts (x,y,z). Rotation matrices are used to recalculate the coordinates to each (x,y,z) point based on the amount of rotation, measured with the platform orientation as the reference. The resulting (x',y',z') coordinates are transformed back to radar coordinates (θ', ϕ'). Each location has M (θ', ϕ') pairs on transmit and receive, translating to M Doppler frequencies, spatial frequencies, and amplitudes. Four $MNP \times 1$ vectors are created, one for amplitude, one each for phase contributions due horizontal spacing, vertical spacing, and Doppler. The Kronecker product paradigm is replaced with the Hadamard product in creating the space-time snapshots. The maneuver models allows characterization of the target and interference (thermal noise and clutter for this research) environment. The next logical step is investigating maneuver impacts on the interference environment, MF output SINR, and sample support homogeneity. These topics are addressed next in Chapter IV.

IV. Maneuver Effects on Clutter Spectrum, SINR, and Homogeneity

U sing the model developed in Chapter III, platform maneuver effects are simulated for the side-looking (SL) airborne radar. The objective is characterization of maneuver effects on clutter spectrum, Matched Filter (MF) Signal-to-Interference-plus-Noise-Ratio (SINR), and sample support homogeneity. The number of azimuth channels, elevation channels, and target ranges are varied to gain insight into maneuver effects. A rotation rate of $800°$/sec and pulse length of 32 pulses is used unless otherwise noted. The rotation rate corresponds to $12.86°$ total rotation during the CPI, similar to the forward-looking (FL) work in [4]. The number of azimuth and elevation channels is varied on a case by case basis to illustrate maneuver effects. The focus is airborne moving target indication, thus the array is steered to boresight ($\theta = 0$, $\phi = 0$). The array is steered at boresight throughout the coherent processing interval, but its orientation relative to the clutter and target changes as the platform rotates. Two key phenomenon identified are strongly correlated with Matched Filter (MF) Signal-to-Interference-plus-Noise (SINR) and sample support homogeneity. The first is the maneuver induced differences in clutter illumination, and the second is the maneuver induced differences in target illumination. As each maneuver type is examined, visual plots depicting these (target and clutter illumination) differences are used to illustrate maneuver effect and gain insight. Azimuthal antenna pattern cuts illustrate the clutter illumination magnitudes at specific ranges. Signal Match (SM) power spectral density (PSD) and minimum variance estimate (MVE) plots illustrate the changes in the clutter environment. Signal-to-Noise-Ratio (SNR) plots depict changes in target illumination. These characterizations of the changing interference environment and target illumination lead directly into the MF SINR and data homogeneity results. The results are organized as follows:

Section 4.1 gives a brief review of the clutter spectral estimations and performance metrics, and their specific implementation within the stationary and maneuver models. Section 4.2-4.4 describes the pitch, roll, and yaw effects for linear and planar

arrays at two target ranges. And Section 4.5 describes the maneuver induced hetero-geneities in the sample support vectors. The simulation parameters are described in Table 4.1.

4.1 Spectral Estimation and Performance Metrics

The SM spectral estimation method was presented in Chapter II and is applied here. The stationary PSD is given by

$$P = \frac{\mathbf{v}^H \mathbf{R} \mathbf{v}}{\mathbf{v}^H \mathbf{v}}, \tag{4.1}$$

where

$$\mathbf{v} = \mathbf{e}(\vartheta_z) \otimes \mathbf{b}(\bar{\omega}) \otimes \mathbf{a}(\bar{\omega}), \tag{4.2}$$

$$\mathbf{R} = \mathbf{R}_n + \mathbf{R}_c, \tag{4.3}$$

and

$$\begin{aligned}
\mathbf{R}_c &= \mathcal{E}\{\boldsymbol{\chi}\boldsymbol{\chi}^H\} \\
&= \sigma^2 \sum_{i=0}^{N_r-1} \sum_{k=0}^{N_c-1} \xi_{ik} \mathbf{e}(\vartheta_z)\mathbf{e}(\vartheta_z)^H \otimes \mathbf{b}(\bar{\omega})\mathbf{b}(\bar{\omega})^H \otimes \mathbf{a}(\vartheta_x)\mathbf{a}(\vartheta_x)^H.
\end{aligned} \tag{4.4}$$

The maneuver PSD is given by

$$\tilde{P} = \frac{\mathbf{v}^H \tilde{\mathbf{R}} \mathbf{v}}{\mathbf{v}^H \mathbf{v}}, \tag{4.5}$$

where,

$$\tilde{\mathbf{R}} = \mathbf{R}_n + \tilde{\mathbf{R}}_c, \tag{4.6}$$

78

Table 4.1:   Simulations parameters.

Variable	Value
M	32
N	varied
P	varied
f_o	1240 MHz
f_r	1984 Hz
T_p	0.8 μs
P_t	200 kW
B	800 kHz
F_n (Noise Figure)	3 dB
N_c	361
h_a (aircraft altitude)	3073 m
v_a (aircraft velocity)	$\frac{d_x f_r}{2}$
R	11,66 km
γ	-3 dB
Array Transmit Gain	22 dB
Element Pattern	Cosine
Element Gain	4 dB
Element Backlobe Level	-30 dB
d_x	0.10922 m
d_z	0.1407 m
Transmit Taper	Uniform (None)
System Losses L_s	3 dB
Target ϕ	0°
Target θ	0°
B_c	$\frac{10}{f_r}$
G_e	4 dB
ρ (rotation rate)	800°/sec
ξ_t (stationary)	1

and

$$\tilde{\mathbf{R}}_c = \mathcal{E}\{\tilde{\boldsymbol{\chi}}_c \tilde{\boldsymbol{\chi}}_c^H\} \tag{4.7}$$

$$= \sigma^2 \sum_{i=0}^{N_r-1} \sum_{k=0}^{N_c-1} \left(\sqrt{\tilde{\boldsymbol{\xi}}_{ik}} \odot \tilde{\mathbf{e}}(\boldsymbol{\vartheta}_z^{\mathrm{rv}}) \odot \tilde{\mathbf{b}}(\bar{\mathbf{w}}_{ik}) \odot \tilde{\mathbf{a}}(\boldsymbol{\vartheta}_x^{\mathrm{rv}}) \right)$$

$$\left(\sqrt{\tilde{\boldsymbol{\xi}}_{ik}} \odot \tilde{\mathbf{e}}(\boldsymbol{\vartheta}_z^{\mathrm{rv}}) \odot \tilde{\mathbf{b}}(\bar{\mathbf{w}}_{ik}) \odot \tilde{\mathbf{a}}(\boldsymbol{\vartheta}_x^{\mathrm{rv}}) \right)^H. \tag{4.8}$$

The stationary Minimum Variance Estimate, discussed in Chapter II, for the stationary scenario is

$$P_{\mathrm{mve}} = (\mathbf{v}^H \mathbf{R}^{-1} \mathbf{v})^{-1}. \tag{4.9}$$

And for the maneuver model is given by

$$\tilde{P}_{\mathrm{mve}} = (\mathbf{v}^H \tilde{\mathbf{R}}^{-1} \mathbf{v})^{-1}. \tag{4.10}$$

The stationary MF output SINR is given by

$$\mathrm{SINR} = \frac{\sigma^2 \xi_t \mid \mathbf{w}^H \mathbf{v}_t \mid^2}{\mathbf{w}^H \mathbf{R} \mathbf{w}}, \tag{4.11}$$

where $\mathbf{w}$ is the non-motion compensated steering vector defined as

$$\mathbf{w} = \mathbf{R}^{-1} \mathbf{v}, \tag{4.12}$$

and ξ_t is set to unity. And the maneuver MF output SINR is given by

$$\mathrm{SINR}^{\mathrm{m}} = \frac{\sigma^2 \mid \tilde{\mathbf{w}}^H (\boldsymbol{\xi}_t \odot \tilde{\mathbf{v}}_t) \mid^2}{\tilde{\mathbf{w}}^H \tilde{\mathbf{R}} \tilde{\mathbf{w}}} \tag{4.13}$$

where

$$\tilde{\mathbf{w}} = \tilde{\mathbf{R}}^{-1} \mathbf{v}. \tag{4.14}$$
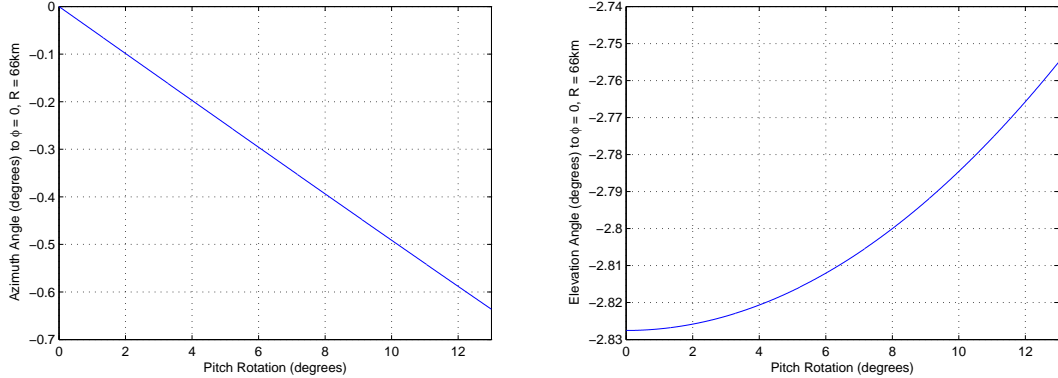
Figure 4.1:   A 12.86° pitch rotation results in only −0.63° change in azimuth angle and +0.07° change in elevation angle to the location $\phi = 0°$ at a range of 66 km.

4.2   Pitch Effects

Platform pitch corresponds to rotation about the y-axis. The antenna is steered to boresight, where the target is located throughout the CPI. In the pitch scenario, the target is always located at boresight despite the platform maneuver. The location of the y-axis, defining boresight and target location, never changes as pitch refers to rotation about that axis. Therefore, the target resides in the main beam at boresight at all times, and is constantly illuminated ($\boldsymbol{\xi}_t = \mathbf{1}_{\mathrm{M}}$).

4.2.1   Linear Array with Target at 11 km and 66 km.   Pitch changes both the azimuth and elevation angles to the location $\phi = 0$ at 66 km, as depicted in Figure 4.1. Notice a 12.86° pitch rotation corresponds to changes in azimuth and elevation of just −0.63° and +0.07° degrees respectively. Significant SINR and detection impact are therefore expected only if the array pattern's azimuth and elevation definition significantly changes over that short span. In the case of the linear array, the pattern lacks elevation definition, and a 3 dB azimuthal beamwidth on the order of 0.63° is not achieved unless N is at least 115 elements long.   Figure 4.2 illustrates an antenna pattern azimuth cut at 66 km for a 120×1 array for the stationary array orientation and for 12.86° pitch orientation, corresponding to the antenna pattern on the final pulse of the CPI. Shorter linear arrays lack the azimuthal definition to

81
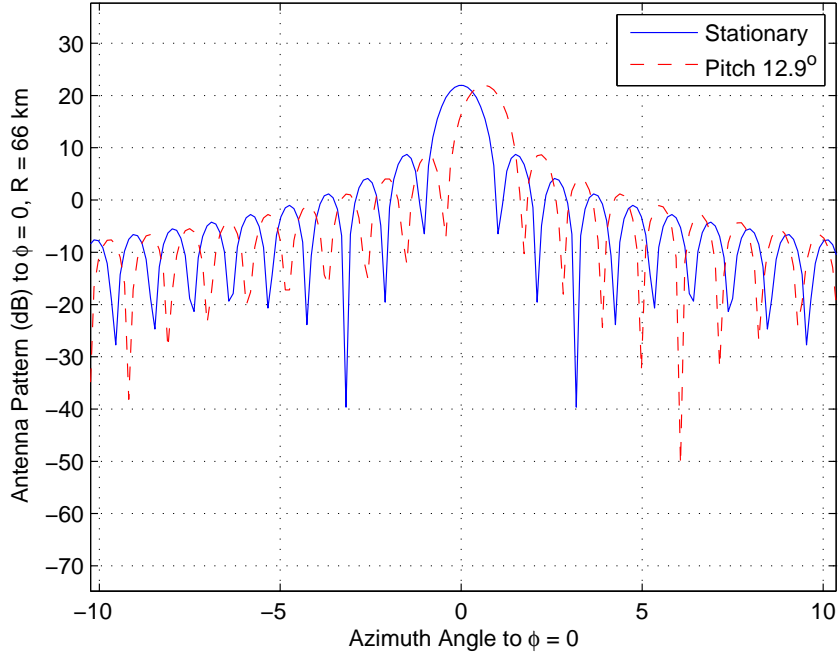
Figure 4.2:   The small change in azimuth and elevation angles at 66 km due to pitch requires greater definition in the antenna pattern to illuminate the ground with any significant difference. A 120×1 array pattern is projected across azimuth at 66 km, demonstrating the need for many elements to achieve any discernable difference.

create significant changes in the clutter illumination at 66 km. Consequently, the clutter environment remains relatively unchanged until the array length approaches 115×1. Figure 4.3 contains four plots depicting SM PSDs and MVEs for both the stationary and pitch scenarios at 66 km. Note, the MVE plots provided are for a 64×1 linear array. The azimuthal and Doppler resolution needed to create complete PSDs for a 120×1 array is processing prohibitive and differences are nearly impossible to see. The 64×1 result provides ample physical insight into the scenario and can be extended to the 120×1 array. Overall, pitch did not have an overwhelming effect on the clutter spectral content. It appears the clutter ridge, the "s"-shaped ridge from negative azimuth and Doppler to positive azimuth and Doppler, shifted slightly in the negative Doppler direction. An azimuthal SM cut at $\phi = 0$ shown in Figure 4.4 confirms the slight negative Doppler shift in the clutter spectrum. The SM PSD cut in Figure 4.4 directly translates to the output SINR plot in Figure 4.5. The increased
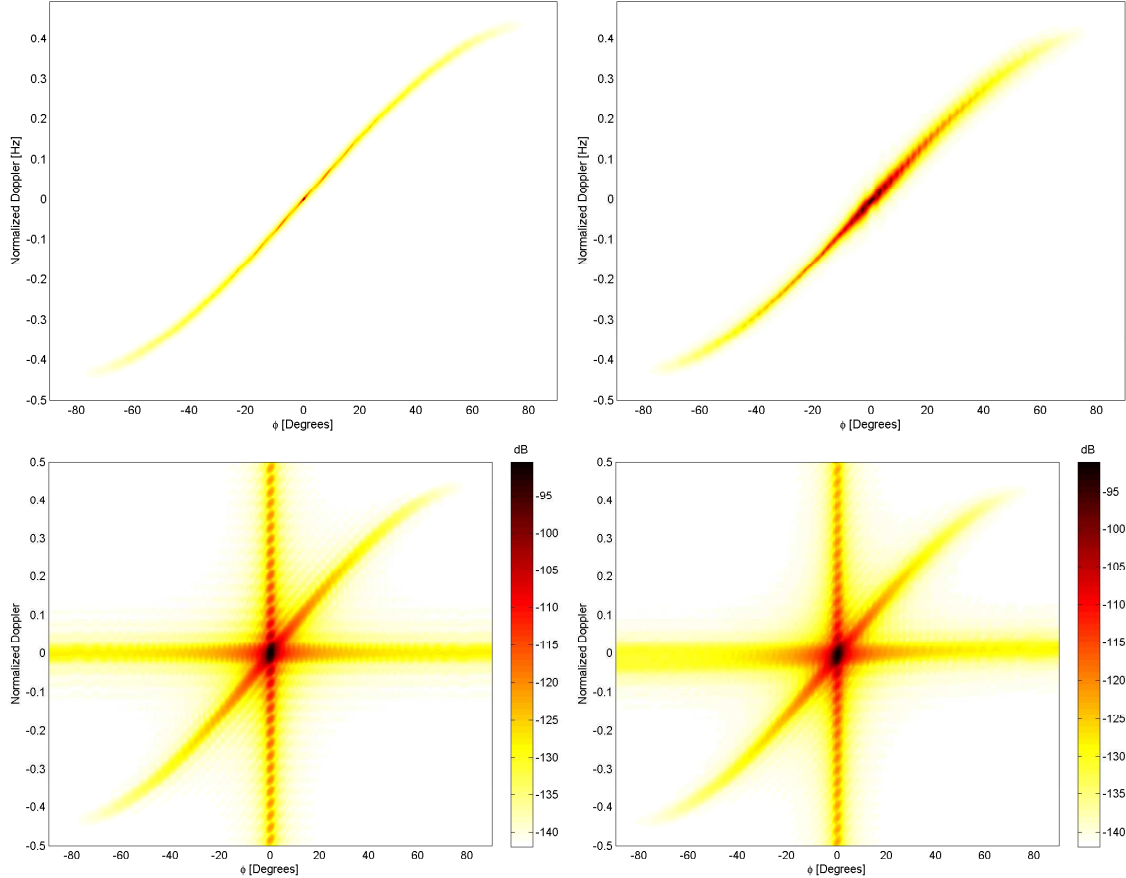
Figure 4.3: Spectral estimation, 64 × 1 array with pitch at 66 km. MVE for the stationary (top left) and pitch (top right) 64 × 1 arrays shows slight spread in the clutter spectrum induced by the pitch rotation. A slight shift towards negative Doppler is noted in the SM PSD pitch scenario (bottom right), compared to the SM PSD stationary (bottom left). This shift is later confirmed with a SM PSD cut at 0 azimuth.

negative clutter power around zero Doppler translates to the SINR degradation when pitch is introduced, labeled with a dashed line and diamond (◇) in Figure 4.5. Notice the improvement between MF and NA performance increases significantly. The MF improvement over NA at 0.1 normalized Doppler was ∼ 20 dB in the stationary scenario. That improvement over NA increased to ∼ 30 dB with pitch maneuver, demonstrating that NA processing is much more susceptible to pitch than the MF.

If the target is located at 11 km versus 66 km, pitch effects are more pronounced. Figure 4.6 shows the azimuth and elevation angles to $\phi = 0$ changes more rapidly as
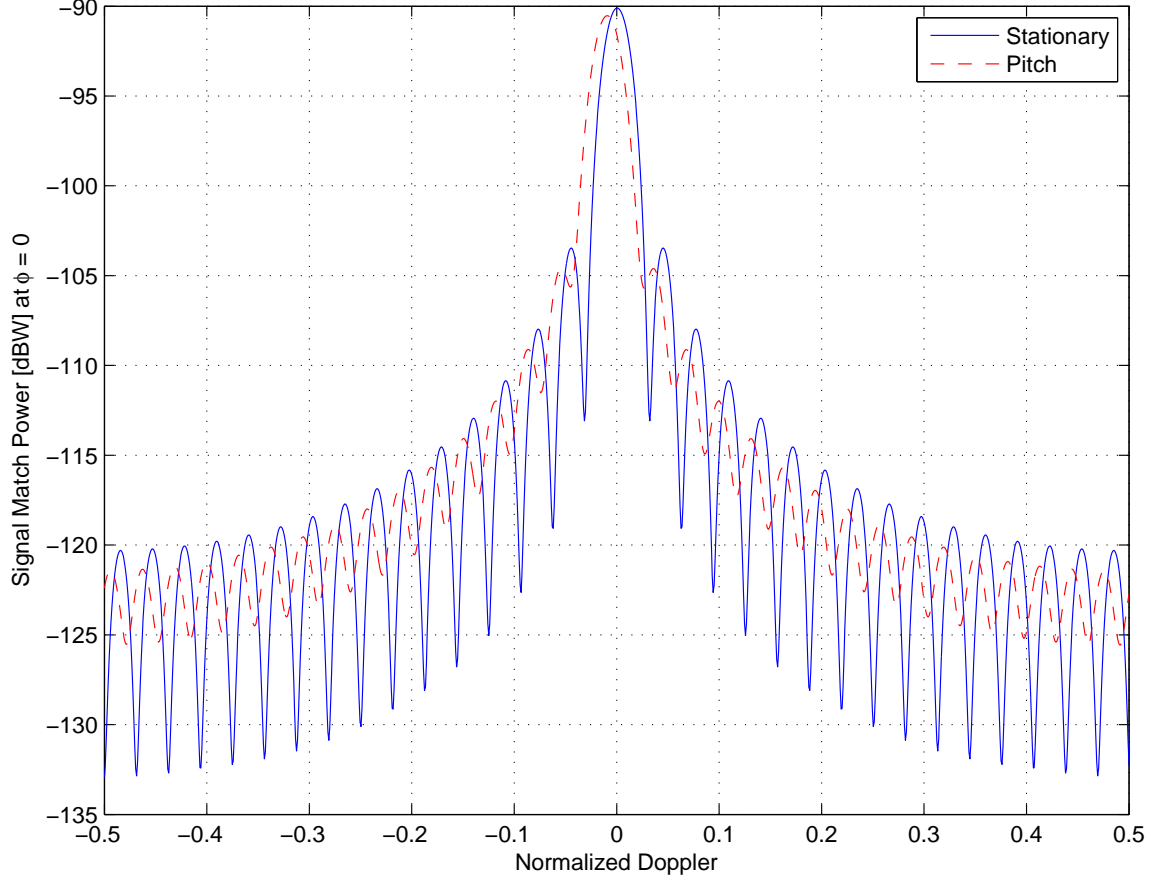
Figure 4.4:   SM PSD cut at zero azimuth, 120×1 with pitch. A slight change in the SM PSD is noted for pitch at 66 km. The shift toward negative Doppler translates to the null shift in the output SINR plot.

range decreases. A $12.86°$ pitch rotation for $\phi = 0$ at 11 km corresponds to changes in azimuth and elevation of $-3.35°$ and $+0.04°$ respectively, a considerable difference from the $-0.63°/ + 0.07°$ at 66 km. The number of azimuth elements required to impact the clutter environment and SINR is reduced from 115 at 66 km to 25 at 11 km. In order to compare results between 11 and 66 km, the 120×1 array is used again. The SM PSD cut for $\phi = 0$ at 11 km is shown in Figure 4.8. The resulting spectral estimates in Figure 4.7 show the dramatic change in the clutter picture. Compared with the cut for $\phi = 0$ at 66 km (Figure 4.4), the negative Doppler shift is much more pronounced and all Doppler lobing structure is lost. The mainbeam width for the 120×1 array is roughly $0.06°$ (see Figure 4.2). An azimuth sweep of $3.35°$,
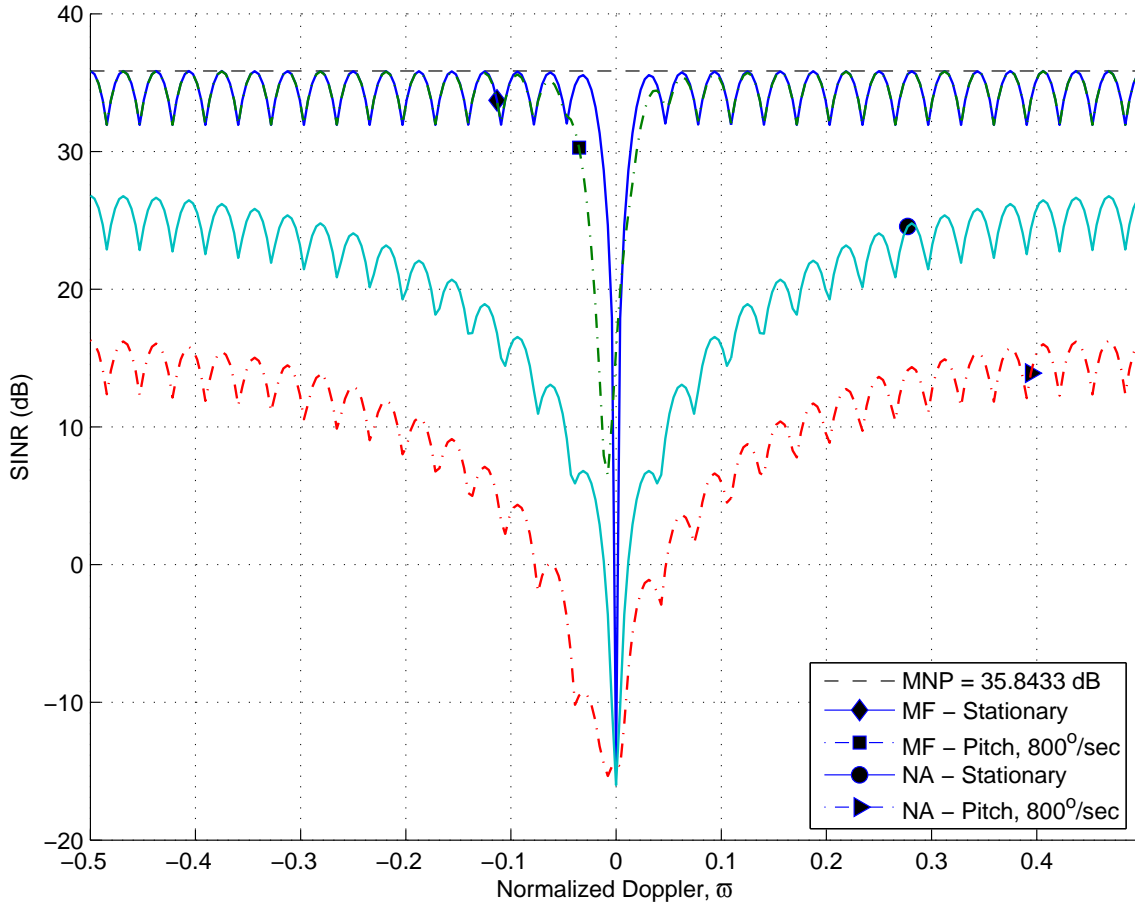
Figure 4.5: Output SINR for 120×1 array with pitch at 66 km. The shift in SM PSD towards negative Doppler is seen in the output SINR. Overall, the array pattern azimuth definition is just approaching the definition needed to cause degradation. Improvement over NA processing with pitch increased considerably.

corresponding to the change in azimuth at 11 km, sweeps through nearly three lobes of the antenna pattern. The clutter illumination for a location at 11 km experiences much greater fluctuation than one at 66 km, and the resulting Doppler spread seen in Figure 4.8 results. The changing clutter environment depicted in the PSD translates to the output SINR in Figure 4.9. First, the widened negative clutter null in the PSD is present in the NA processing SINR. Next, it is also observed in the widening of the main clutter null in the MF. The clutter null actually shifted to negative Doppler, away from zero Hz. Similar to the result at 66km, the MF improvement gap over NA
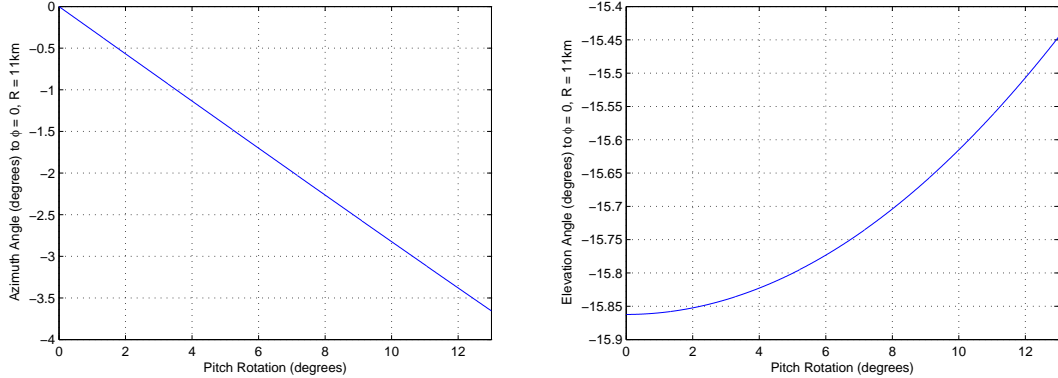
Figure 4.6:   A 12.86° pitch rotation results in a −3.35° change in azimuth angle and +0.04° change in elevation angle to the location $\phi = 0°$ at a range of 11 km. The change in azimuth at 11 km is nearly 3 full degrees more than that at 66 km.

processing widened when pitch was introduced. The increased clutter power due to smaller range resulted in MF improvement of $\sim$ 45 dB over NA processing.

Next, pitch effects are considered for an increasing number of azimuth channels. As the number of azimuth channels are increased, the transmitted antenna pattern gains azimuthal definition. If the azimuth resolution is high enough, the resulting clutter spectrum broadens and shifts. If the resolution is not high enough, the clutter spectrum remains close to the stationary spectrum. Figure 4.10 shows SM cuts at zero azimuth for $N = 100$, 150, and 200. Note, the CPI was shortened to 20 pulses for these plots to computationally allow increased N values. Severe spreading is seen for the 11km scenario, while the 66 km case is relatively stable due to the small changes in azimuth and elevation angles pitch causes at that range. If the azimuth resolution is too low for significant pitch effects, increasing azimuth channels improves MF performance. This result is observed in the narrowing null in the SINR loss plot of Figure 4.11. On the other hand, if the azimuth resolution is high enough such that pitch effects are significant, increasing azimuth channels results in the clutter null spread and shift seen in Figure 4.11.

4.2.2   Planar Array with Target at 11 km and 66 km.   Adding elevation channel changes the antenna pattern and the clutter illumination. The entire array
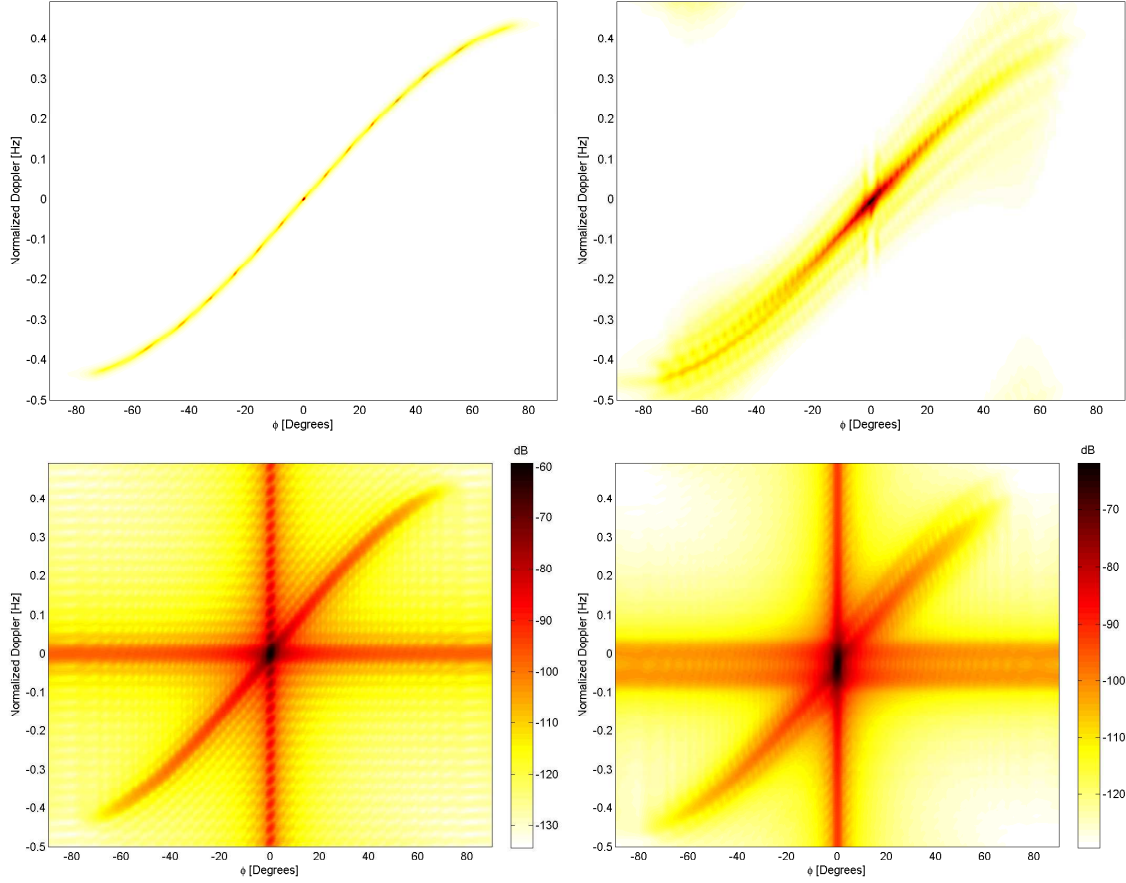
Figure 4.7: Spectral estimation, 64×1 array with pitch at 11 km. MVE for the stationary (top left) and pitch (top right) 64×1 arrays shows slight spread in the clutter spectrum induced by the pitch rotation. A slight shift towards negative Doppler is noted in the SM PSD pitch scenario (bottom right), compared to the SM PSD stationary (bottom left). This shift is later confirmed with a SM PSD cut at 0 azimuth.

gain is normalized to 22 dB, regardless of the total number of elements. Therefore the target (at boresight) remains under the same illumination as the linear array. However, the clutter is illuminated with less power by elevation sidelobes previously not present in the linear array. The difference in illumination is more pronounced in the 11 km scenario because of the elevation angle to the range. Referring back to Figures 4.1 and 4.6, the elevation angle to $\phi = 0$ at 66km is $-2.8°$ and to 11km is $-14°$. Figure 4.12 illustrates this concept that the degree of impact on clutter illumination depends on the range. The addition of five (5) elevation channels results in a 12 dB reduction in clutter illumination at 11km, but only a 0.3 dB reduction
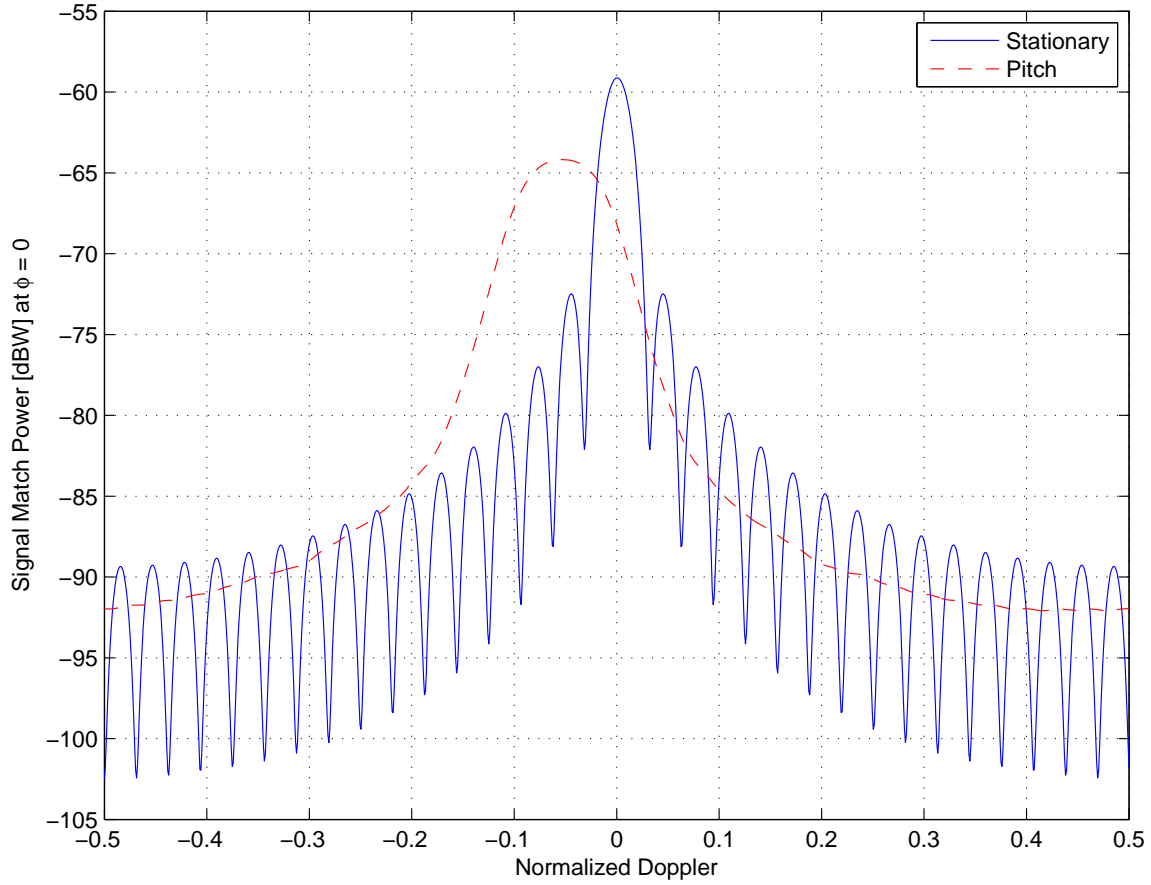
Figure 4.8: SM PSD cut for 120×1 array at $\phi = 0$ for 11 km with pitch. The increased azimuth resolution of the antenna pattern and the change in azimuth associated with pitch at 11 km create the spreading and shift observed.

at 66km. The illustration at 66km is omitted for the insignificant change. The reduction in clutter illumination at 11km translates to a reduction of the clutter power spectrum, as depicted in Figure 4.13. Not surprisingly, the clutter power's significant reduction in the planar array plus the added DOF translate to improved SINR, shown in Figure 4.15. While increasing azimuth channels increased pitch effects, increasing elevation channels decreases pitch effects. The added elevation definition reduces clutter illumination and therefore power, while the target is illuminated constantly in the normalized mainbeam at 22 dB.

A brief recap is needed of pitch effects for linear and planar arrays, including targets at close (11km) and distant (66km) ranges. Pitch effects are insignificant at
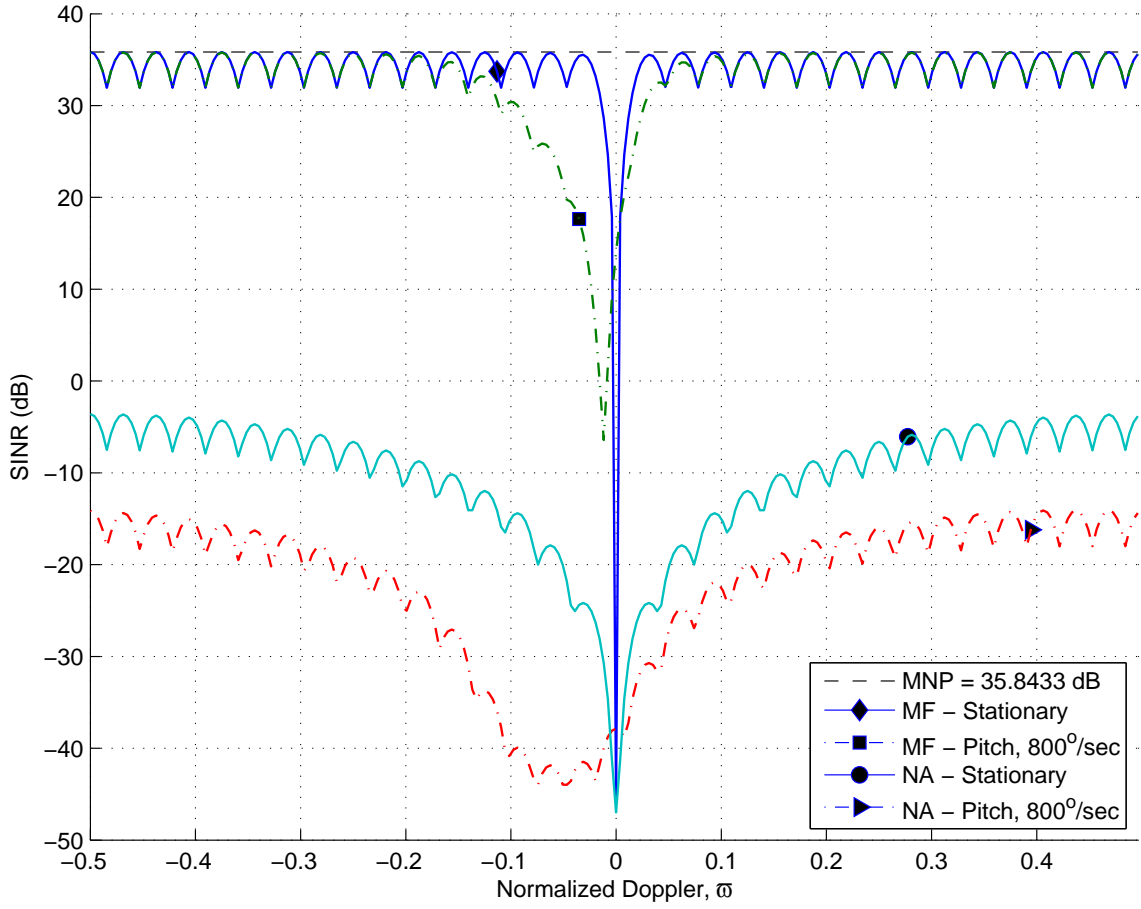
Figure 4.9: Output SINR for 120×1 array with pitch at 11 km. The broadening and larger shift in SM PSD towards negative Doppler is seen in the output SINR. Improvement over NA processing again increased, just as it did at 66km.

distant ranges for the linear array, as long as the array length and resulting azimuthal definition does not approach the corresponding change in azimuth resulting from the pitch rotation. For the simulation parameters used, linear array pitch effects at 66km were minimal until the array length approached 115 elements. The greater the target distance, the greater the number of elements required before pitch causes SINR degradation. Before the number of azimuth channels reaches that threshold number, adding azimuth channels improves performance as if pitch were not present. Adding elevation channels offers marginal improvement for distant targets. The small elevation angles to distant targets, and the very small change in elevation angle pitch induces, requires the addition of many elevation channels to impact the results. For
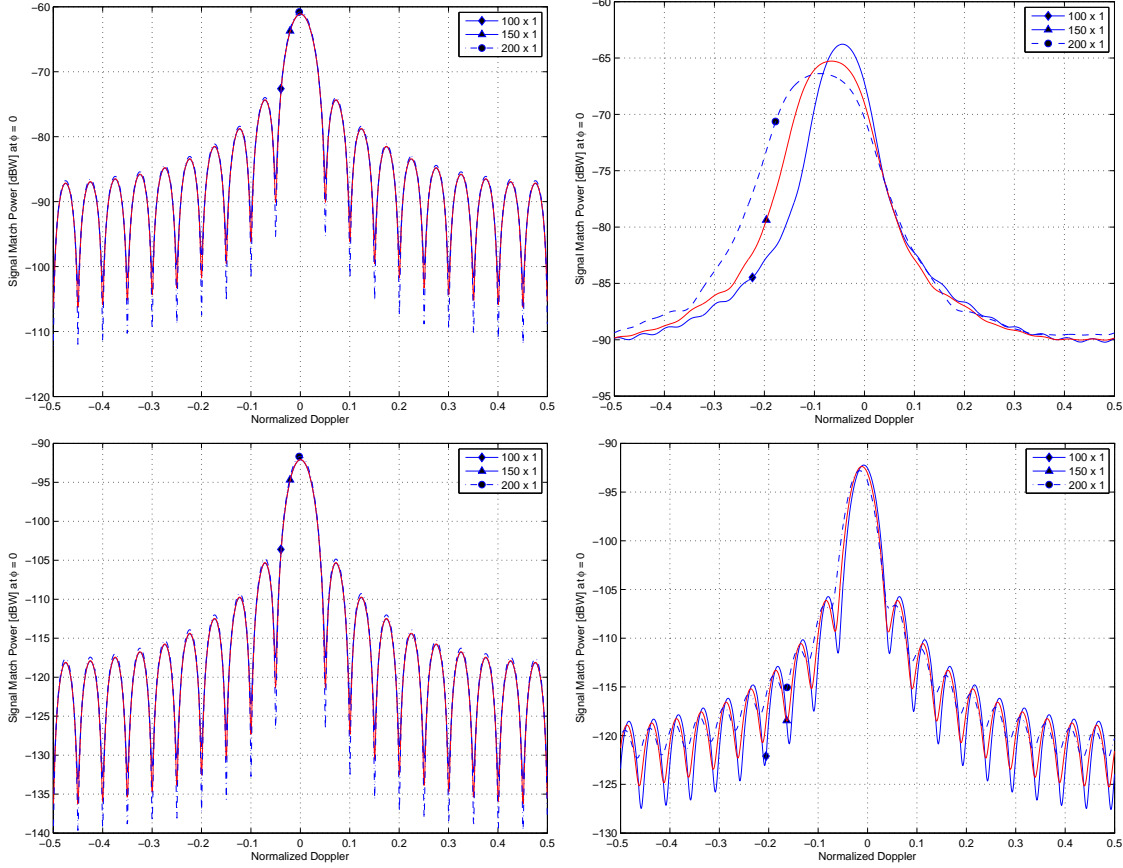
Figure 4.10:   SM PSD cut for linear arrays at $\phi = 0$ for 11 km and 66 km with pitch. The number of pulses in the CPI was reduced to 20, in order to avoid computation memory limits. Top left: SM cut for 11 km without platform maneuver. Top right: SM cut for 11 km with pitch. As the azimuth channels are increased, the resolution of the antenna pattern improves. These improvements in resolution lead to the shift and spread observed. Bottom left: SM cut for 66 km without platform maneuver. Bottom right: SM cut for 66 km with pitch. The antenna pattern resolution is not high enough to produce significant changes in the PSD cut. A slight negative Doppler shift and shortening of the nulls is observed. The nulls would eventually fill and the clutter null shift if more channels were added.

the 120×1 linear array and 66km case, 16 elevation channels are needed to reduced the clutter illumination at $\phi = 0°$ 3 dB. That elevation channel addition increases MNP from 3840 to 61440. The slight reduction in clutter power is heavily trumped by the enormous increase in required processing power, especially when pitch effects are minimal at distant ranges for the parameters simulated.
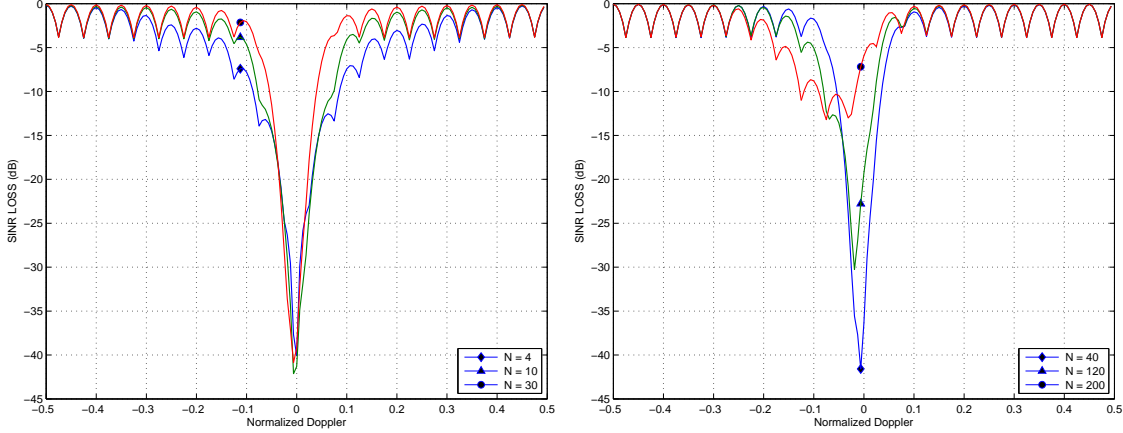
Figure 4.11:   SINR Loss for 11 km with pitch. The number of azimuth channels is varied, while $M = 20$, $P = 1$. In the left plot, the number of channels remains small enough such that the antenna pattern lacks enough resolution for pitch effects to be seen. As the number of channels increases, the null narrows as would be expected if pitch were not involved. In the right plot, the number of channel is high enough such that pitch effects are observed. The null shifts and widens due to the increased azimuth resolution and resulting PSD shift and spread.
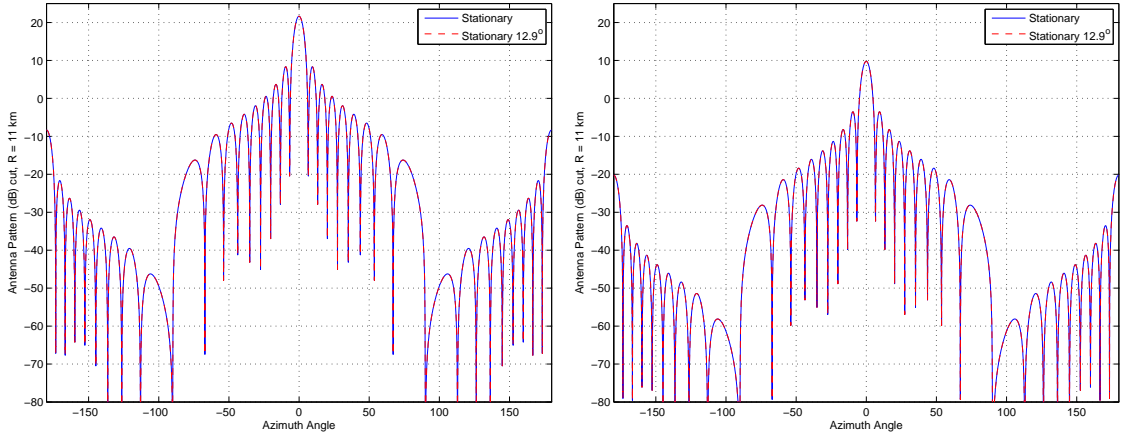
Figure 4.12:   Antenna pattern azimuthal cut at 11 km and 12.86° pitch. The addition of five (5) elevation channels results in a significant reduction in clutter illumination at 11 km. The added elevation definition placed the clutter at 11 km in previously non-existent sidelobes. The left plot is an azimuth cut for a 20×1 array, showing a clutter illumination at $\phi = 0$ of 22dB. The right plot is an azimuth cut for a 20×5 array, showing a clutter illumination at $\phi = 0$ of 10dB.

Linear array pitch effects are very significant at close ranges. Pitch rotation changes the azimuth angles to clutter patches more quickly at close ranges than distant ranges. Multiple antenna pattern lobes illuminate each clutter patch, resulting

91
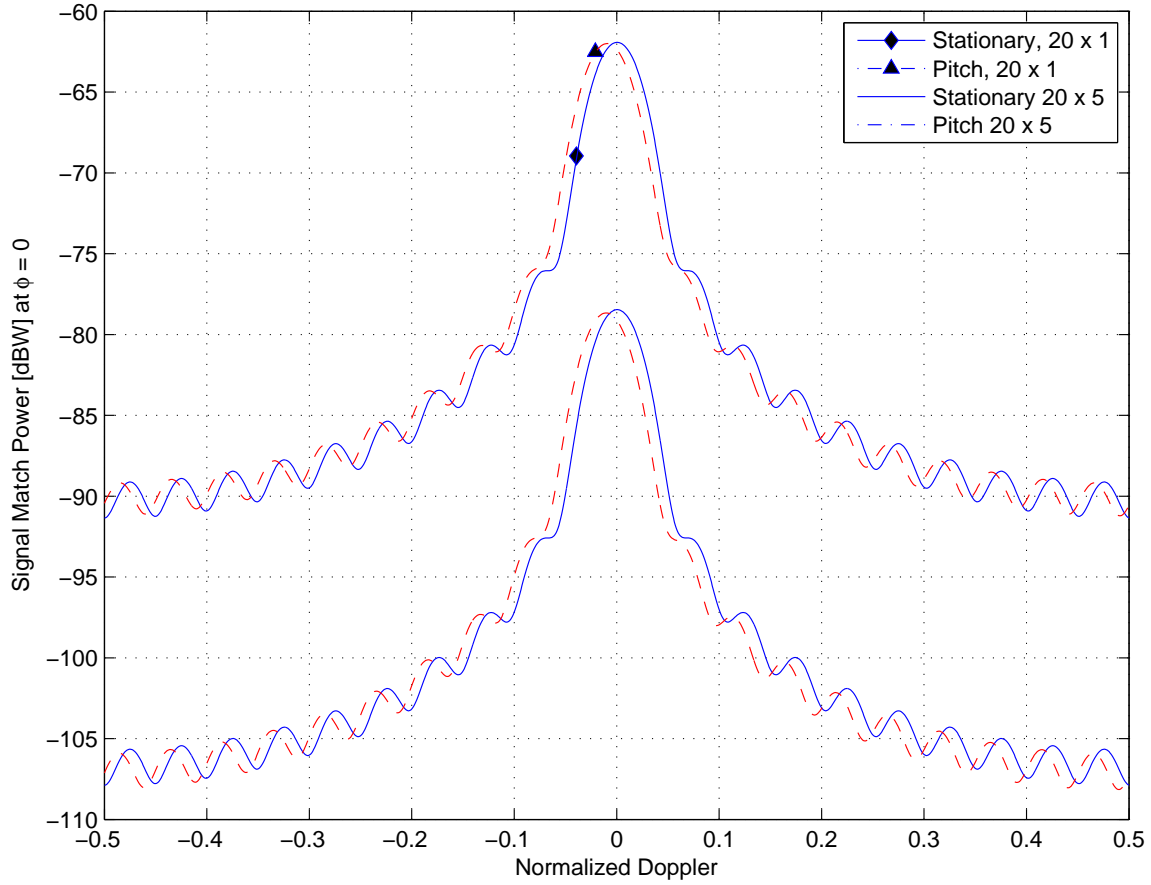
Figure 4.13: The addition of five (5) elevation channels places clutter at 11km in elevation sidelobes not present in the linear array. The net result is a significant reduction in clutter power. The reduction is not observed at 66km due to the small elevation angle to that range.

in a broad Doppler spread and shift. The broadness of the shift is proportional to the azimuth resolution (and hence number of azimuth channels) in the array. The addition of elevation channels significantly improves performance at close ranges due to the reduction of clutter illumination and constant target illumination. Compared to the distant target scenario, fewer elevation channels result in significant clutter reduction.

Pitch effects for the linear and planar array, at 11 km and 66 km, were addressed in this section. Platform roll is investigated next.
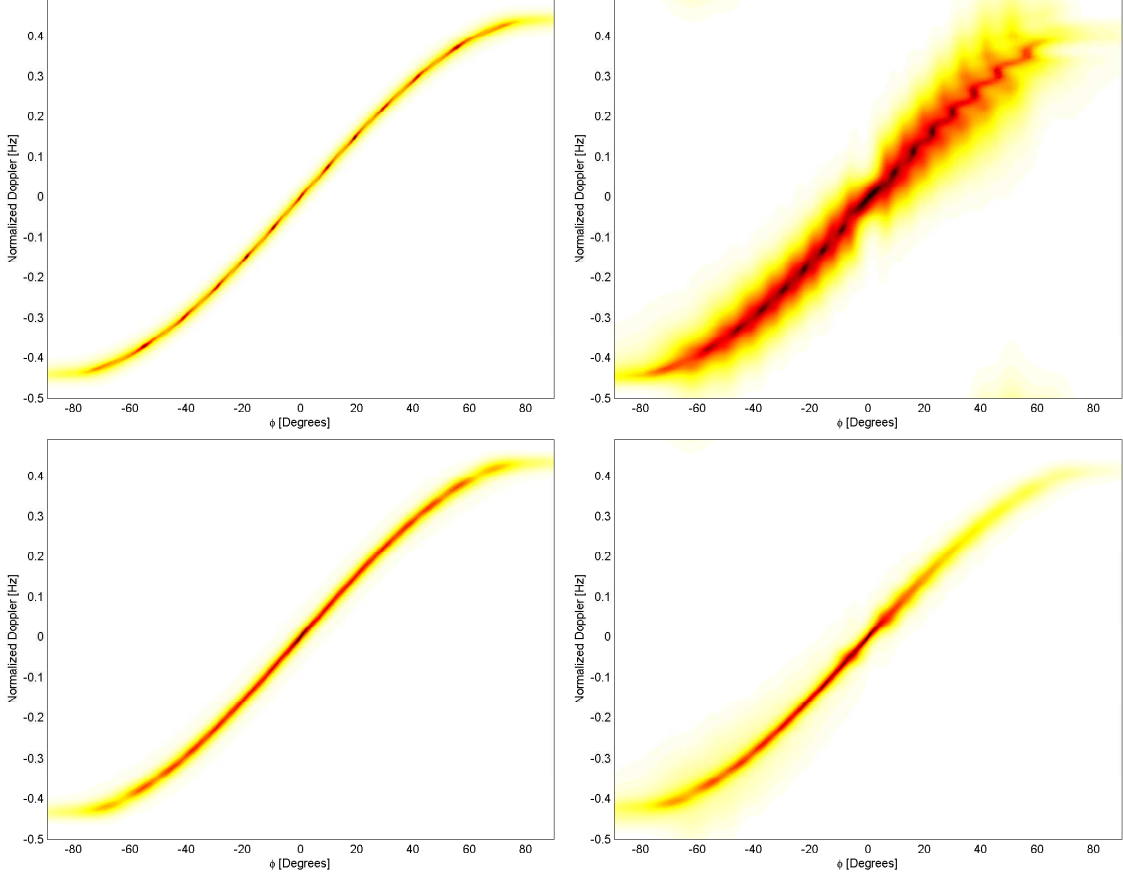
Figure 4.14:   MVE for 20×1 and 20×5 arrays with and without pitch at 11 km. The addition of elevation channels with pitch impacts the clutter spectrum. The top plots show the MVE for a 20×1 planar array without (left) and with (right) pitch at 11km. The bottom plots show the MVE for the 20×5 array with (right) and without (right) pitch. Less spreading occurs in the 20×5 case.

4.3   Roll effects

Platform roll corresponds to rotation about the x-axis. The antenna is steered to boresight, where the target is located at the start of the CPI. In the roll scenario, the target is not always located at boresight due the platform maneuver. Therefore, the target is not constantly illuminated ($\boldsymbol{\xi}_t \neq \mathbf{1}_M$). Roll effects will therefore be due to changes in both target and clutter illumination.

4.3.1   Linear Array with Target at 11 km and 66 km.   First consider a target at 66km. Roll changes in the azimuth and elevation angles to the location $\phi = 0$
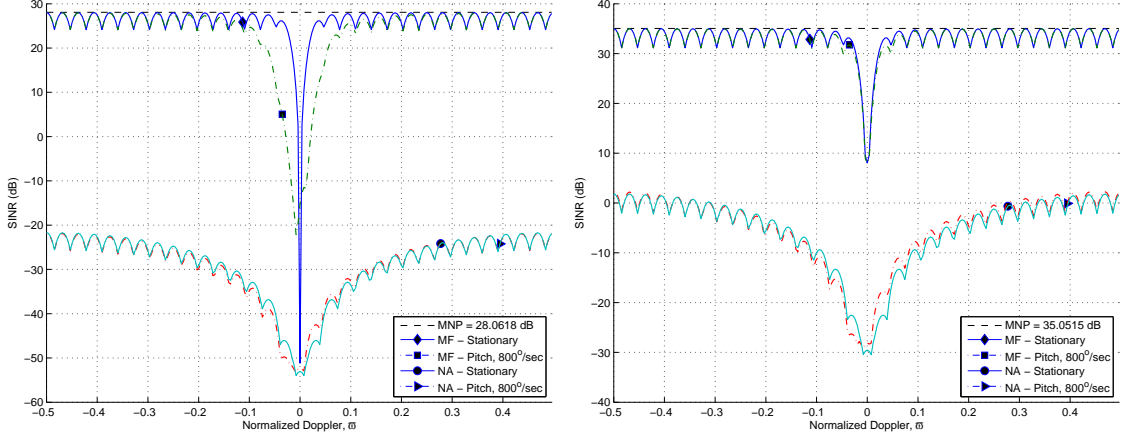
Figure 4.15:   Output SINR for 20×1 and 20×5 array with pitch. The addition of five (5) elevation channels greatly improves SINR and narrows the clutter null to near stationary MF performance. The left plot shows output SINR for a 20×1 array for 11km. The pitch causes a widening of the clutter null around zero Doppler. The right plot shows output SINR for a 20×5 array at 11km. The null narrows and shortens due to decreased clutter illumination caused by the elevation definition added and added DOF.
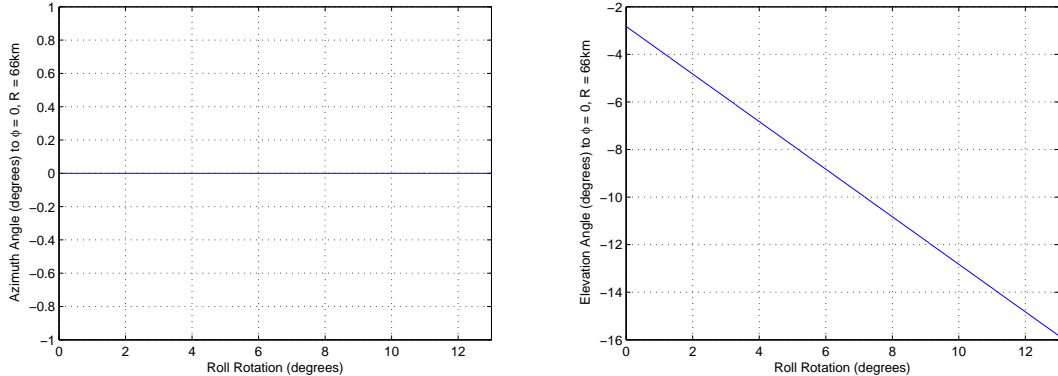
Figure 4.16:   A $12.86°$ roll rotation results in no change in azimuth angle and $-12.86°$ change in elevation angle to the location $\phi = 0$ at a range of 66km.

at 66km are depicted in Figure 4.16. Notice a $12.86°$ roll rotation corresponds to no change in azimuth and an one-for-one change in elevation of $-12.86°$ for $\phi = 0$. Significant SINR impact is therefore expected only if the array pattern's *elevation* definition changes considerably over that $12.86°$ span. In the case of the linear array, the pattern lacks elevation definition. The poor elevation definition leads to little difference in clutter illumination in both the roll right and roll left scenarios, as

94
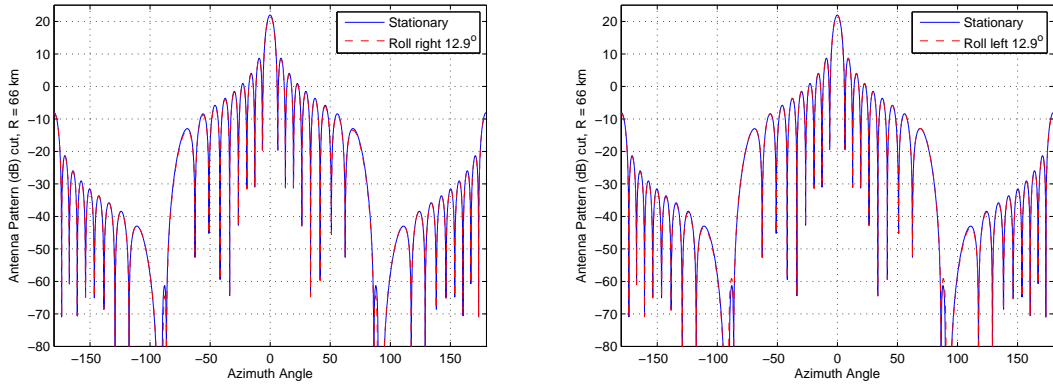
Figure 4.17: Antenna pattern azimuthal cuts at 66 km and 12.86° roll. On the left, an azimuth cut for the roll right scenario shows no difference than the roll left scenario (right). The lack of elevation definition in the linear array causes the lack of illumination difference.

depicted in Figure 4.17. In the case of roll right, the mainbeam is rolling skyward away from the ground. In the roll left scenario, the mainbeam is rolling downward toward the ground. A slight change of -0.45 dB in target illumination occurs due to roll in either direction. With little change in clutter or target illumination at 66 km, roll has an insignificant impact on the clutter spectra and output SINR as shown Figure 4.18. Adding azimuth channels narrows the clutter null and improves SINR, as depicted in Figure 4.19. The clutter null narrows and SINR loss decreases as the number of azimuth channels is increased.

Summarizing roll effects on the linear array, at both 11km and 66km the lack of antenna pattern elevation definition results in insignificant changes in target and clutter illumination. These minor differences translate to minor differences in the clutter spectrum and output SINR. The addition of azimuth channels improves SINR and narrows the clutter null.

4.3.2 Planar Array with Target at 11 km and 66 km. In the linear array, the direction of role was of no consequence due to the lack of elevation definition in the antenna pattern. The addition of elevation channels makes the direction of roll important. In the roll right scenario, the mainbeam rolls skyward away from the

95
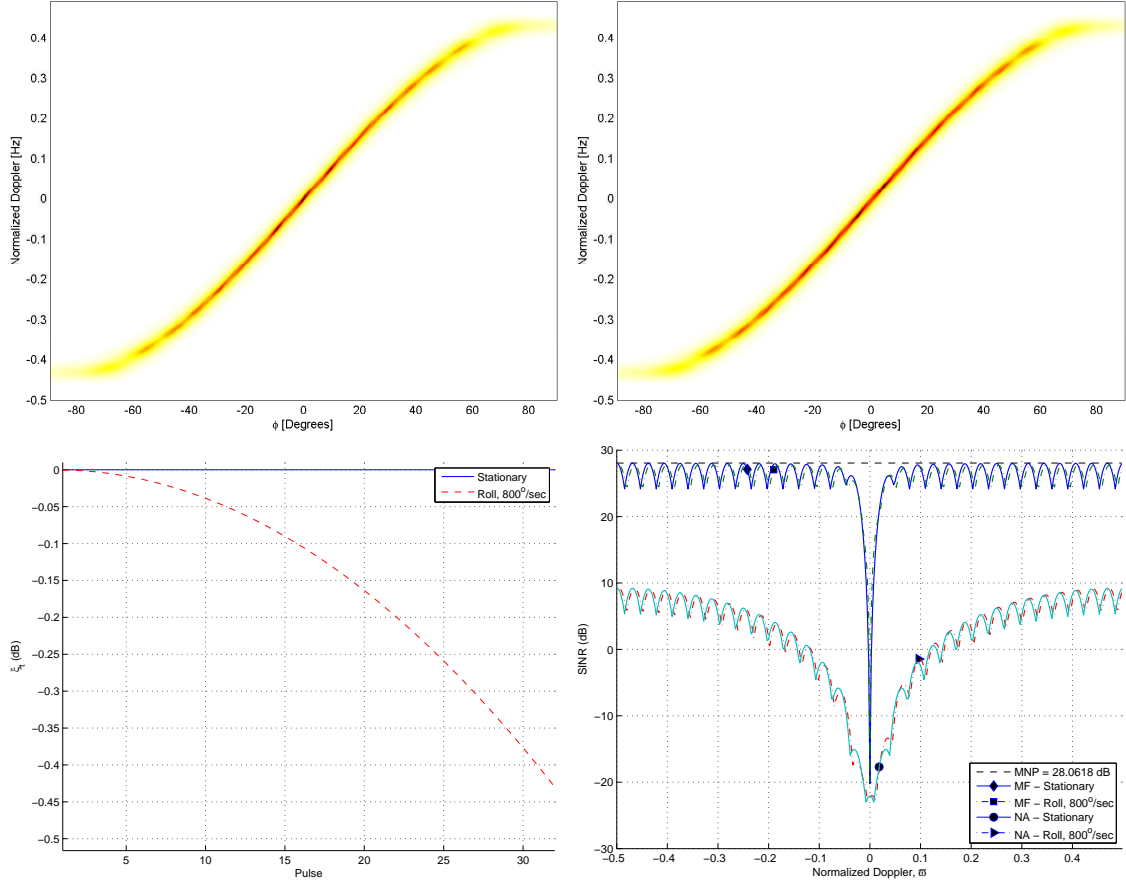
Figure 4.18: MVE, SNR, SINR for 20×1 array at 66 km with roll. The top left figure is the MVE for the stationary platform. The top right figure is the MVE with roll, showing no discernable difference from the stationary case. The SNR is depicted in the bottom left figure, illustrating just a −0.45 dB change in target illumination. The little change in clutter spectrum coupled with the small change in target illumination results in minimal change in the output SINR, shown in the bottom right figure.

clutter and illuminates the clutter with more sidelobes. In the roll left scenario, the mainbeam actually rolls towards the clutter and illuminates more clutter with the mainbeam. The net result is two very different clutter spectrums, depicted in Figure 4.20. Roll left yields a 14dB increase in clutter power because the mainbeam rotates toward the ground, while the roll right yields a 10dB decrease because the mainbeam rotates skyward. The target illumination also undergoes drastic changes compared to the linear case, depicted in Figure 4.21. However, these dramatic differences in clutter spectra do not translate to differences in output SINR depicted in Figure 4.22.
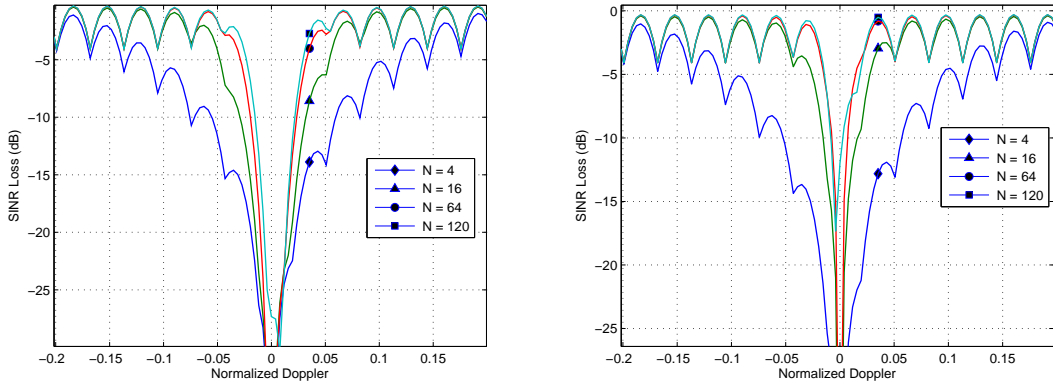
Figure 4.19:　　SINR loss and at 11 km and 66 km with roll. The clutter null narrows and SINR loss decreases as the number of azimuth channel is increased in both the 11 km (left) and 66 km (right) scenario.

Despite a 22dB difference in clutter spectra, output SINR appears identical. The result is attributable to the high number of MF DOF, and the fact that the clutter spectrum did not shift in Doppler.

Next, the relationship between increasing elevation channels and roll effects is considered. In the linear array, adding azimuth channels narrowed the clutter null. However, the addition of elevation channels has the opposite effect. The SINR loss plot in Figure 4.23 shows a widening null and increasing loss and the number of elevation channels increase.

Roll effects are minimal for the linear array, at all ranges, due to the lack of elevation definition in the antenna pattern. The array remains in its original place throughout the CPI, and the change in clutter and target illumination is minute. The addition of elevation channels enhances roll effects.

4.4　Yaw Effects

Platform yaw corresponds to rotation about the z-axis. The antenna is steered to boresight, where the target is located at the start of the CPI. In the yaw scenario, the target is not always located at boresight due the platform maneuver. Therefore, the target is not constantly illuminated ($\boldsymbol{\xi}_t \neq \mathbf{1}_M$).

97
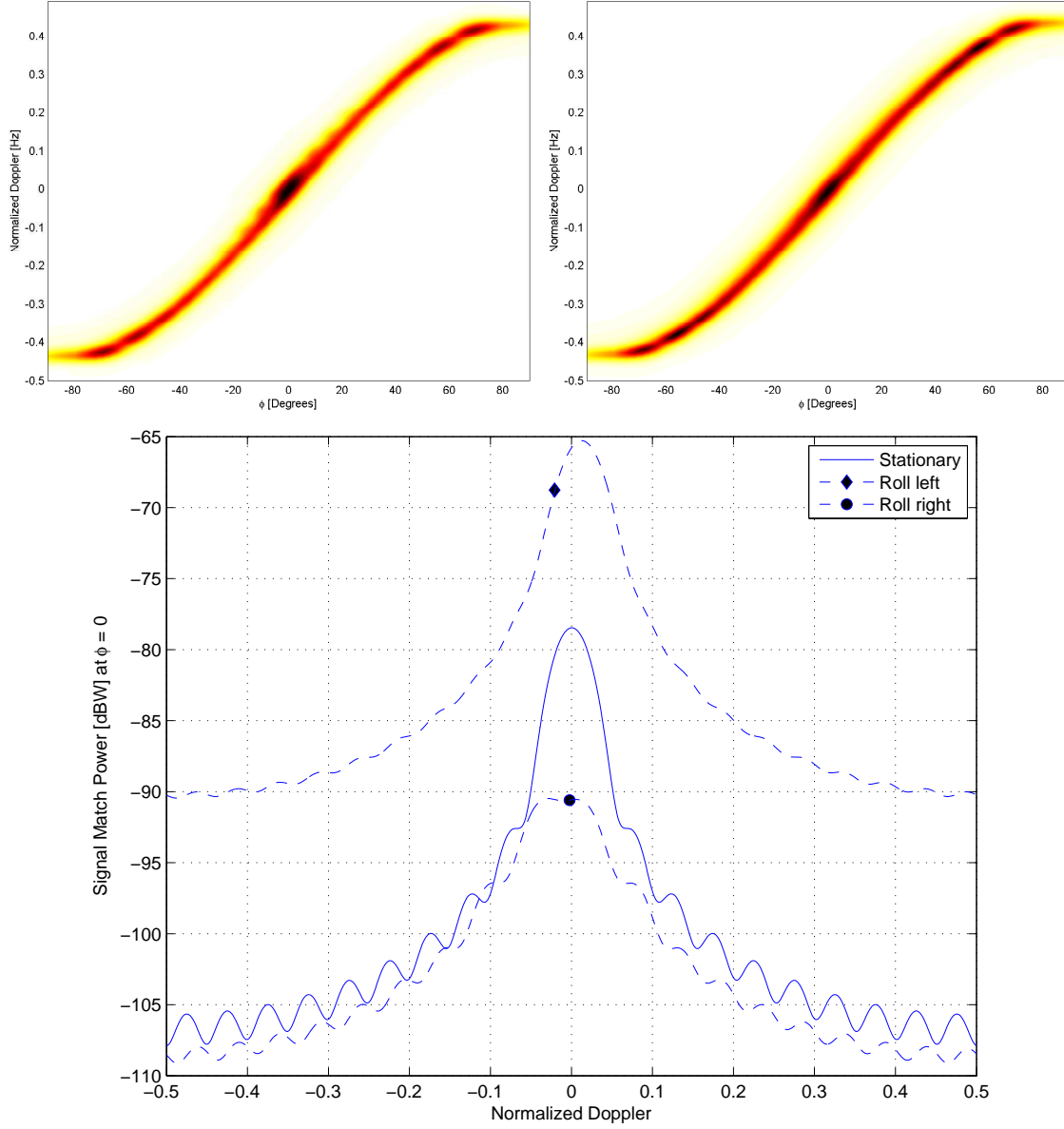
Figure 4.20:   MVE and SM cut for planar arrays with and without roll. The addition of elevation channels with roll impacts the clutter spectrum at both 11km and 66km. The top plots show the MVE for a 20×5 planar array with roll left (left) and roll right (right) at 11km. A broadening in Doppler is observed in both cases, but no magnitude information can be taken from MVE. The bottom plot shows the SM PSD cuts at zero azimuth for roll right, roll left, and stationary. Roll left yields a 14dB increase in clutter power because the mainbeam rotates toward the ground, while the roll right yields a 10dB decrease.

4.4.1   Linear Array with Target at 11 km and 66 km.   Yaw changes in the azimuth and elevation angles to the location $\phi = 0$ at 66km are depicted in Figure
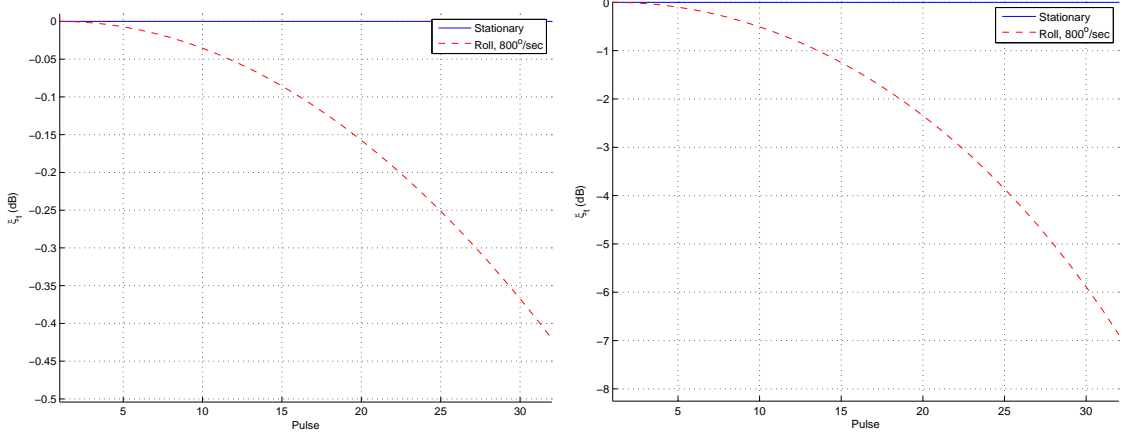
Figure 4.21:   Signal-to-Noise ratio for linear and planar array and target at 11km with roll. The poor elevation definition of the 20×1 linear array (left) yields little change in target illumination despite $12.86°$ of roll. The addition of five (5) elevation channels (right) increases elevation definition and yields a -7dB swing in target illumination.
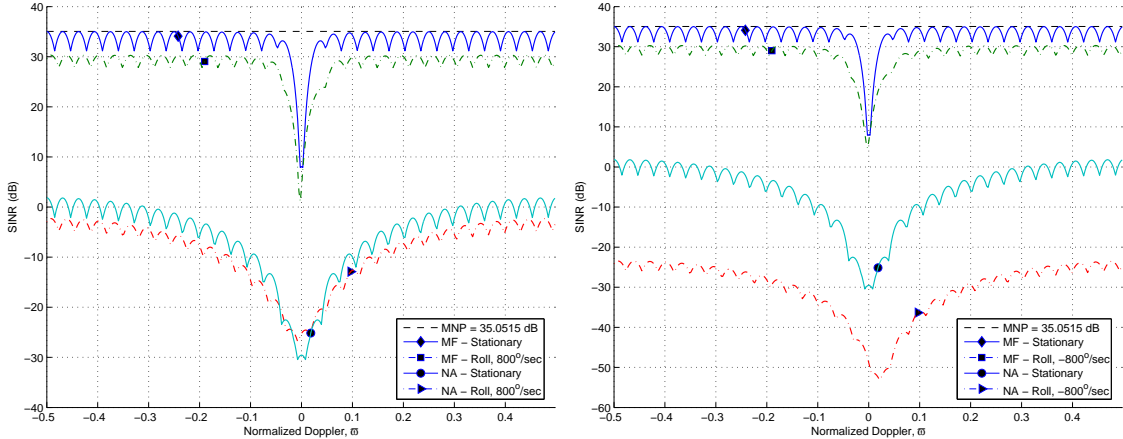

Figure 4.22:   SINR for 20×5 planar array with roll at 11 km. Left: roll right. Right: roll left. The increased clutter power is evident in the roll left plot in the large drop in NA performance. However, the MF overcomes the increase in clutter with $MNP = 3200$ DOF.

4.24.   Notice a $12.86°$ yaw rotation corresponds to no change in elevation and an one-for-one change in azimuth of $-12.86°$ for $\phi = 0$. This relationship is the same for 11km and 66km. Significant SINR impact is therefore expected if the array pattern's *azimuth* definition changes considerably over that $12.86°$ span. In the case of the linear array, the pattern has significant azimuth definition for any realistic array length. The azimuth definition leads to significant differences in the clutter illumination for both

99
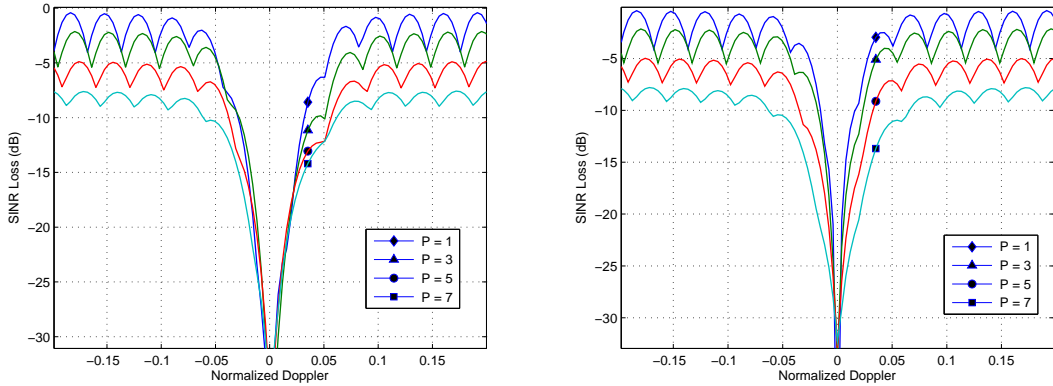
Figure 4.23: SINR loss varying elevation channels with roll. The left plot shows SINR loss for the 11 km scenario and increasing elevation channels and the left plot shows the same for 66 km. In both cases, the loss and null width increase as P increases. $N = 20$ for all plots.
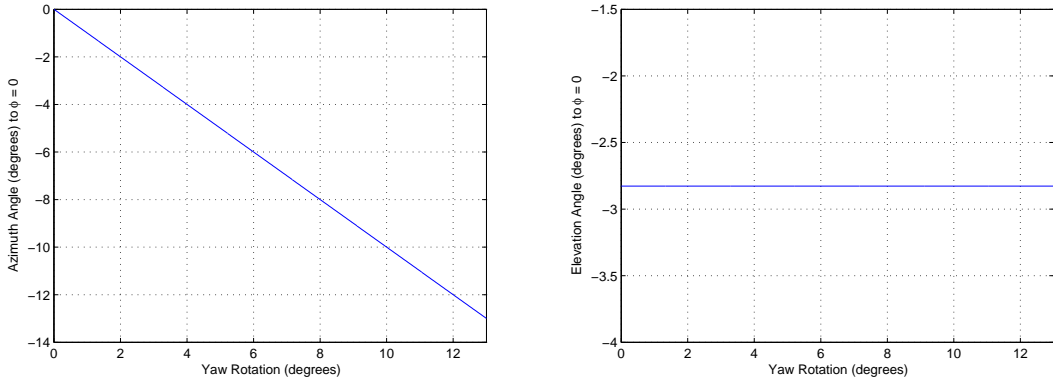

Figure 4.24: A 12.86° yaw rotation results in no change in elevation angle and $-12.86°$ change in azimuth angle to the location $\phi = 0$ at both 11km and 66km.

11km and 66km, as shown in Figure 4.25. This same azimuth definition leads to significant differences in the clutter spectrum for both 11km and 66km, as shown in Figure 4.26. Smearing in both azimuth and Doppler is apparent in Figures 4.26. However, the SM PSD cut does not look drastically changed from the stationary case. As the platform yaws clockwise (CW) about the z-axis, the mainbeam and antenna pattern rotates as well. The velocity vector and consequently the Doppler of each ik^{th} patch changes. However, the overall magnitude of Doppler illumination remains relatively unchanged. In the stationary case, the patch at $\phi = 0$ had a

100
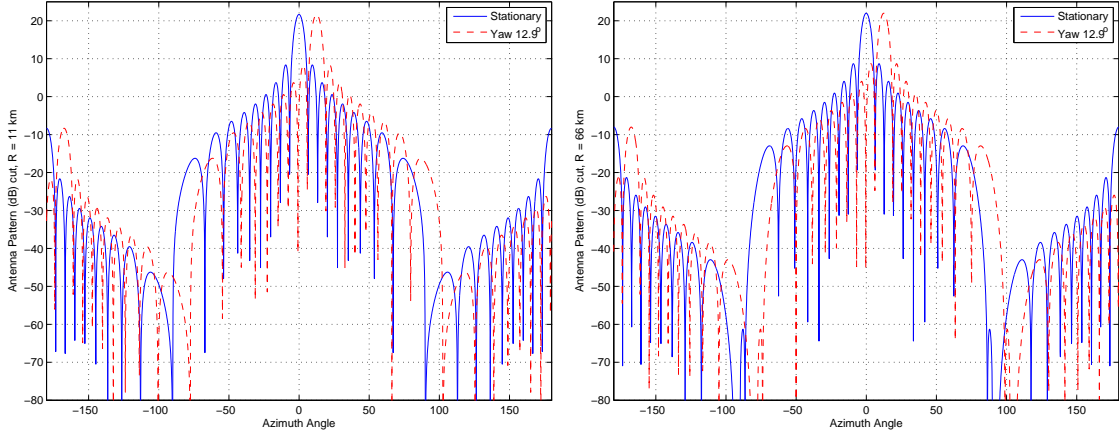
Figure 4.25: Antenna pattern azimuthal cuts for 20×1 at 11 and 66 km with yaw. Yaw rotation about the z-axis produces a one-for-one change in azimuth angle. A 12.86° rotation corresponds to nearly two lobes (mainbeam plus sidelobe) of the pattern.

Doppler frequency of zero and was at boresight throughout the CPI. Now assume the platform yawed 1°. That same patch is no longer at at boresight nor is its Doppler frequency zero. However, the patch previously at $\phi = 1°$ is now at boresight and its Doppler frequency is zero. When the platforms yaws 2°, the patch previously at 2° and non-zero Doppler is now at boresight and zero Doppler. The radar is "looking" at its boresight throughout the CPI, and that view is not drastically changing. However, a yaw has an enormous impact on target illumination, depicted in Figure 4.27. The 12.86° yaw puts the target though the first antenna pattern null and halfway into the second null. The target is nearly begin "yawed" out of the picture. The result is a significant degradation in output SINR, shown in Figure 4.28 for both 11 km and 66 km. If the number of azimuth channels is increased, the antenna pattern beamwidth decreases and the target illumination change becomes more pronounced. The SINR loss plot in Figure 4.29 shows loss proportional to the number of azimuth channels N. The larger N becomes, the close the radar gets to "yawing" the target out of the picture.

4.4.2 Planar Array with Target at 11 km and 66 km. The addition of elevation elements once again changes the way the clutter is illuminated. The resulting
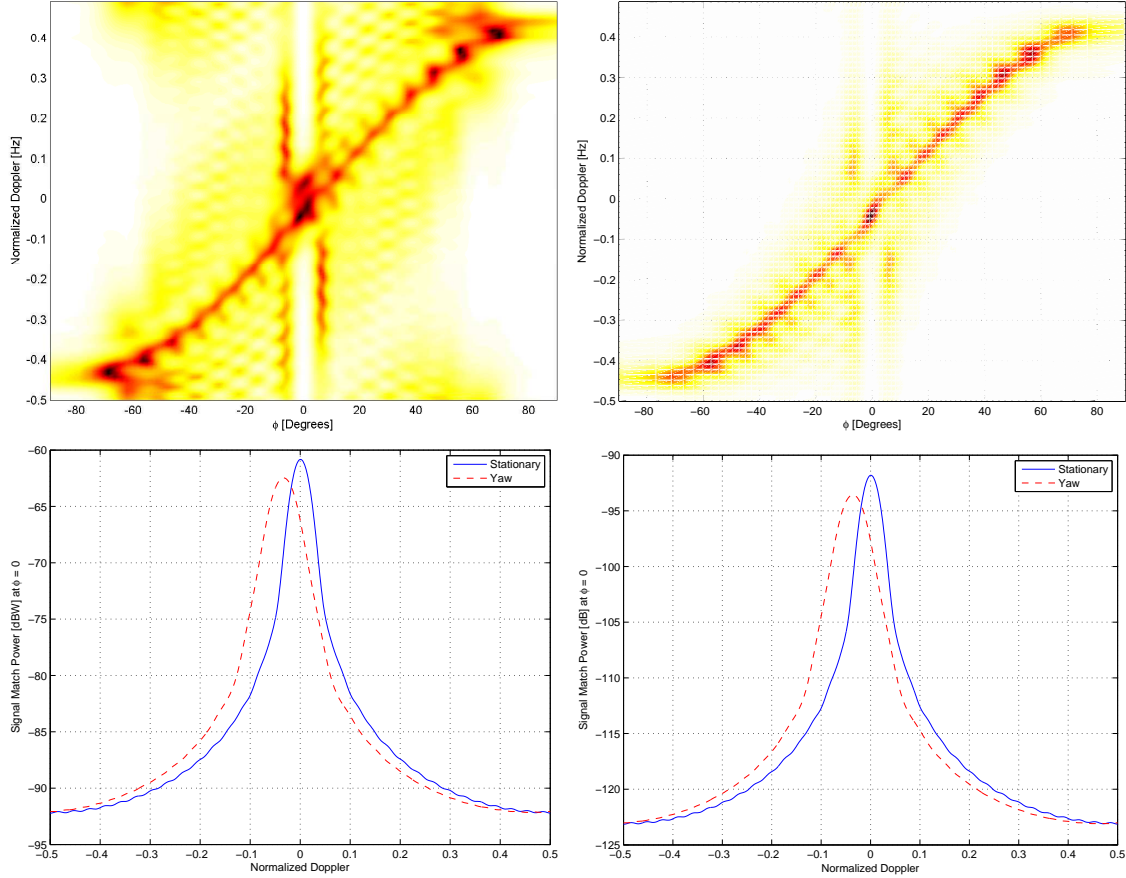
Figure 4.26: Clutter spectrum for 20×1 arrays with and without yaw at 11 km and 66 km. The top plots show the MVE for 11 km (left) and 66 km (right) with yaw. These plots show extreme spread in Doppler and azimuth. The bottom plots show the SM PSD cut at zero azimuth for 11 km (left) and 66 km (right). Unlike the MVE, drastic differences are not seen in the SM cut.

clutter spectrum are depicted for the 20×5 array at 11 km and 66 km in Figure 4.30. Target illumination is shown in Figure 4.31. The addition of elevation channels does not impact the target illumination, as the target illumination depends only on the azimuthal definition due to yaw being a rotation about the z-axis. However, the target illumination remains drastically reduced compared to the stationary case. As the number of elevation channels is increased, the added DOF and reduction in clutter illumination do not overcome the drastic reduction in target illumination. Some improvement is observed however at the 11 km range, as the change in clutter illumination impacts performance more so than at 66 km. Figure 4.32 shows the
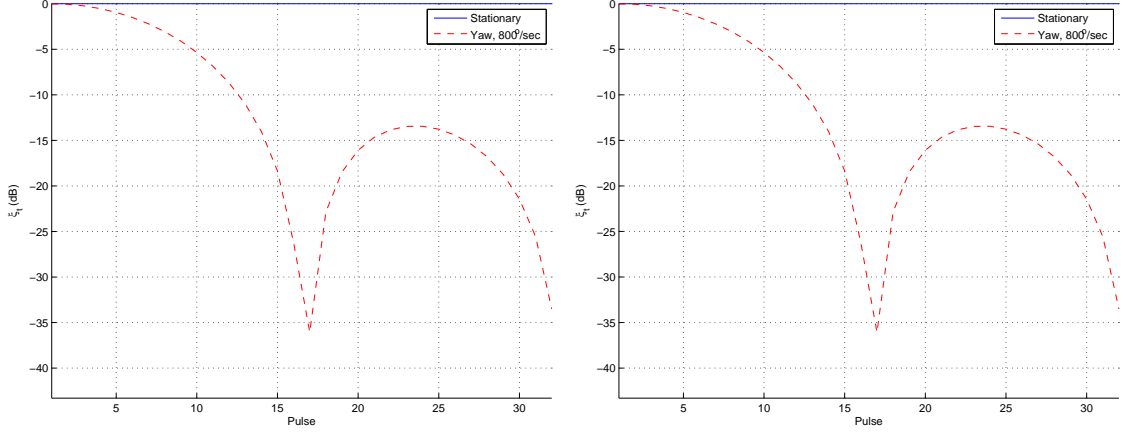
Figure 4.27: SNR for 20×1 array with yaw at 11 km and 66 km. The yaw induces major changes in target illumination in both the 11 km (left) and 66 km (right) scenarios. The target is illuminated nearly 6 dB less only a third of the way through the CPI. By the halfway point of the CPI, the difference is 30 dB down. The 12.86° yaw puts the target though the first antenna pattern null and halfway into the second null.
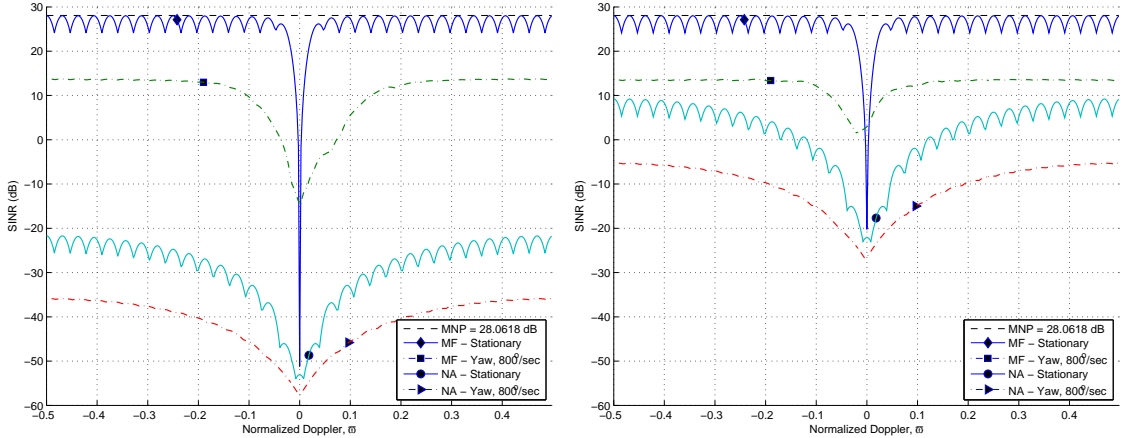

Figure 4.28: Output SINR for 20×1 array with pitch at 11 km and 66 km. The vast reduction in target illumination results in significant impact on SINR for both the 11 km (left) and 66 km (right) scenario.

SINR loss for varying elevation channels. In the 11 km scenario, a slight narrowing of the clutter null is observed and loss is inversely proportional to P. It is noted however that the SINR loss maximum is -12dB, despite the narrowing null. While the decrease in clutter illumination lessens the degradation caused by yaw, the hit it target illumination can not be overcome. In the 66 km case, adding elevation channels does not effect the null width or loss. Physically, the 66 km range is farther away

103
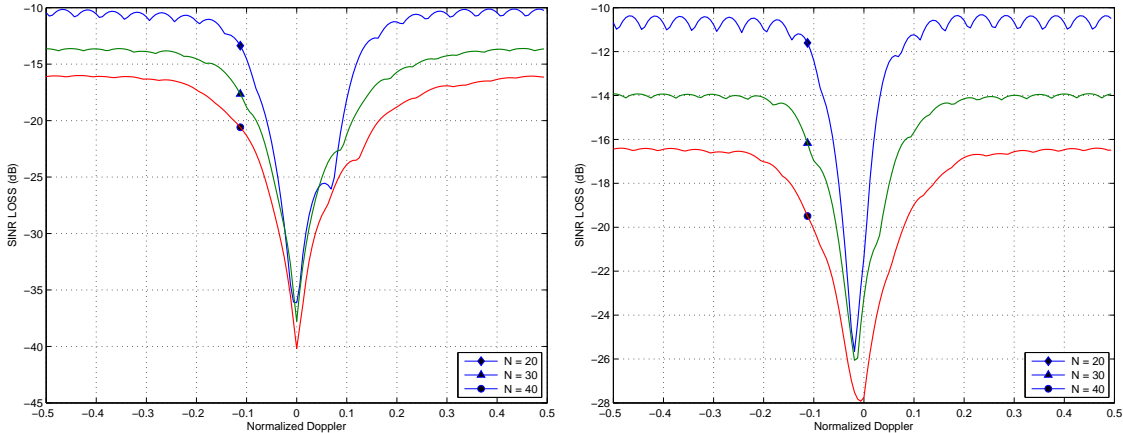
Figure 4.29: SINR loss at 11 and 66 km with roll. Severe loss is observed at both range, 11 km (left) and 66 km (right). The beamwidth associated with these values of N is small enough such that the target illumination is drastically reduced.

where the added elevation channels do not effect the clutter illumination. The result is again limited by the decreased target illumination.

Overall, yaw is by far the most devastating maneuver effect, at short and long ranges. The main culprit is drastically lower power with which the target is illuminated. The addition of elevation channel is ineffective at mitigating the impact. Pitch contributions are limited unless the number of azimuth channels produce a beamwidth on the order of the change in azimuth and elevation to a range. The number of azimuth channels needed is proportional to the range of interest. The addition of elevation channel mitigated pitch effects. Roll effects were negligible for the linear array due to lack of elevation definition. Adding azimuth channels to the linear array improved performance. The addition of elevation channels enhanced roll effects, as the added elevation definition resulted in fluctuations in target and clutter illumination not seen with the linear array.

4.5 Maneuver Effects on Sample Support Homogeneity

The statistical clutter environment is rarely, if ever, known *a priori* and must be estimated based on snapshots from range cells other than the RUT. An accurate estimate relies upon homogeneous, independent-identically distributed (iid) sample
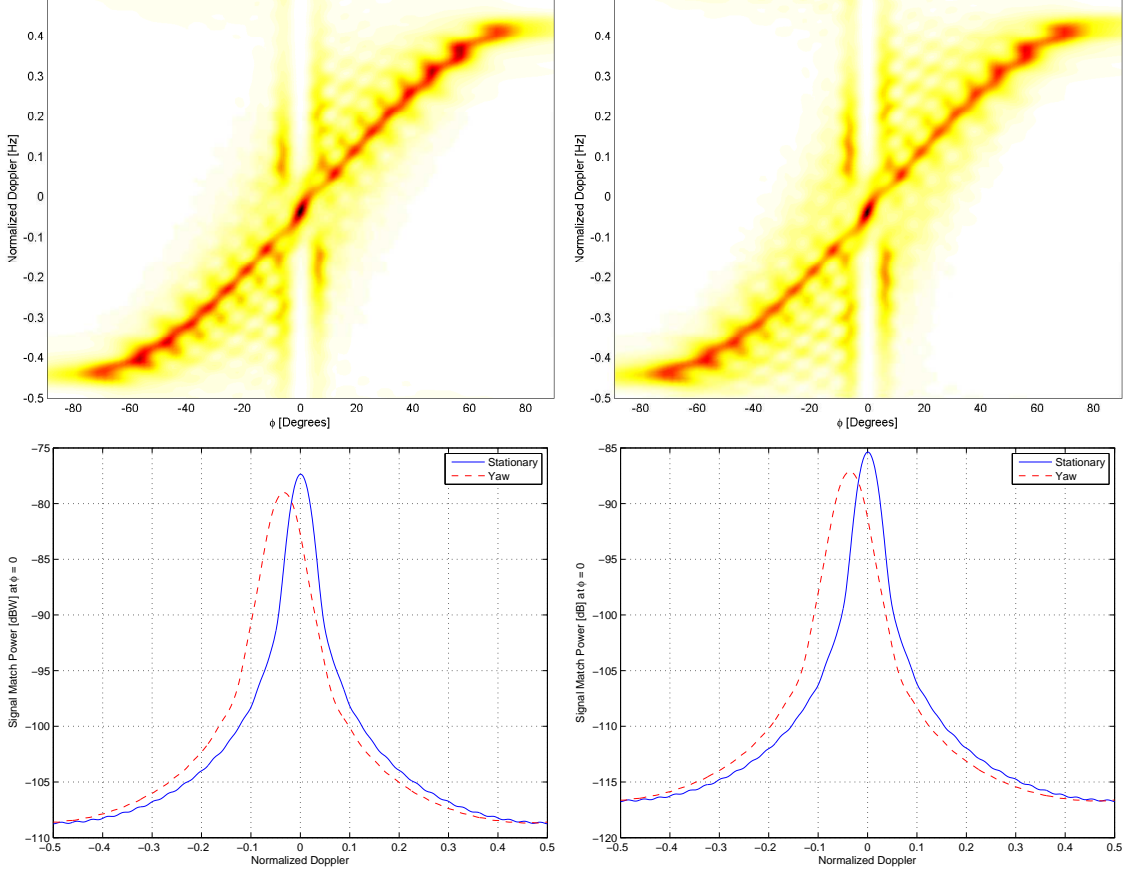
Figure 4.30:   MVE for 20×5 arrays with and without yaw at 11 km and 66 km. The MVE for 11 km in the top right plot shows severe smearing in azimuth and Doppler. Similar smearing is seen in the MVE at 66 km (top right). The SM cuts at 11 km (bottom right) and 66 km (bottom left) show a shift towards negative Doppler.

support vectors. For this research, the generalized inner-product [11],

$$\text{GIP}_{\text{k}} = \boldsymbol{\chi}_{\text{k}}^{H} \mathbf{R}_{\text{RUT}} \boldsymbol{\chi}_{\text{k}}. \tag{4.15}$$

is used to access maneuver induced heterogeneities in sample support data. Using the known covariance of the RUT, the GIP compares the magnitude and phase of snapshots at surrounding range cells. The larger the GIP variance and range across a set of sample support vectors, the greater the non-homogeneity. The key physical insight into what the GIP does is that it measures the statistical "likeness" of the RUT
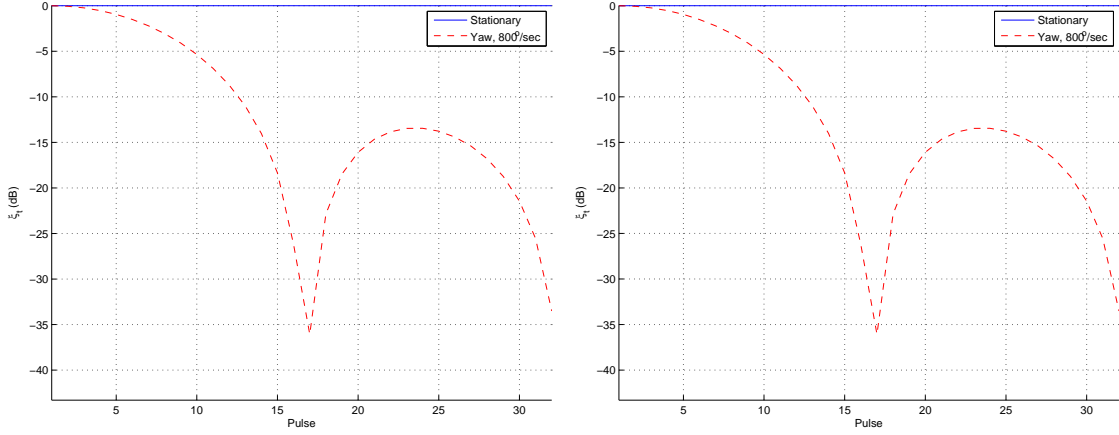
Figure 4.31:   SNR for 20×5 array with yaw at 11 km and 66 km. The addition of elevation does not impact the major changes in target illumination in both the 11 km (left) and 66 km (right) scenarios. The target is illumination nearly 6 dB down only a third of the way through the CPI. By the halfway point of the CPI, the difference is 30 dB down. The 12.86° yaw puts the target though the first antenna pattern null and halfway into the second null.
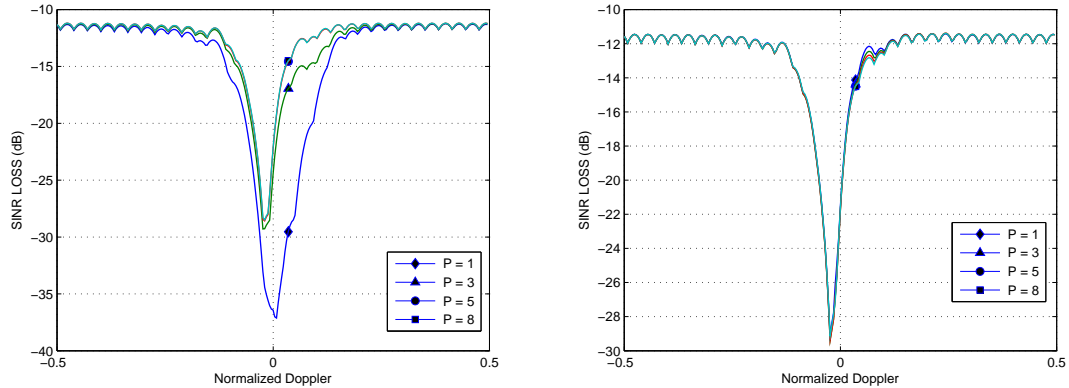

Figure 4.32:   SINR loss varying elevation channels at 11 and 66 km with yaw. At 11 km (left), a slight narrowing of the clutter null is observed and loss is inversely proportional to P. The SINR loss maximum is -12dB, despite the narrowing null. While the decrease in clutter illumination lessens the degradation caused by yaw at 11 km, the hit it target illumination can not be overcome. At 66 km (right), adding elevation channels does not effect the null width or loss. Physically, the 66 km range is farther away where the added elevation channels does not effect the clutter illumination. The result is again limited by the decreased target illumination.

with other range cells. The more statistically alike they are, the more homogenous that sample support vector is.
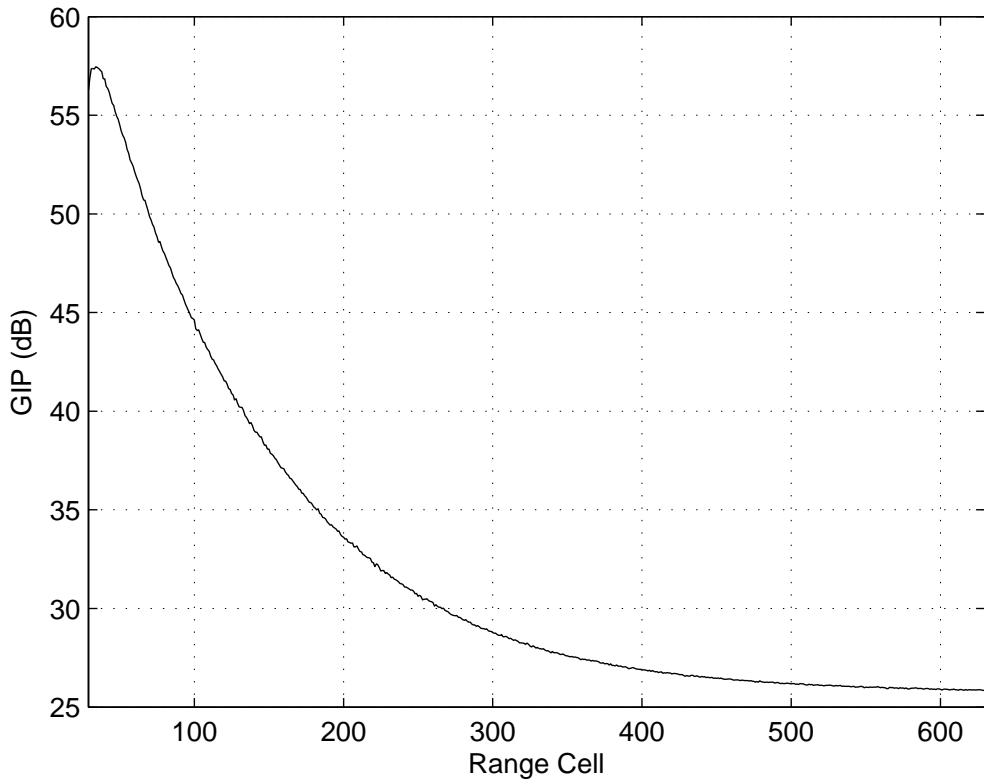
Figure 4.33:   GIP for 20×1, known covariance at 66 km and no maneuver. The CPI length is 20 pulses. Note the value at the RUT (550) is 26 dB, corresponding to the dB value of MNP. A total of 338 range cells are within 3dB of the RUT.

Sample support homogeneity is examined for a 20×1 linear and 20×4 planar array. Recalling the sample support discussion from Chapter II, Factored-Time Space (FTS) requires $2N$ i.i.d. sample support vectors and Joint-Domain-Localized (JDL) requires $2\eta_a\eta_b\eta_e$ to achieve within 3dB of known covariance [2]. FTS therefore requires 40 i.i.d. sample support vectors. Note, the terminology "3dB of known covariance" means known FTS and JDL covariance. JDL may be performed with fewer DOF, but is not assigned a minimum requirement in this exercise. As the maneuver induced heterogeneities are accessed, these i.i.d. sample support requirements are kept in mind. First, the GIP results for the homogeneous cases are examined. The CPI is shorted to 20 pulses for all GIP simulations in the interest of computational loads. In Figure 4.34, the RUT is range cell 550 at 66 km. The GIP value at the RUT

is 26dB, corresponding to the dB value of MNP. In general, the farther away a range cell is from the RUT, the less statistically alike the two are and the larger the GIP. From a physical standpoint, the range cells at close ranges are under much higher illumination and the phase of snapshots at close ranges differ greatly from the RUT. Figure 4.34 illustrates this concept nicely. No published work exists stating a quantitative maximum GIP that equates to the sample support vectors under that maximum are "homogeneous enough" to meet the i.i.d. assumption. The focus of this research is not determining which range cells are intelligent choices for sample support. Instead, the focus is what effects does platform maneuver have on the sample support homogeneity. For comparisons between range cells, a 3dB threshold is used in this research. In the stationary case of Figure 4.34, a total of 338 range cells (from number 292 and higher) are within 3dB of the RUT. Sufficient homogeneous sample support is therefore available for both FTS and JDL.

Range cell 292 is 30.9km from the RUT. The likelihood of range cells of a statistically "alike" nature existing at ranges farther away than that is extremely low. The swath of range cells investigated is therefore limited to number 292 and higher. The addition of platform maneuver is shown in Figure **??**. The addition of roll had minimal effect on the GIP. All 338 range cells within 3dB of the RUT remain under 3dB. However, pitch reduced that number to 271 and yaw reduced it to 278. Overall, maneuver effects on sample support homogeneity is not dramatic. The worst case (pitch) yields a 20% reduction of range cells within 3dB, but the total number of sample support vectors within 3dB remains high enough for partially adaptive processing requirement.

The stationary GIP with the addition of four (4) elevation channels is shown in Figure 4.35. Note the reduction in the number of sample support vectors within 3dB when elevation channels are added. There are now 258 range cells within 3dB of the RUT. The addition of elevation channel means added definition to the antenna pattern. Therefore, the differences in illumination between any two range cells increases. The addition of platform maneuver is shown in Figure 4.36. Overall, the maneuver
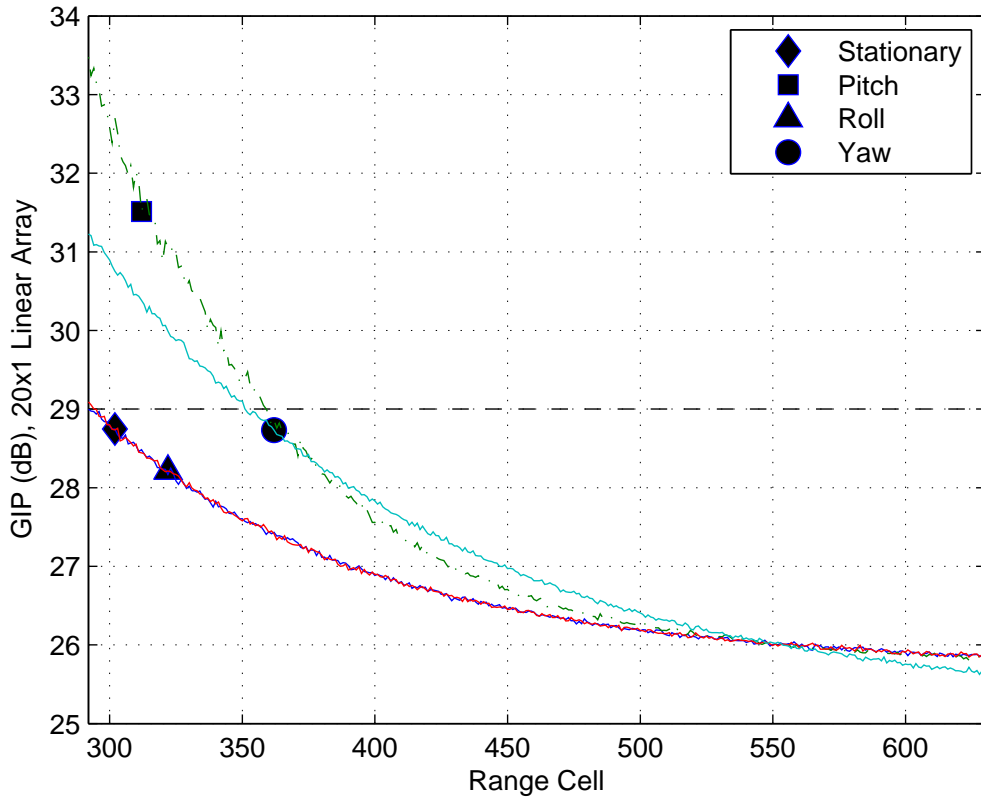
Figure 4.34: GIP for 20×1, known covariance at 66 km and with. The CPI length is 20 pulses. In the stationary and roll cases, 338 rangge cells are within 3dB of the RUT GIP. However, pitch has reduced that number to 271 and yaw to 278.

had little impact on the number of sample support vectors within 3dB of the RUT. Pitch yielded 253 (98% of stationary total), roll yielded 264 (102%), and yaw yielded 247 (96%). Overall for a target at 66 km, platform maneuver has little impact on data homogeneity around the RUT. The changes in angles at distant ranges is small, as are the resulting changes in illumination and phase of the returns.

Attention is now turned to a target at 11 km. Unlike the 66 km scenario, platform maneuver introduces significant changes in angle and illumination from one location to another, as shown in Section 4.2-4.4. The stationary GIP is shown in Figure 4.37. Note the value at the RUT (92) is 26 dB, corresponding to the dB value of MNP. A total of 592 range cells are within 3dB of the RUT. The maneuver results are shown in Figure 4.38. Pitch yielded 450 (76% of stationary total), roll yielded 596
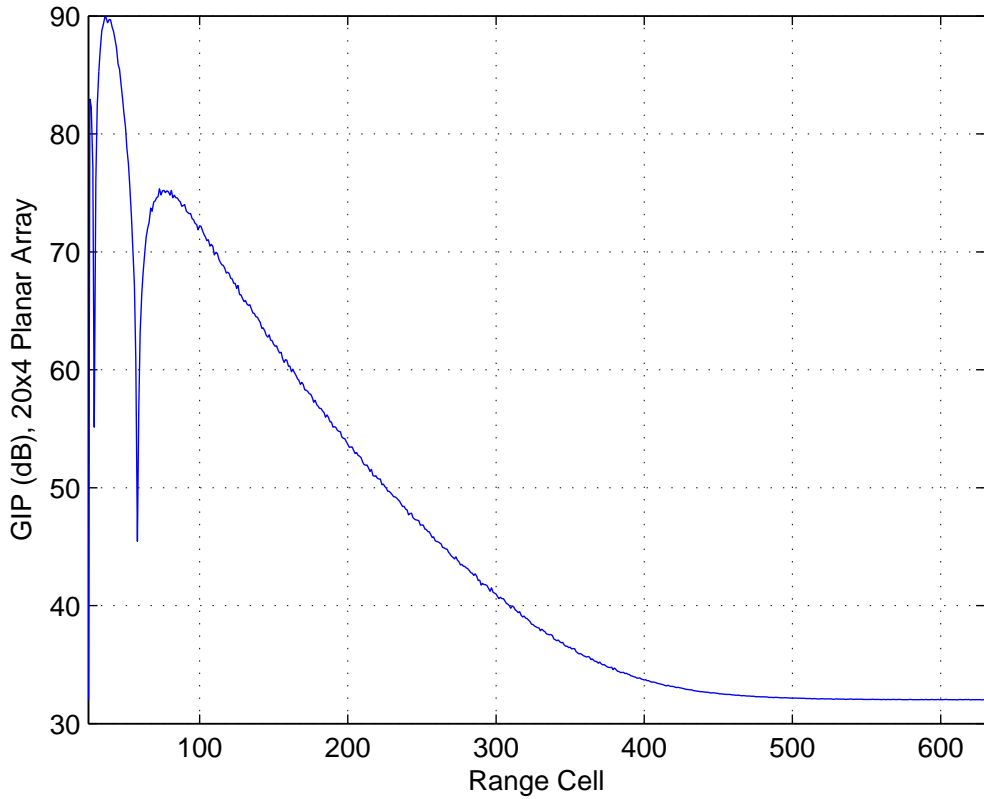
Figure 4.35: GIP for 20×4, known covariance at 66 km and no maneuver. The CPI length is 20 pulses. Note the value at the RUT (550) is 32 dB, corresponding to the dB value of MNP. A total of 258 range cells are within 3dB of the RUT.

(96%), and yaw yielded 393 (66%) range cells within 3dB of the RUT. However, range cells around the RUT are highly corrupted. Covariance estimation is often performed with sample support vectors near ranges of the RUT. However, maneuver makes these surrounding range cells highly heterogenous.

Overall for the linear array, sample support homogeneity effects are increased at closer range. At 66 km, sample support within 3dB of the RUT is 80% of the stationary total when pitch is introduced, 100% for roll, and 82% for yaw. At 11 km, those numbers fall to 76%, 96%, and 66% respectively. Additionally, the cells surrounding the RUT are highly heterogenous at 11 km. Sample support homogeneity increases when elevation channels are added, for both 11 km and 66 km. The increased elevation channels decreases the overall illumination of the clutter. When maneuver

110
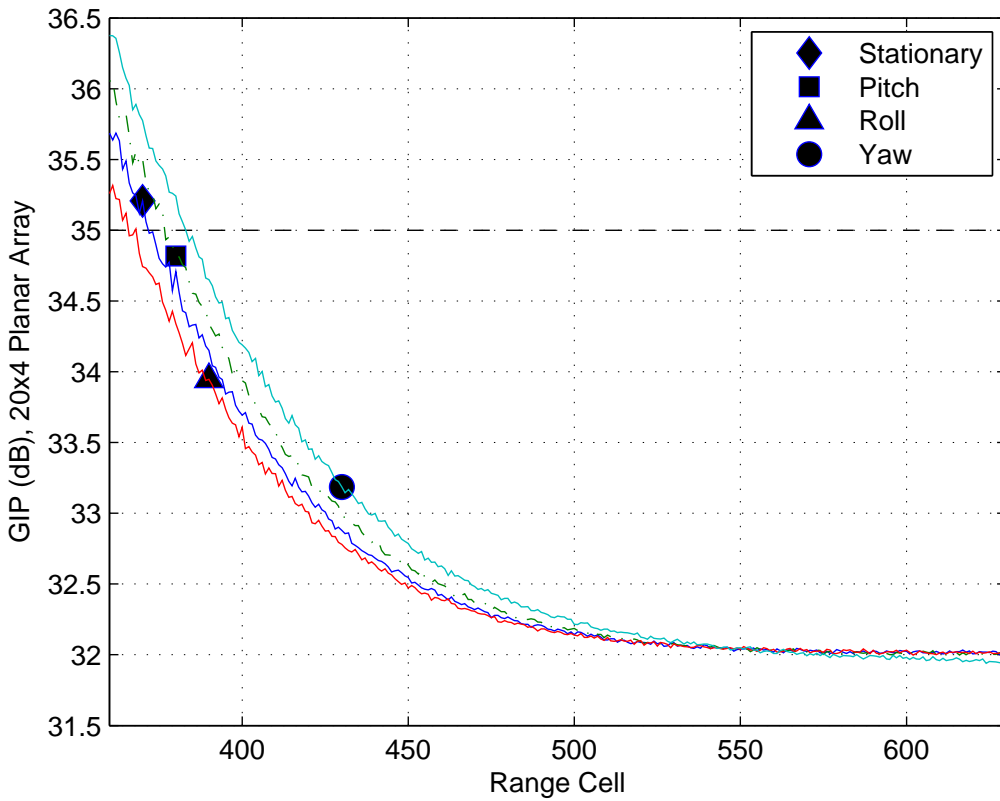
Figure 4.36:   GIP for 20×4, known covariance at 66 km with maneuver. The CPI length is 20 pulses with the RUT =550. Pitch yielded 253 (98% of stationary total), roll yielded 264 (102%), and yaw yielded 247 (96%) range cells within 3dB of the RUT.

is introduced, the changes is illumination are lessened and the resulting data more "alike".

4.6   Results Summary

Pitch maneuver effects are limited unless the number of azimuth channels produce a beamwidth on the order of the change in azimuth and elevation to the range of interest. MF performance improves as the number of azimuth channels increases, until that threshold pattern resolution is achieved. The number of azimuth channels needed is proportional to the range of interest, thus pitch effects are strongest at close ranges. The addition of elevation channel mitigate pitch effects, but the added
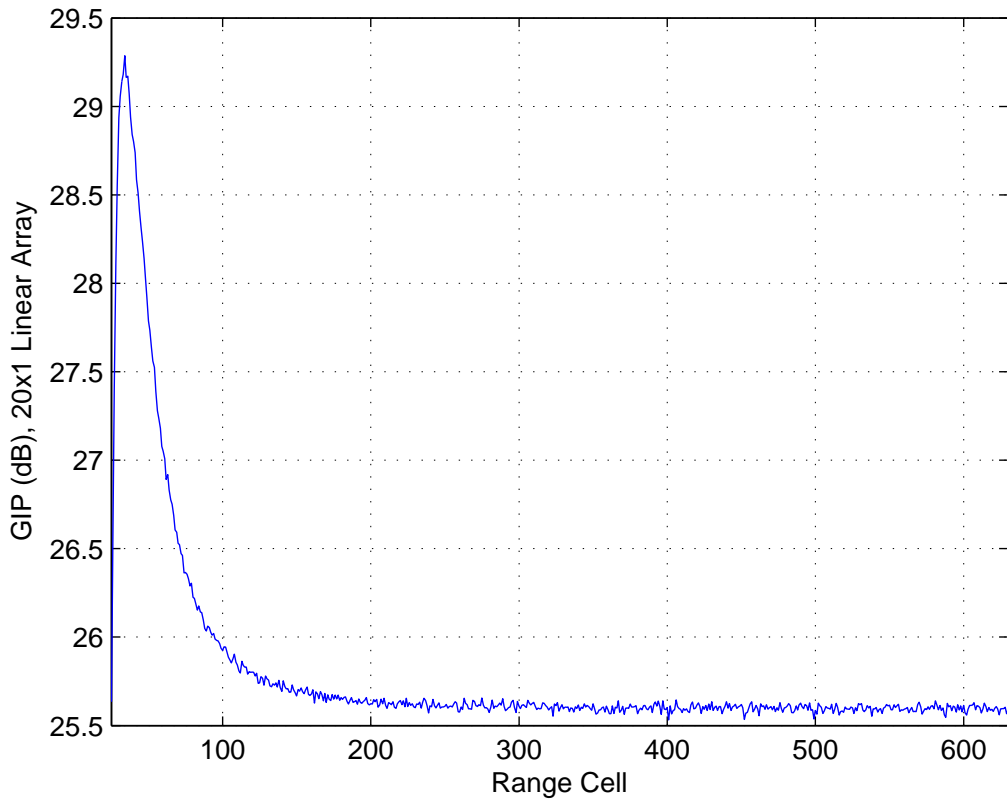
Figure 4.37: GIP for 20×1, known covariance at 11 km and no maneuver. The CPI length is 20 pulses. Note the value at the RUT (92) is 26 dB, corresponding to the dB value of MNP. A total of 592 range cells are within 3dB of the RUT.

DOF are unnecessary at ranges where pitch is a non-factor. The target resides in the mainbeam at boresight throughout the CPI, due to the rotation about the boresight axis.

Roll has little impact on the linear array at all ranges, due the the lack of elevation definition in the antenna pattern. That lack of definition translates to minimal changes in clutter and target illumination. Increases in the number of azimuth channels narrows the clutter null and improves MF performance. The addition of elevation channels, however, magnifies roll impact. The added elevation definition changes clutter and target illumination, resulting in degraded performance.
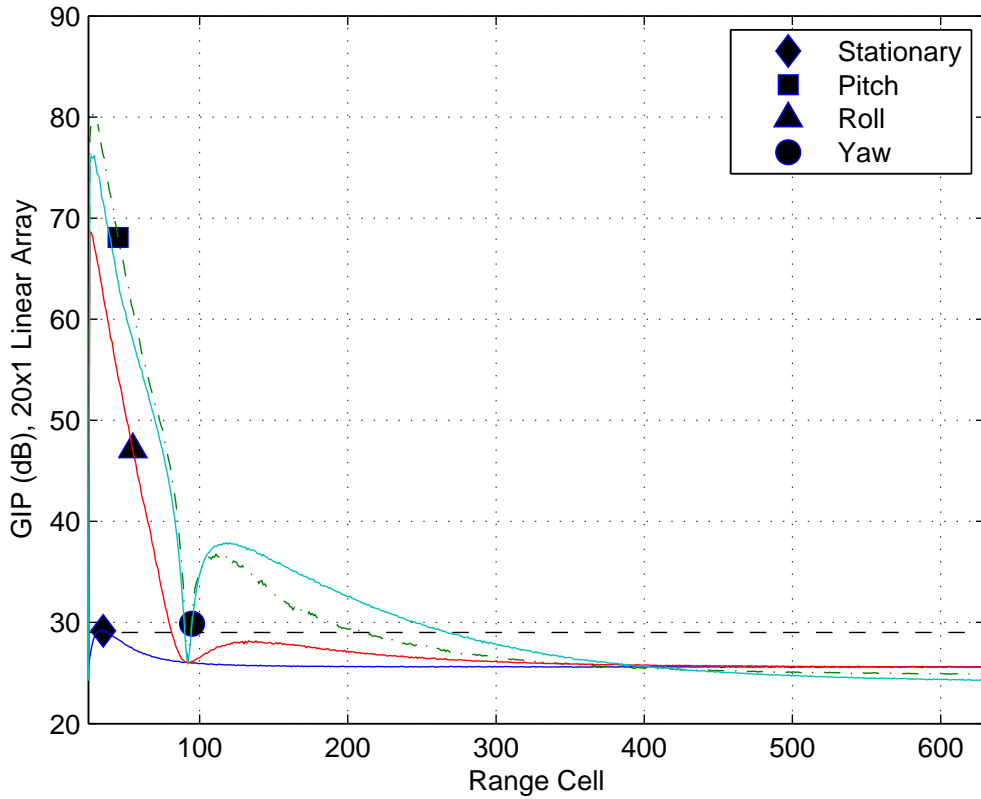
Figure 4.38:   GIP for 20×1, known covariance at 11 km with maneuver. The CPI length is 20 pulses with the RUT =92. Pitch yielded 450 (76% of stationary total), roll yielded 596 (96%), and yaw yielded 393 (66%) range cells within 3dB of the RUT. Range cells around the RUT are very heterogenous.

The most devastating maneuver effect at all ranges is yaw. The main culprit is drastically lower power with which the target is illuminated. Increasing the number of azimuth channels tightens the antenna beamwidth, leading to decreased target illumination and MF performance. The addition of elevation channels slightly improves performance at close ranges, where the decrease in clutter illumination is noticeable. As range increases, the added elevation channels have less impact as the clutter illumination decreases with range.

Similar to the MF SINR results, platform maneuver impacts on sample support homogeneity are more pronounced at 11km than 66km. The changes in azimuth and elevation, and therefore the changes in the magnitude and phase of the clutter

Table 4.2: Percent reduction in number of sample support vectors GIP falling within 3dB of the RUT.

	Pitch		Roll		Yaw	
	11 km	66 km	11 km	66 km	11 km	66 km
Linear	24%	20%	4%	0%	34%	18%
Planar	4%	2%	3%	0%	6%	4%

snapshots, are increased. The largest impact is observed in the linear array with yaw at 11km, where only 66% of sample support vectors originally within 3dB of the RUT remain within 3dB. This, and all GIP results, are *highly* optimistic given the array sizes tested. Recall pitch effects are not seen in the output SINR plots for 66km until N approached 115 elements. Yet 20% of sample support previously with 3dB of the RUT was lost when the array was just 20×1.

V. Conclusions

This research develops a space-time-adaptive-processing (STAP) model incorporating platform pitch, yaw, and roll. It characterizes the resulting interference environment, and examines the maneuver impact on fully adaptive processing performance and homogeneous sample support. Chapter II summarizes the airborne radar problem, the stationary STAP model of $[3, 10]$, and STAP fundamentals. The model of $[3, 10]$ serves as the foundation for the maneuver model. Chapter III details the maneuver model, including modified signal, target, clutter, and formatting models. Chapter IV simulates Chapter III's model. Each maneuver and its effect on the interference environment, target, Signal-to-Interference-plus-Noise-Ration (Ratio), and homogeneous sample support are examined in detail.

5.1 STAP Maneuver Model for Side-Looking Arrays

The maneuver model developed can simulate any degree of pitch, roll, yaw, or any combination of the three. This research focused on development of the model itself, versus specific innovative and complex scenarios to simulate. The framework developed, however, is capable of handling complex rotations not addressed in this research's simulations. The overriding theme of the maneuver model is that singular quantities in the stationary model of $[3, 10]$ possess M unique quantities in the maneuver model. The platform defines the reference coordinate system at all times. The (θ, ϕ) radar coordinates of each clutter patch and the target are first transformed into their cartesian counterparts (x,y,z). Rotation matrices are used to recalculate the coordinates to each (x,y,z) point based on the amount of rotation, measured with the platform orientation as the reference. The resulting (x',y',z') coordinates are transformed back to radar coordinates (θ', ϕ'). Each location has M (θ', ϕ') pairs, translating to M Doppler frequencies, spatial frequencies, and amplitudes. Four $MNP \times 1$ vectors are created, one for amplitude, one each for phase contributions due horizontal spacing, vertical spacing, and Doppler. The Kronecker product paradigm is replaced with the Hadamard product in creating the space-time snapshots.

5.2 Impact on Matched Filter Performance

Pitch maneuver effects are limited unless the number of azimuth channels produce a beamwidth on the order of the change in azimuth and elevation to the range of interest. MF performance improves as the number of azimuth channels increases, until that threshold pattern resolution is achieved. The number of azimuth channels needed is proportional to the range of interest, thus pitch effects are strongest at close ranges. The addition of elevation channels mitigates pitch effects, but the added DOF are unnecessary at ranges where pitch is a non-factor. The target resides in the mainbeam at boresight throughout the CPI, due to the rotation about the boresight axis.

Roll has little impact on the linear array at all ranges, due the the lack of elevation definition in the antenna pattern. That lack of definition translates to minimal changes in clutter and target illumination. Increases in the number of azimuth channels narrows the clutter null and improves MF performance. The addition of elevation channels, however, magnifies roll impact. The added elevation definition changes clutter and target illumination, resulting in degraded performance.

The most devastating maneuver effect at all ranges is yaw. The main culprit is drastically lower power with which the target is illuminated. Increasing the number of azimuth channels tightens the antenna beamwidth, leading to decreased target illumination and MF performance. The addition of elevation channels slightly improves performance at close ranges, where the decrease in clutter illumination is noticeable. As range increases, the added elevation channels have less impact as the clutter illumination decreases with range.

5.3 Impact on Sample Support Homogeneity

Similar to the MF SINR results, platform maneuver impacts are more pronounced at 11km than 66km. The changes in azimuth and elevation, and therefore the changes in the magnitude and phase of the clutter snapshots, are increased. The

largest impact is observed in the linear array with yaw at 11km, where 34% of sample support vectors originally within 3dB of the RUT are lost. This, and all GIP results, are *highly* optimistic given the array sizes tested. Recall pitch effects are not seen in the output SINR plots for 66km until N approached 115 elements. Yet 20% of sample support previously with 3dB of the RUT was lost when the array was just 20×1.

5.4 *Improvements and Future Research*

The model developed offers many potential extensions for future research. The first improvement is the addition of motion compensated steering. Motion compensated steering contains two parts: compensation on transmit and compensation on receive. On transmit, simulations for this research restricted antenna steering to its boresight, effectively making the radar unaware of its own maneuver. Radar platforms today have the ability to monitor their position and steer their transmit beam to a fixed location. Adding this feature to the model requires a simple modification. The antenna pattern presented as steered to $(\theta, \phi) = (0, 0)$ in Equation (2.30) as,

$$W(\theta, \phi) = \sum_{p=0}^{P-1} \sum_{n=0}^{N-1} e^{j2\pi n \vartheta_x} e^{j2\pi p \vartheta_z}. \tag{5.1}$$

Steering the beam on transmit changes this expression to

$$W(\theta, \phi) = \sum_{p=0}^{P-1} \sum_{n=0}^{N-1} e^{j2\pi n \vartheta_x} e^{j2\pi p \vartheta_z} e^{j2\pi n \vartheta_x^l} e^{j2\pi p \vartheta_z^l}, \tag{5.2}$$

where ϑ_x^l and ϑ_z^l are the spatial frequencies corresponding to look location (θ^l, ϕ^l). The target location is therefore calculated based on the original stationary geometry, and the M values to that target are calculated and create $M \times 1$ vectors of antenna steer. Ideally, the radar is able to update its look direction every range cell. The second part of motion compensated steering, compensation on receive, is already completely within the context of the model. Motion compensation on receive refers to adapting with the motion compensated steering vector. This model calculates

that steering vector, but adapted with the original uncompensated steering vector. Mathematically, the MF weight vector calculation changes from,

$$\mathbf{w} = \tilde{\mathbf{R}}^{-1}\mathbf{v}, \tag{5.3}$$

to

$$\tilde{\mathbf{w}} = \tilde{\mathbf{R}}^{-1}\tilde{\mathbf{v}}, \tag{5.4}$$

for motion compensated steering on receive.

The second improvement and future extension of this research is conversion from SL to forward-looking (FL). The conversion itself is rather simple. Converting this model to FL requires a new definition of the aircraft velocity vector. It was previously derived as,

$$\vec{\mathbf{v}}_a = v_a\hat{\mathbf{x}}. \tag{5.5}$$

The FL velocity vector is

$$\vec{\mathbf{v}}_a = v_a\hat{\mathbf{y}}. \tag{5.6}$$

And the normalized Doppler frequency of a clutter patch at changes from

$$\bar{\omega} = 2\frac{v_a\cos\theta\sin\phi}{\lambda f_r}, \tag{5.7}$$

to

$$\bar{\omega} = 2\frac{v_a\cos\theta\cos\phi}{\lambda f_r}. \tag{5.8}$$

Additional modification is necessary in the target model, as the projection of the aircraft velocity vector to the target location changes as well. Nonetheless, the improvement itself is simple while the potential applications are not.

The final suggestion for improvement and research continuation is the use of sub-arrays. Real world antenna arrays often number in the hundreds or thousands of elements. Simulations for this research were limited in array size due to computational limits. The use of sub-arrays removes that limitation by simulating the increased array size on transmit, while keeping the temporal DOF at a manageable level. The added capability of sub-arrays enhances the potential applications of this research immensely.

Bibliography

1. Balanis, Constantine. *Antenna Theory.* John Wiley & Sons, Inc., New York, NY, second edition, 1997.

2. Brennan, L.E. and I.S. Reed. "Theory of Adaptive Radar". *IEEE Transactions on Aerospace and Electronic Systems*, AES-9(2):237–252, March 1973.

3. Hale, Todd B. *Airborne Radar Interference Suppression Using Adaptive Three-Dimensional Techniques.* Ph.D. dissertation, School of Engineering and Management, Air Force Institute of Technology (AETC), 2950 P Street, Bldg 640, Wright-Patterson AFB, OH 45433-7765, June 2002. AFIT/DS/ENG/02-02.

4. Herbert, George M. "Effects of platform rotation on STAP performance". *IEE Proceedings - Radar, Sonar, and Navigation*, 151(1):2–8, February 2005.

5. Klemm, Richard. *Principles of Space-Time Adaptive Processing*, volume 12 of *IEE Radar, Sonar, Navigation and Avionics Series.* Institution of Electrical Engineers (IEE), Michael Faraday House, Six Hills Way, Stevenage, Herts. SG1 2AY, United Kingdom, 2002. ISBN 0852961723.

6. Mahafza, Bassem R. *Introduction to Radar Analysis.* CRC Press LLC, 2000 N.W. Corporate Blvd., Boca Raton, FL 33431, 1998.

7. Richardson, P.G. "Effects of manoeuvre on space-time adaptive processing". *Proceedings of the 1997 IEE Radar Conference*, 285–290. Institution of Electrical Engineers (IEE), Edinburgh, Scotland, October 1997.

8. Richardson, P.G. "Space-time adaptive processing for manoeuvring airborne radar". *IEEE Electronics and Communication Engineering Journal*, 11(1):57–63, February 1999.

9. Skolnik, Merrill I. *Introduction to Radar Systems.* McGraw-Hill, Inc., 1221 Avenue of the Americas, New York, NY 10020, third edition, 2001. ISBN: 0072909803.

10. Ward, James. *Space-Time Adaptive Processing for Airborne Radar.* Contract F19628-95-C-0002, Lincoln Laboratory, Massachusetts Institute of Technology, Lexington, Massachusetts, December 1994.

11. Wicks, Michael C., William L. Melvin, and Pinyuen Chen. "An Efficient Architecture for Nonhomogeneity Detection in Space-Time Adaptive Processing Airborne Early Warning Radar". *Proceedings of the 1997 International Radar Conference.* October 1997. Edinburgh, UK.

REPORT DOCUMENTATION PAGE

Form Approved
OMB No. 0704–0188

1. REPORT DATE *(DD–MM–YYYY)*	2. REPORT TYPE	3. DATES COVERED *(From — To)*
23–03–2006	Master's Thesis	Sept 2004 — Mar 2006

4. TITLE AND SUBTITLE

Space-Time Adaptive Processing
For Side-Looking Arrays
With Platform Maneuver

5a. CONTRACT NUMBER

5b. GRANT NUMBER

5c. PROGRAM ELEMENT NUMBER

6. AUTHOR(S)

John T. Buckreis, Capt, USAF

5d. PROJECT NUMBER

5e. TASK NUMBER

5f. WORK UNIT NUMBER

7. PERFORMING ORGANIZATION NAME(S) AND ADDRESS(ES)

Air Force Institute of Technology
Graduate School of Engineering and Management (AFIT/EN)
2950 Hobson Way, Bldg. 640
WPAFB OH 45433-7765

8. PERFORMING ORGANIZATION REPORT NUMBER

AFIT/GE/ENG/06-09

9. SPONSORING / MONITORING AGENCY NAME(S) AND ADDRESS(ES)

AFRL/SNRW (AFMC)
Attn: Michael Murray
2241 Avionics Circle, Bldg. 620
Wright Patterson Air Force Base, OH 45433
Michael.Murray@wpafb.af.mil, DSN 785-5579

10. SPONSOR/MONITOR'S ACRONYM(S)

11. SPONSOR/MONITOR'S REPORT NUMBER(S)

12. DISTRIBUTION / AVAILABILITY STATEMENT

Approval for public release; distribution is unlimited.

13. SUPPLEMENTARY NOTES

14. ABSTRACT

This research effort develops a space-time adaptive processing (STAP) radar data model for the side-looking (SL) array with platform maneuver. A primary assumption of most STAP models is the absence of platform maneuver during the coherent processing interval (CPI). This research abandons the platform stationarity assumption, allowing platform pitch, roll, and yaw during the CPI. The model developed characterizes platform maneuver effects on the clutter spectrum, examines Matched Filter (MF) output Signal-to-Interference-plus-Noise-Ratio (SINR), and investigates maneuver impact on sample support homogeneity. The introduction of pitch marginally impacts MF SINR due to the lack of achieved azimuth resolution in this research, but decreases available homogenous sample support 24% at 11 km and 20% at 66 km. Roll impact on MF performance is observed only in the planar array, with MF SINR dropping 4 dB but sample support homogeneity is unaffected. Yaw effects are the most devastating, dropping output SINR 15 dB at 11 km and 66 km, and decreasing available homogeneous sample support 34% at 11 km and 18% at 66 km.

15. SUBJECT TERMS

radar, space-time adaptive processing, STAP, platform maneuver, sample support, homogenous

16. SECURITY CLASSIFICATION OF:			17. LIMITATION OF ABSTRACT	18. NUMBER OF PAGES	19a. NAME OF RESPONSIBLE PERSON
a. REPORT	b. ABSTRACT	c. THIS PAGE			Todd B. Hale (ENG), PhD
U	U	U	UU	136	**19b. TELEPHONE NUMBER** *(include area code)* (937) 255–3636, ext 4639, Todd.Hale@afit.edu

Standard Form 298 (Rev. 8–98)
Prescribed by ANSI Std. Z39.18